KONINKLIJK BELGISCH INSTITUUT VOOR NATUURWETENSCHAPPEN
OD NATUUR – BEHEERSEENHEID VAN HET MATEMATISCH MODEL

MOnitoring en MOdellering van het cohesieve sedimenttransport en evaluatie van de effecten op het mariene ecosysteem ten gevolge van bagger- en stortoperatie (MOMO)

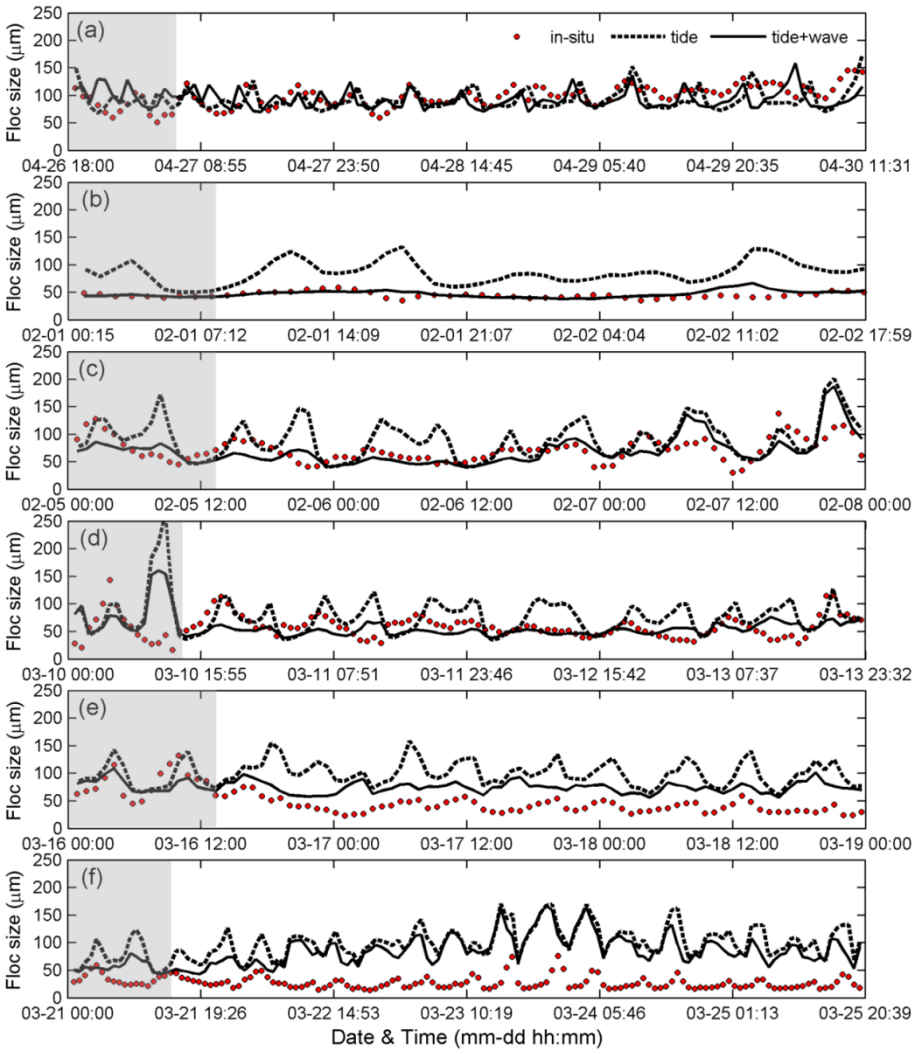

Activiteitsrapport (1 januari 2017 – 30 juni 2017)

Michael Fettweis, Matthias Baeye, Frederic Francken, Dries Van den Eynde, Peihung Chen[1], Jason Yu[1]

MOMO/8/MF/201708/NL/AR/1

museum
Operational Directorate Natural Environment
OD Nature I OD Natuur I DO Nature

KBIN-OD Natuur - BMM
Gulledelle 100
B–1200 Brussel
België

Inhoudsopgave

[1] National Sun Yat-Sen University, Department of Marine Environment and Engineering, Lien-Hai Road 70, 80424 Kaohsiung, Taiwan

1. Inleiding

1.1. Voorwerp van deze opdracht

Het MOMO-project (monitoring en modellering van het cohesieve sedimenttransport en de evaluatie van de effecten op het mariene ecosysteem ten gevolge van bagger- en stortopera-tie) maakt deel uit van de algemene en permanente verplichtingen van monitoring en evalua-tie van de effecten van alle menselijke activiteiten op het mariene ecosysteem waaraan België gebonden is in overeenstemming met het verdrag betreffende de bescherming van het mariene milieu van de noordoostelijke Atlantische Oceaan (1992, OSPAR-Verdrag). De OSPAR Commissie heeft de objectieven van haar Joint Assessment and Monitoring Programme (JAMP) gedefinieerd tot 2021 met de publicatie van een holistisch "quality status report" van de Noordzee en waarvoor de federale overheid en de gewesten technische en wetenschappelijke bijdragen moeten afleveren ten laste van hun eigen middelen.

De menselijke activiteit die hier in het bijzonder wordt beoogd, is het storten in zee van baggerspecie waarvoor OSPAR een uitzondering heeft gemaakt op de algemene regel "alle stortingen in zee zijn verboden" (zie OSPAR-Verdrag, Bijlage II over de voorkoming en uitschakeling van verontreiniging door storting of verbranding). Het algemene doel van de opdracht is het bestuderen van de cohesieve sedimenten op het Belgisch Continentaal Plat (BCP) en dit met behulp van zowel numerieke modellen als het uitvoeren van metingen. De combinatie van monitoring en modellering zal gegevens kunnen aanleveren over de transportprocessen van deze fijne fractie en is daarom fundamenteel bij het beantwoorden van vragen over de samenstelling, de oorsprong en het verblijf ervan op het BCP, de veranderingen in de karakteristieken van dit sediment ten gevolge van de bagger- en stortoperaties, de effecten van de natuurlijke variabiliteit, de impact op het mariene ecosysteem in het bijzonder door de wijziging van habitats, de schatting van de netto input van gevaarlijke stoffen op het mariene milieu en de mogelijkheden om deze laatste twee te beperken.

Een samenvatting van de resultaten uit de voorbije vergunningsperiode kan gevonden worden in het Syntheserapportten over de effecten op het mariene milieu van baggerspeciestortingen (Lauwaert et al. 2016) dat gepubliceerd werd conform art. 10 van het K.B. van 12 maart 2000 ter definiëring van de procedure voor machtiging van het storten in de Noordzee van bepaalde stoffen en materialen.

1.2. Algemene doelstellingen

Het onderzoek heeft als doel om de effecten van baggerspeciestortingen op het mariene ecosysteem (fysische aspecten) te onderzoeken en kadert in de algemene doelstellingen om de baggerwerken op het BCP en in de kusthavens te verminderen en om een gedetailleerd inzicht te verwerven van de fysische processen die plaatsvinden in het mariene kader waarbinnen deze baggerwerken worden uitgevoerd. Dit impliceert enerzijds beleidsondersteunend onderzoek naar de vermindering van de sedimentatie op de baggerplaatsen en het evalueren van alternatieve stortmethoden. Anderzijds is vernieuwend onderzoek voor het beter schatten van de effecten van het storten van baggerspecie. Dit is specifiek gericht op het dynamische gedrag van silb in de waterkolom en op de bodem en zal uitgevoerd worden met behulp van modellen, in situ metingen en remote sensing data.

<u>1) In situ en remote sensing metingen en data analyse</u>

De monitoring van effecten van baggerspeciestortingen gebeurd met behulp van een vast

meetstation in de nabijheid van MOW1, en met meetcampagnes met de RV Belgica (een 4 tal meetcampagnes voor het verzamelen van traject informatie, profielen en de calibratie van sensoren; en een 10 tal campagnes voor het onderhoud van het meetstation te MOW1). De geplande monitoring is gericht op het begrijpen van processen, zodoende dat de waargenomen variabiliteit en de effecten van baggerspeciestortingen in een correct kader geplaatst kunnen worden. Een belangrijk deel is daarom gericht op zowel het uitvoeren van de in situ metingen, het garanderen van kwalitatief hoogwaardige data en het archiveren, rapporteren en interpreteren ervan. Remote sensing data afkomstig van onder andere satellieten worden gebruikt om een ruimtelijk beeld te bekomen.

2) Uitbouw en optimalisatie van het modelinstrumentarium

Het tijdens de voorbije jaren verbeterde en aangepaste slibtransportmodel zal verder worden ontwikkeld. Dit zal parallel gebeuren met de nieuwe inzichten die voorvloeien uit de metingen en de process gerichte interpretatie van de metingen.

3) Ondersteunend wetenschappelijke onderzoek

Monitoring gebaseerd op wetenschappelijke kennis is essentieel om de effecten van menselijke activiteiten (hier het storten van baggerspecie) te kunnen schatten en beheren. Om te kunnen voldoen aan de door OSPAR opgelegde verplichtingen van monitoring en evaluatie van de effecten van menselijke activiteiten is het ontwikkelen van nieuwe monitorings- en modelleractiviteiten nodig. Dit houdt in dat onderzoek dat de actuele stand van de wetenschappelijke kennis weerspiegelt wordt uitgevoerd en dat de hieruit voortvloeiende nieuwe ontwikkelingen geïntegreerd zullen worden in zowel de verbetering van het modelinstrumentarium als voor het beter begrijpen van het fysisch milieu.

1.3. Onderzoek Januari 2017 – December 2018

In het bijzonder is bij het opstellen van de hieronder vermelde taken rekening gehouden met de aanbevelingen voor de minister ter ondersteuning van de ontwikkeling van een versterkt milieubeleid zoals geformuleerd in het “Syntheserapport over de effecten op het mariene milieu van baggerspeciestortingen (2011)” dat uitgevoerd werd conform art. 10 van het K.B. van 12 maart 2000 ter definiëring van de procedure voor machtiging van het storten in de Noordzee van bepaalde stoffen en materialen. De specifieke acties in de periode 2017-2018 zullen uitgevoerd worden om de algemene doelstellingen in te vullen zijn de volgende:

Streven naar een efficiënter stortbeleid door:

- Optimalisatie van de stortlocaties. Bijkomende simulaties worden uitgevoerd voor het opzetten van een MER voor een alternatieve stortplaats (zie taak 2.2). Verder zullen de effecten van een efficiënter verplaatsen van het gebaggerde materiaal te Nieuwpoort en Blankenberge naar de stortzones (lozen i.p.v. storten) geëvalueerd worden (zie Taak 3.4);
- Onderzoek naar de mogelijkheden voor het opzetten van een operationeel stortmodel in overleg met aMT (Taak 2.3). Dit model zal geïntegreerd worden in de binnen BMM-OD Natuur beschikbare operationele modellen. Het model zal gebruikt worden om in functie van de voorspelde fysische (wind, stroming, golven, sedimenttransport, recirculatie), economische (afstand, grootte baggerschip) en ecologische aspecten op korte termijn een keuze te kunnen maken tussen de beschikbare stortlocaties. Hiervoor zal binnen de huidige periode het slibtransportmodel gevalideerd worden op de geografische variabiliteit van de turbiditeitszones en de flocculatie van het slib.

Continue monitoring van het fysisch-sedimentologische milieu waarbinnen de baggerwerken worden uitgevoerd (Taak 1) en aanpassing van de monitoring aan de nog op te

stellen targets voor het bereiken van de goede milieutoestand (GES), zoals gedefinieerd binnen MSFD;

Uitbouw en optimalisatie van het numerieke modelinstrumentarium, ter ondersteuning en verfijning van het onderzoek (Taak 2.1).

Taak 1: In situ en remote sensing metingen en data analyse

Taak 1.1 Langdurige metingen

Sinds eind 2009 worden er continue metingen uitgevoerd te MOW1 met behulp van een meetframe (tripode). Met dit frame worden stromingen, slibconcentratie, korrelgrootteverdeling van het suspensiemateriaal, saliniteit, temperatuur, waterdiepte en zeebodem altimetrie gemeten. Om een continue tijdreeks te hebben, wordt gebruik gemaakt van 2 tripodes. Na ongeveer 1 maand wordt de verankerde tripode voor onderhoud aan wal gebracht en wordt de tweede op de meetlocatie verankerd. Op de meetdata wordt een kwaliteitsanalyse uitgevoerd, zodat de goede data onderscheiden kunnen worden van slechte of niet betrouwbare data.

In 2013-2016 werden enkele langdurige metingen uitgevoerd met behulp van een OBS-5 sensor vastgemaakt aan de AW boei; deze metingen zullen verdergezet worden. De data geven informatie over de SPM concentratie aan het oppervlak en zijn aldus complementair aan de bodemnabije metingen met de tripode. De data zijn ook van belang voor het calibreren en valideren van de oppervlakte SPM concentraties uit satellietbeelden.

Taak 1.2 Calibratie van sensoren tijdens in situ metingen

Tijdens 4 meetcampagnes per jaar met de R/V Belgica zullen een voldoende aantal 13-uursmetingen uitgevoerd worden met als hoofdoel het calibreren van optische of akoestische sensoren en het verzamelen van verticale profielen. De metingen zullen plaatsvinden in het kustgebied van het BCP. De optische metingen (transmissometer, Optical Backscatter Sensor) zullen gecalibreerd worden met de opgemeten hoeveelheid materie in suspensie (gravimetrische bepalingen na filtratie) om te komen tot massa concentraties. Naast de totale hoeveelheid aan suspensiemateriaal (SPM) wordt ook de concentratie aan POC/PON, TEP, chlorophyl (Chl-a, Chl-b) en phaeofytine (a, b) bepaald. Stalen van suspensiemateriaal zullen genomen worden met de centrifuge om de samenstelling ervan te bepalen.

Taak 1.3 Kwaliteitscontrole van de data

In situ metingen zijn steeeds onderhevig aan onzekerheden tengevolge van random meetfouten (gebrek aan precisie), systematische fouten (onnauwkeurigheid), menselijke fouten, en de statistische variabiliteit van de parameter. De fouten hebben hun oorsprong in de onnauwkeurigheid en het gebrek aan precisie van het meetinstrument of de procedures (bv. waterstaalname en filtratie). Doel is om de fout op de verschillende onderdelen van de metingen (filtratie, calibratie, langdurige trends...) te schatten. Een procedure die de best practice beschrijft zal worden opgesteld.

Een belangrijk aandachtspunt bij deze langdurige datareeksen is het garanderen van een gelijke kwaliteit in de tijd van de verzamelde data. De vraag die zich bij onze SPM concentratiemetingen stelt is niet zozeer het opmeten van hogere of lagere waarden, mogelijks veroozaakt door het toepassen van een andere stortstrategie, maar het garanderen dat deze waarden inderdaad veroorzaakt worden door menselijke activiteiten (bv storten) en niet het effect zijn van natuurlijke fluctuaties. Om kwaliteitsvolle data te kunnen leveren over een lange periode, die gebruikt kunnen worden om langdurige trends te identificeren, is het nodig om een rigoureuze kwaliteitscontrole uit te voeren. OBS alsook akoestische sensoren zijn gevoelig aan de samenstelling en korrelgrootte van het gesuspendeerde

materiaal. Dit kan varieren in functie van de boven vermelde frequenties, maar hieromtrent is er nog geen afdoende duidelijkheid wat de metingen te MOW1 betreft. De wetenschappelijke vragen die daarom moeten worden, hebben betrekking tot in situ en in lab calibratie van de OBS sensoren en van akoestische backscatter sensoren en de meetfouten.

Taak 1.4: Verwerking en interpretatie van de data

De metingen vergaard tijdens de 13-uursmetingen aan boord van de Belgica en met de tripode worden verwerkt en geïnterpreteerd. Hiervoor werden in het verleden al heel wat procedures (software) toegepast of ontwikkeld, zoals de berekening van de bodemschuifspanning uit turbulentiemetingen, entropieanalyse op partikelgrootteverdelingen, de opsplitising van multimodale partikelgrootteverdeling in een som van lognormale verdelingen, het groeperen van de data volgens getij, meteorologie, klimatologie en seizoenen. Deze methodes zijn opgenomen in de standaardverwerking van de data. De aldus verwerkte data dienen als basis voor het verder gebruik binnenin wetenschappelijke vragen.

Taak 1.5: Sedimentologie van zeebodem

De sedimentologie van stortplaatsen en referntiezones zal, in samenwerking met het ILVO, worden bestudeerd met alternatieve meettechnieken, zoals de Sediment Profile Imaging (SPI).

Taak 1.6: TBT analysen

TBT analysen op stalen aangeleverd door het ILVO zullen door het chemisch labo van het KBIN (Ecochem) worden uitgevoerd. Het betreft de analyse van 6 stalen (2 replica's).

Taak 2: Uitbouw en optimalisatie van het modelinstrumentarium

Taak 2.1: Verdere ontwikkelingen en validatie van een slibtransportmodel voor het BCP gebaseerd op Coherens V2

Het tijdens de voorbije jaren verbeterde en aangepaste slibtransportmodel zal worden gevalideerd met behulp van de langdurige meetreeksen en de satellietbeelden. Hierbij zal dezelfde methode als in Baeye et al. (2011) en zoals in taak 1.4 worden gebruikt om de modelresultaten te groeperen en te klasseren volgens windrichting, weertype en getij. Het voordeel van deze werkwijze is dat niet zozeer gekeken wordt of de correlatie tussen meting en modelresultaat in één of meerder punt goed is, maar dat globaal nagegaan wordt of het model de SPM dynamica op het BCP goed kan reproduceren.

Verdere ontwikkelingen aan het model parallel met nieuwe inzichten die voorvloeien uit de metingen en de process gerichte interpretatie van de metingen zullen worden geïmplementeerd in het model.

Taak 2.2: Ondersteuning bij de MER studie van een alternatieve stortlocatie

Op dit moment worden op het BCP vijf stortplaatsen gebruikt voor het gebaggerd materiaal afkomstig uit de vaargeulen op zee en de zeehavens: Zeebrugge Oost, S1, S2, B&W Oostende en Nieuwpoort. Door OD Natuur- BMM werd in het kader van het MOMO project onderzoek gedaan naar de efficiëntie van de stortplaatsen. Daaruit blijkt dat de recirculatie naar de baggerplaatsen het grootste is vanuit de stortplaats Zeebrugge Oost. Met behulp van numerieke modellen werden een aantal alternatieve locaties voor de stortplaats Zeebrugge Oost bestudeerd. In 2012-2013 werd een terreinproef uitgevoerd om de resultaten van de numerieke modellering op het terrein te valideren. Uit de resultaten van de terreinproef bleek dat er aanwijzingen zijn die de resultaten van de numerieke modellering bevestigen.

OD Natuur-BMM zal in deze studie instaan voor het uitvoeren van de nodige numerieke modelleringen in de eerste helft van 2017. Hiervoor zal gebruik gemaakt worden van

het bijgewerkte 3D stromingsmodel dat beschikbaar is bij OD Natuur-BMM. Het model is opgebouwd in Coherens V2, inclusief sedimenttransportmodule en flocculatiemodel. Meer specifiek zal de OD Natuur-BMM betrokken zijn bij:

Fase 1 (long list van mogelijke locaties en exploitatiescenario's opgemaakt worden): berekening van de recirculatie voor maximaal 10 mogelijke locaties en/of stortscenario's. Voor iedere berekening zullen voor een aantal combinaties van hydro-meteo randvoorwaarden simulaties uitgevoerd worden. Deze randvoorwaarden zijn zo gekozen dat ze optimale aansluiting verzekeren met de al eerder uitgevoerde simulaties.

Fase 2 (opmaak Milieu Effect Rapport): Bij de opmaak van het MER zelf is geen specifieke modellering nodig voor de inschatting van de effecten. Indien uit overleg met de vergunningsverlenende instanties blijkt dat simulaties moeten uitgevoerd worden ter onderbouwing van de gemaakte keuzes (recirculatie bij een bepaalde locatie/stortstrategie) kan dit uitgevoerd worden.

Taak 2.3: Operationeel stortmodel (vanaf 2018)

Overleg met aMT over het opstellen van een operationeel stormodel om de noden en de mogelijkheden te definiëren. Het model zal later (vanaf 2018) kunnen opgesteld worden en kan dan geïntegreerd worden in de binnen BMM-OD Natuur beschikbare operationele modellen. Het model zal kunnen gebruikt worden om in functie van de voorspelde fysische (wind, stroming, golven, sedimenttransport, recirculatie), economische (afstand, grootte baggerschip) en ecologische aspecten op korte termijn een keuze te kunnen maken tussen de beschikbare stortlocaties.

Taak 3: Ondersteunend wetenschappelijk onderzoek

Monitoring gebaseerd op wetenschappelijke kennis is essentieel om de effecten van menselijke activiteiten (hier het storten van baggerspecie) te kunnen schatten en beheren. Om te kunnen voldoen aan de door OSPAR opgelegde verplichtingen van monitoring en evaluatie van de effecten van menselijke activiteiten is een verdere implementatie van huidige en het ontwikkelen van nieuwe monitoringsactiviteiten nodig. Meer spefiek gericht op de activiteit 'storten van baggerspecie' worden hier – wat het fysische milieu betreft - turbiditeit, samenstelling van de zeebodem, bathymetrie en hydrografische condities beoogd. Deze taak speelt hierop in door de ontwikkeling van nieuwe tools die de actuele stand van de wetenschappelijke kennis weerspeiegelen teneinde de mthematische modellen te optimaliseren en verfijnen.

Taak 3.1: Sedimentuitwisseling tussen de zee en de haven van Zeebrugge

Slib stroomt de haven van Zeebrugge binnen rond HW, wanneer de stroming maximaal is. Gezien de grote turbulentie op dit moment op zee bestaat het SPM uit voornamelijk kleine vlokken met een lage valsnelheid. Eens het suspensiemateriaal de haven binnenkomt, neemt de turbulentie plots af, ontstaan er grotere vlokken en treed er een snelle bezinking op. Het verloop van de SPM concentratie in de haven zelf is goed gekend (zie onder andere de SPM concentratie metingen in de haven tijdens de terreinproef en de metingen van de topsliblaag), maar aan de havenmond zijn minder data beschikbaar om de sedimentuitwisseling in kaart te brengen en dit tijdens verschillende getij- en meteocondities. In deze taak zal de sedimentdynamica bestudeerd worden gebruikmakend van ADCP transects gemeten met de RV Belgica, van verticale profielen van SPM concentratie en vlokgrootte in en uit de haven, en van remote sensing beelden.

Taak 3.2: Microbiologische activiteit en de wisselwerking met sedimentdynamica

Een sleutelelement in het functioneren van kustnabije ecosystemen is de aanwezigheid van biotische en abiotische partikels. Vertikale en dus ook horizontale fluxen van SPM

worden bepaald door hun valsnelheid, die afhangt van de capaciteit van de deeltjes om te flocculeren. Flocculatie beïnvloedt de grootte van de gesuspendeerde deeltjes en bepaald daardoor de depositie van het slib. Op zijn beurt wordt flocculatie gestuurd door turbulentie, de SPM concentratie, en de oppervlakteigenschappen van de deeltjes, die van electrochemische of biologische oorsprong kunnen zijn. Wat dit laatste betreft heeft dit een wederzijdse invloed tot gevolg tussen het SPM en de primaire productie doordat stoffen zoals TEPs (transparent exopolymeric particles), die vrijkomen door het phytoplankton en de bacteriën, de vlokgrootte en dus ook de valsnelheid van het SPM beïnvloeden. Het belang van deze processen voor de slibdynamica in onze kustzone en dus ook voor de aanslibbing van havens en vaargeulen wordt gegeven door de uitzonderlijk hoge primaire productie in de Belgische kustzone tengevolge van eutrofiëring (algenbloei). Dat er een effect is werd al aangetoond door de metingen te MOW1 die lieten zien dat het SPM zich anders gedraagt in de winter dan in de biologisch actieve zomerperiode. In de winter is het SPM beter gemengd in de waterkolom dan in de zomer en treden er dus hogere concentraties op in de waterkolom. In de zomer bevindt zich meer suspensiemateriaal dicht tegen de bodem en daalt de SPM concentratie in de waterkolom. Dit roept volgende vragen op, in het bijzonder 1) Hoe moet het modelinstrumentarium (flocculatiemodule) worden aangepast om deze seizoenaliteit te kunnen modelleren? 2) Wordt de seizoenaliteit in SPM concentratie en biologische activiteit veroorzaakt doordat de algen TEP produceren, dat aanleiding geeft tot de vorming van grotere vlokken en dus een hogere bezinking van het SPM als gevolg heeft, of daalt eerst de SPM concentratie tengevolge van fysische processen (afname van de stormfrequentie in de lente) en start de algenbloei nadat het water minder troebel is geworden? 3) De troebelheid in de waterkolom is in de Belgische kustzone altijd hoog en de lichtindringing is ook in de zomer beperkt. Speelt troebelheid (en dus ook SPM concentratie) een belangrijke rol bij start van de algenbloei bepaald of is dit eerder een secundair process?

Het onderzoek zal gericht zijn op het verzamelen van in situ meetdata van TEP, SPM en Chl concentratie te MOW1 en op andere plaatsen; het analyseren van de data in functie van boven aangehaalde vragen; het incorporeren van de biologische activiteit in een flocculatiemodel en het uitvoeren van modelberekeningen.

<u>Taak 3.3: Overgang kustzone – offshore: Waarom is het turbiditeitsgebied beperkt tot de kustzone?</u>

Turbulentie samen met de SPM concentratie bepalen de lichthoeveelheid in het water. De cross-shore stroming in vele kustgebieden is gekenmerkt door landinwaarts gerichte stroming dicht tegen de bodem en een zeewaarts gerichte aan het wateroppervlak (estuariene circulatie). Het is op dit moment niet duidelijk hoe het Schelde estuarium deze circulatie beïnvloed. Hierdoor wordt het SPM (en het phytoplankton) naar de kust getransporteerd in de bodemlaag nadat het eerst naar offshore werd getransporteerd in de oppervlaktelaag. Deze mechanismus is mogelijks verantwoordelijk voor de scherpe gradiënt in SPM concentratie langsheen onder andere de Belgische kust en de Westerscheldmonding. Ook turbulentie is gekenmerkt door een gradïent: hoog dicht tegen de kust en afnemend naar offshore toe. Dit komt overeen met een toename in waterdiepte naar offshore toe. Bij geringere waterdieptes is de turbulentie hoger, de vertikale menging dus sneller en dus de tijd met lage SPM concentratie korter. Naar offshore toe zal de lichthoeveelheid in de waterkolom dus toenemen in de oppervlaktelaag omdat de diepte toeneemt. Vanaf een bepaalde diepte bereikt het SPM niet meer de oppervlakte tijdens vertikale menging. De afname in SPM concentratie is dus mogelijkes een afspiegeling van de gradiënten in diepte en turbulentie. Dit proces werd aangetoond in andere delen van de Noordzee (Duitse

Bocht), maar nog niet in de Belgische kustzone.

Het onderzoek zal gericht zijn op het verzamelen van in situ meetdata van TEP, SPM en Chl concentratie op een drietal locaties gelegen op verschillende afstanden van de kust; het varen van ADCP transects dwars op de kust; en het analyseren van de data. TEP en Chl zijn een onderdeel van het SPM en hebben een significante invloed op de seizoenaliteit van de SPM dynamica.

Taak 3.4: Alternatieve Stortstrategies Nieuwpoort

Er zal ondersteuning gegeven worden aan afdeling kust in verband met het opzetten van een wetenschappelijke terreinproef om de impact van het verpompen van baggerspecie uit de haven van Nieuwpoort op een stortzone te evalueren. Details hiervan zullen op een vergadering van de technische werkgroep besproken worden.

1.4. Gerapporteerde en/of uitgevoerde taken

Periode Januari 2017 – Juni 2017

Taak 1.1: De meetreeks te MOW1 werd verdergezet.

Taak 1.2: Calibratie van sensoren werd uitgevoerd tijdens campagne 2017/20 (21-23/06/2017).

Taak 2.1: De bodemschuifspanning gemodelleerd met het hydrodynamisch model werd gevalideerd met in situ data te MOW1. Dit is een eerste stap bij de validatie van een slibtransportmodel voor het BCP gebaseerd op Coherens V2, zie appendix 2.

Taak 2.2: Simulaties met de nieuwe versie van het COHERENS V2 model voor de Belgische kustzone werden uitgevoerd ter ondersteuning van de MER studie voor een alternatieve stortlocatie, zie hoofdstuk 2.

Taak 3.2: Waterstalen voor de bepaling van TEP concentratie werden 1-2 wekelijks genomen te Oostende.
Een bestaand flocculatiemodel werd aangepast om biologisch flocculatie te simuleren. De resultaten werden gecalibreerd en gevalideerd met metingen te MOW1 en Blankenberge, zie hoofdstuk 3.

1.5. Publicaties (januari 2017 – december 2018)

Hieronder wordt een overzicht gegeven van publicatie met directe betrokkenheid van het KBIN waar resultaten en data uit het MOMO project in werden gebruikt.

Activiteits-, Meet- en Syntheserapporten

Fettweis M, Baeye M, Francken F, Van den Eynde D, Chen P, Yu J. 2017. MOMO activiteitsrapport (1 januari – 30 juni 2017). BMM-rapport MOMO/8/MF/201707/NL/AR/1, 32pp + app.

Conferenties/Workshops

Adriaens R, Zeelmakers E, Fettweis M, Vanlierde E, Vanlede J, Stassen P, Elsen J, Środoń J, Vandenberghe N. 2017. Quantitative clay mineralogy as provenance indicator for the recent muds located at the marine limit of influence of the Scheldt estuary. Scheldt-Ems workshop, 16-17 February, Antwerp (Belgium).

Publicaties (tijdschriften, hoofdstuk in boeken)

Adriaens R, Zeelmaekers E, Fettweis M, Vanlierde E, Vanlede J, Stassen P, Elsen J, Środoń J, Vandenberghe N. Quantitative clay mineralogy as provenance indicator for recent muds in the southern North Sea (under review for *Marine Geology*)

Chen P, Yu JCS, Fettweis M. Modelling storm-influenced SPM flocculation using a tide–wave-combined biomineral model. *Water Environment Research* (revision submitted in June 2017).

2. Modellering van de SPM verspreiding na storten: Ondersteuning bij de MER voor een alternatieve stortlocatie

In kader van de MER voor een alternatieve stortlocatie werd een modelleerstudie uitgevoerd naar de recirculatie van gestort baggermateriaal uit de haven van Zeebrugge terug naar de haven en dit voor de bestaande stortplaats B&W Zeebrugge Oost en enkele alternatieve stortplaatsen. De simulaties werden in overleg met ARCADIS en de Technische Werkgroep Baggerstorten opgesteld, de resultaten van de numerieke simulaties werden door Arcadis verwerkt en gerapporteerd (Arcadis, 2017). De huidige studie is het vervolg van eerdere numerieke modellerstudies (Fettweis et al. 2005, 2009; Van den Eynde & Fettweis 2006, 2015) en een terreinproef uitgevoerd in 2013 en 2014 (Fettweis et al. 2015, 2016) die suggereerden dat de recirculatie van het gestort baggermateriaal terug naar de haven kan verminderd worden door een alternatieve stortplaats voor B&W Zeebrugge Oost te kiezen.

Op basis van verschillende parameters (vaarafstand, waterdiepte, andere gebruik) werden door Arcadis mogelijke posities naar voor geschoven, namelijk O4 (51°22’09.97”N, 3°12’37.15”O) gelegen ten oosten van de haven van Zeebrugge maar dichter bij de haven dan stortplaats Zeebrugge-Oost; O1 (51°22’55.93”N, 3°08’21.67”O) gelegen ten westen van Zeebrugge maar iets verder uit de kust; O3 (51°21’07.94”N, 3°05’28.31”O) ook ten westen van Zeebrugge gelegen maar dichter bij de kust; en A3 (51°21’59.68”N, 3°09’04.11”O) ook ten westen van Zeebrugge gelegen maar dichter tegen de haven (zie Figuur 2.1). Verder werden vier atmosferische condities geselecteerd namelijk geen wind, een constante wind uit het NNO met een windsnelheid van 7,5 m/s (zomercondities), een constante wind uit het ZW met een windsnelheid van 9,5 m/s (wintercondities) en een constante wind uit het NW met een windsnelheid van 8,5 m/s. Deze laatste windconditie werd gedefinieerd omdat bij deze windcondities kan verwacht worden dat de recirculatie het grootste zou zijn vanuit stortplaats O1.

Figuur 2.1: De alternatieve stortlocaties voor Zeebrugge Oost.

De golven voor deze windcondities werden berekend met het derde generatie golfmodel WAM met drie gekoppelde roosters. Voor de hydrodynamica, sedimentdynamica en morfologie werd gebruik gemaakt van het COHERENS V2 model. Hiervoor werd een modellentrein opgesteld met vier gekoppelde roosters. Het grofste rooster omvat het gehele Noordwest-Europese Continentale Plat, het fijnste rooster omvat het Belgisch Continentale Plat met een resolutie van ongeveer 270 m x 280 m. De simulaties werden uitgevoerd voor een periode van 1 maand, waarbij om de 2 uren verspreid over 5 minuten een hoeveelheid van 650 ton droge stof (TDS) werd gestort in een roosterpunt van het model. 90% van het materiaal werd hierbij geplaatst in de onderste laag van het model (suspensiemateriaal). De resterende 10% van het materiaal in de oppervlaktelaag van het model, overeenkomstig waarnemingen van stortoperaties. Als mediane korrelgrootte werd 50 µm gebruikt; de valsnelheid en de kritische bodemspanning voor erosie werden respectievelijk op 1 mm/s en 0.5 Pa gezet.

In Tabel 2.1 worden de uitgevoerde simulaties voorgesteld. Simulatie 01, 02, 03 en 10 zijn referentieruns (i.e. storten op B&W Zeebrugge Oost) voor de verschillende meteorologische condities. In de andere simulaties wordt de recirculatie bepaald bij de alternatieve stortplaatsen. De berekende erosie en sedimentatie op de stortlocaties werden als realistisch bevonden, met een geringe sedimentatie tijdens het storten en een erosie van dit materiaal later in functie van de heersende stroomsnelheid. Op langere termijn is er geen sedimentatie waarneembaar op de stortplaatsen, wat overeenkomst met de observaties. De berekende recirculatie van het gestorte materiaal voor het referentiescenario 01 is ongeveer 8 %, wat overeenkomt met de geschatte waarde van ongeveer 10 % (Arcadis 2017).

Tabel 2.1: Lijst van simulaties

Run	Stortlocatie	Wind
01	Zeebrugge-Oost	Geen
02	Zeebrugge-Oost	NNO
03	Zeebrugge-Oost	ZW
04	O4	NNO
05	O1	ZW
06	O4	ZW
07	O1	NNO
08	O3	ZW
09	A3	ZW
10	Zeebrugge-Oost	NW
11	O1	NW

3. Modellering van de interactie tussen microbiologische activiteit en sediment dynamica

Suspended particulate matter (SPM) is a mixture of organic and inorganic particles that has specific physicochemical properties (Berlamont et al. 1993; Maggi 2009). When the SPM consists of cohesive sediments then particles interact with the surrounding environment through physical, biological, and chemical mechanisms (Manning et al., 2006) and resulting in a change of the inherent properties (density, size) of the particles by flocculation. In marine and estuarine environments, flocculation influences sediment transport and may influence coastal eutrophication, algae blooms, fate of pollutants, ephemeral sealing of the sea-floor by fluffy layers, benthic and pelagic ecosystems and siltation of navigation channels and harbors (Lancelot et al. 1987; Lee and Wiberg 2002; Kirby 2011). Flocculation occur in a turbulent flow field, as induced by e.g. tides, and combines aggregation, where the suspended particles form larger-sized clusters or flocs, and breakage, where the larger flocs are broken up into their constituting particles. The conceptual relationship between floc diameter, SPM concentration and shear stress proposed by Dyer (1989) shows that turbulent flow enhances particle aggregation and increases the size and settling velocity of the flocs. SPM dynamics are further influenced by waves, particularly during storms. In nearshore areas waves may W induce high turbulent shear, which potentially enhance floc fragmentation or break up. In addition, wave-induced erosion may lead to the resuspension of coarser-grained sediment particles with unimodal particle-size distributions (PSDs) (Li and Mehta 2000; van Kessel and Kranenburg 1998), or to the formation of high concentrated mud suspensions (HCMSs) or mixed suspensions that combine coarser grains and flocs that have usually a multimodal PSD (Baeye et al. 2011; Fettweis et al. 2010). The effects of wave-driven resuspensions and floc break-up may thus yield complex floc dynamics.

Several flocculation models have been developed to simulate flocculation behavior in marine and estuarine environments; they can be categorized into four types: (1) concentration-dependent empirical–equation-based models (van Leussen 1994); (2) models applying a single characteristic diameter as a time-dependent variable (Winterwerp 1998, 2002; Maggi 2009); (3) distribution-based models that consider the average floc size of a continuous floc-size distribution function (Maerz and Wirtz 2009); and (4) size-class-based models assuming that floc distributions are composed of discrete size classes (Verney et al. 2010; Lee et al. 2011). Most of these models focus on tide-induced dynamics (e.g. Winterwerp, 2002; Maerz and Wirtz 2009; Maggi 2009; Verney et al. 2010; Lee et al. 2011); however, waves can also critically influence cohesive sediment transport on continental shelves (Green et al. 1995; Traykovski et al. 2007). Wright et al. (2006) included both tidal and wave velocity in their model to represent the effects of tide- and wave-supported sediment flows on shelf deposition and morphology in wave-dominated environments. Such transport is a primary cause of across-shelf transport and emplacement of flood deposits on muddy shelves.

The Belgian nearshore area is characterized by high turbidity and intense seasonal algae blooms (Lancelot et al. 1987; Fettweis et al. 2014). SPM dynamics in this area are controlled by tidal forces on calm days and by a combination of tides and waves during storms (Howarth et al. 1993). Additioniolly, human activities supply excess nutrients to coastal zones, resulting in intense algae blooms, especially during spring and early summer (Borges and Gypens 2010), making the area a relevant site to investigate links between biomass, SPM concentration and tide-wave effects. Algae release abundant sticky, gel-like organic colloids, i.e. extracellular polymeric substances (EPS) and transparent extracellular

particles (TEP) that enhance the binding strength of floc aggregations (Alldredge et al. 1993). Maggi (2009) proposed a biomineral flocculation model and validated it by using field data to study the floc behaviors in this area. However, the data were collected during calm days, and the model only considered tide-driven floc processes.

Besides the microbiological influences on flocculation, the study has also investigated the wave effects on flocculation by comparing storm and calm periods. The model (Maggi 2009), which represents a single characteristic particle and takes into account biological effect on floc dynamics was adapted to incorporate the combined effects of tides and waves. SPM particle size (D50) measured in situ in the southern North Sea (Fettweis et al. 2012; Lee et al. 2012) was used to validate our model simulations. The simulation considered both tide and tide-wave combined forcings and the biological effects on floc strength and flocculation.

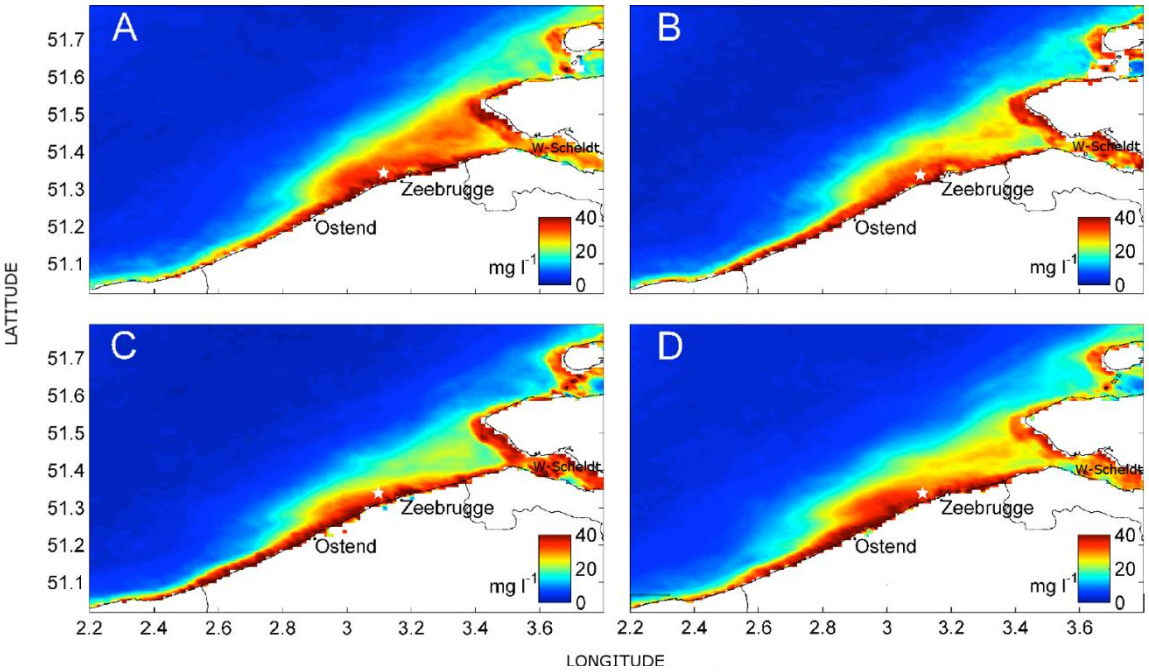

Figure 3.1: Mean surface SPM concentration (mg/l) in the southern North Sea, obtained from moderate resolution imaging spectroradiometer (MODIS) images (2002–2009) for different wind directions: (a) SW winds; (b) NE winds; (c) NW winds; and (d) SE winds (adapted from Baeye et al. 2011). The white star indicates the measuring Blankenberge is.

3.1. Study area

The measurement station Blankenberge (Figure 3.1) is situated approximately 5 km southwest (SW) of the port of Zeebrugge, Belgium. It is positioned in a turbidity maximum zone, where the water depth varies between 6 and 10 m, and the maximum tidal current can increase to more than 1 m/s (Lee et al. 2012). Zeebrugge has a semidiurnal tidal regime and a mean tidal range of 4.3 and 2.8 m during spring and neap tides, respectively. The winds predominantly blow in from the SW for 33% of the year; northeast (NE) winds are the second most predominant. The maximum wind speed coincides with SW winds; however, the highest waves occur during northwest winds (Fettweis et al. 2010). SPM concentration ranges between 20 and about 500 mg/l at the surface and between 100 and more than 5000 mg/l near the bed; lower values (<100 mg/l) occur offshore. SPM concentrations decrease during SW winds but increase during NE winds because the outflow from the Westerschelde estuary is more turbid than that from the English Channel (Baeye et al., 2011; see Figure 3.1. The SPM concentration in the high turbidity zones of the southern North Sea are inversely correlated with chlorophyll (Chl) concentration (Fettweis

et al., 2014). During the winter season (October–March) SPM concentration is high and Chl concentration is low; these conditions are reversed during the summer season (April–September), see Figure 3.2. Fettweis et al. (2014) noted that the strength of floc aggregations is controlled by the sticky organic substances associated with enhanced primary production (high Chl concentration) during the summer season

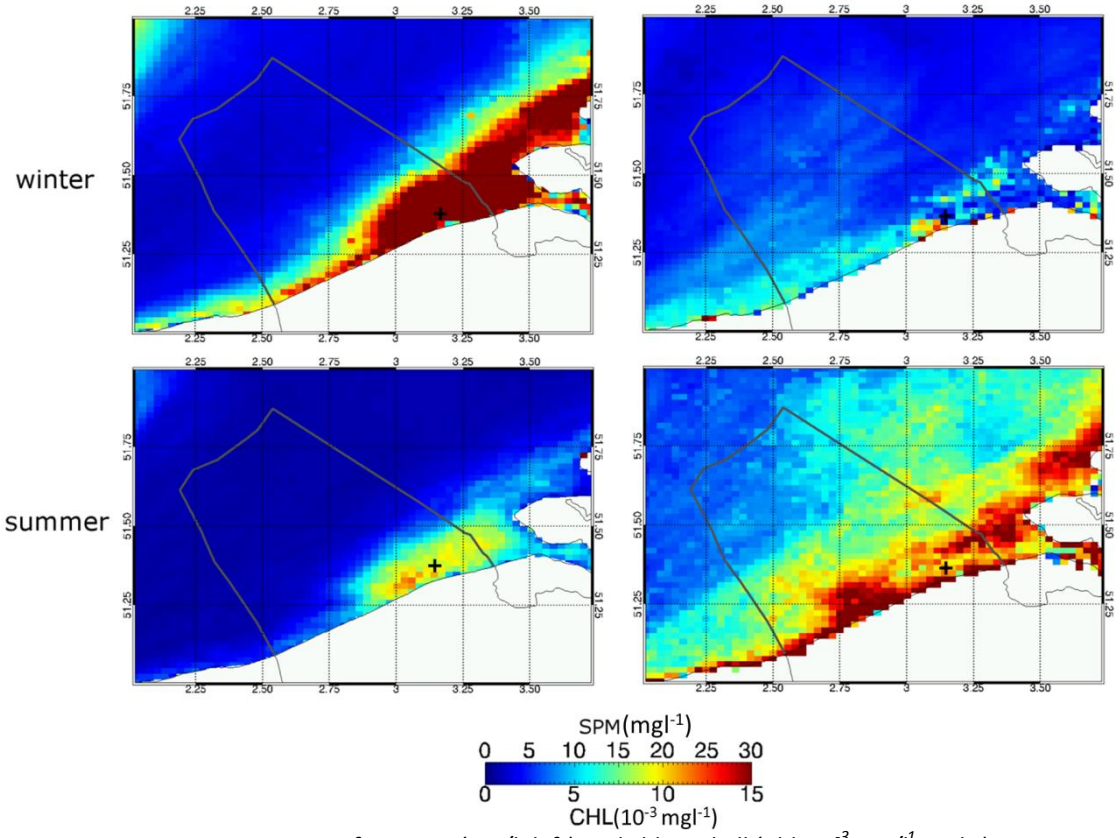

Figure 3.2: Mean surface SPM (mg/l, left) and chlorophyll (Chl, 10^{-3} mg/l, right) concentrations in the southern North Sea during the winter (October–March, top) and summer (April–September, bottom). Data were obtained from a MERIS satellite (adapted from Fettweis et al., 2014). The cross indicates the in situ measuring station Blankenberge.

3.2. Methodology

3.2.1. Field measurements

Data were collected using a multisensory benthic lander (tripod) to measure floc size, SPM concentration, and tidal currents. The tripod measuring system included a Sequoia Scientific laser in situ scattering and transmissometer 100C (LISST-100C), 3-MHz SonTek Acoustic Doppler Profiler (ADP), and two D&A optical backscatter point sensors (OBSs) (Fettweis et al. 2012). The LISST was mounted 2 m above the bed (mab), which was subsequently analyzed for particle size information (e.g., D50 and PSDs). The OBSs were installed at 0.2 and 2 mab, and their voltage was converted into SPM concentration by calibration against filtered water samples during several field campaigns (Fettweis et al. 2006). A linear regression between all OBS signals and SPM concentrations from filtration was assumed (factor =1.78). The ADP profiler was attached at 2.3 mab to measure tidal current in the lowest 2 m of the water column.

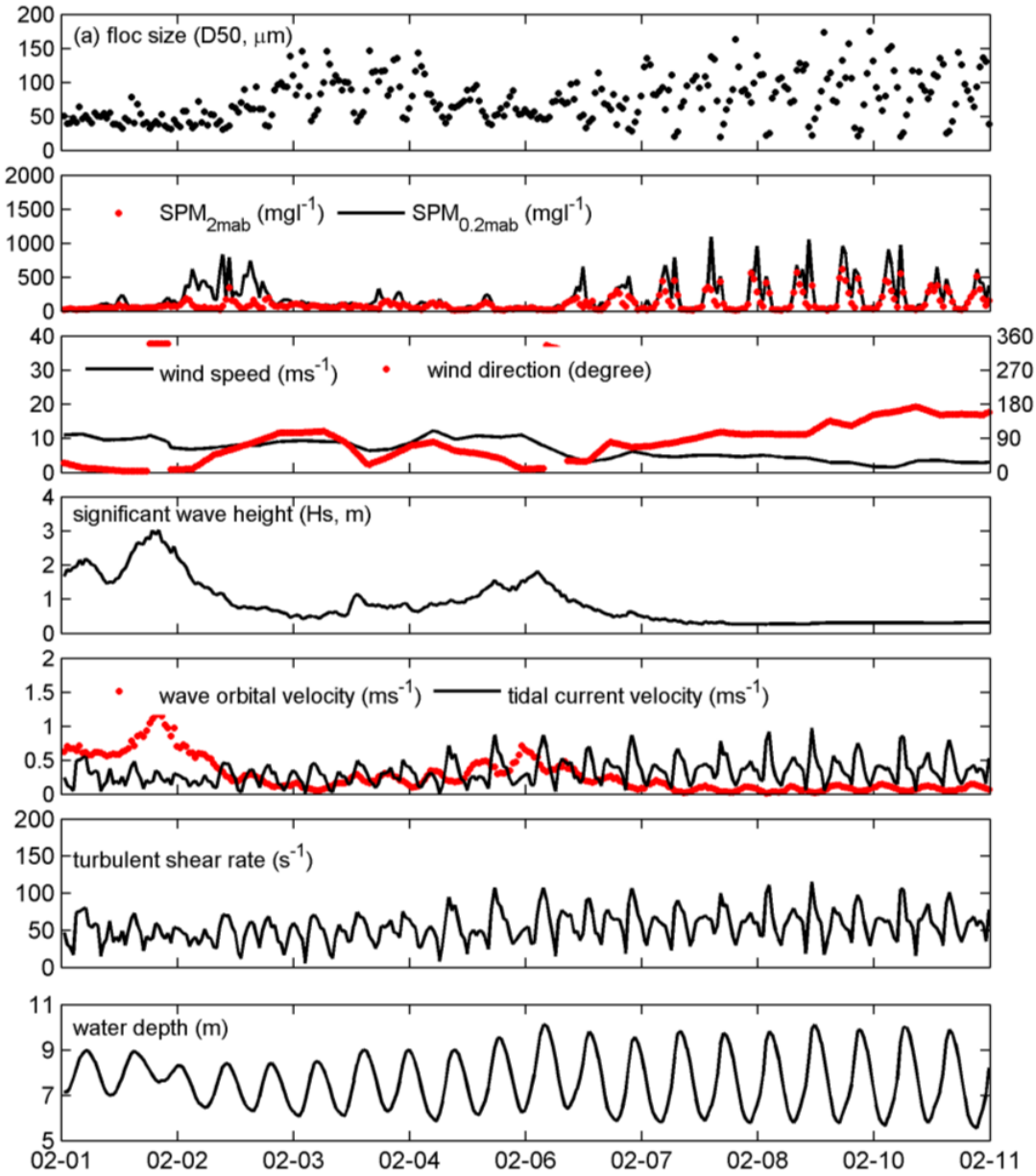

Figure 3.3: Time series of field data at the Blankenberge station for the period February 2 to 11 2008. The figure shows (from up to down) floc size (D50, μm), SPM concentration at 0.2 and 2 mab (mgl-1), wind speed (ms-1) and direction (degree), significant wave height (Hs, m), tidal and wave orbital velocities (ms-1), turbulent shear rate (s-1) and the Kolmogorov microscale (λ, μm), and water depth (m).

Measurements were taken in early 2008; the weather was stormy from February to March and calm throughout April. The environmental characteristics of storm and calm events used for the periods that have been modelled are listed in Table 3.1. The first storm (February 1 and 2) occurred during a neap tide and caused significant wave heights (Hs) of up to 2.8 m. By contrast, the Hs during the second storm (February 5–7) reached 1.5 m (Figure 3.3). The winds blowing from the SW–W during both of these storms produced a positive (northward) subtidal alongshore flow; all storms with these characteristics were named SW-ward storms (SW storms) in this study.

In March, three storm events occurred (Figure 3.4). The first event took place between March 10 and 13, producing a H_s of 2.5 m, and was also classified as SW storm. The storm of March 16 to 19 and March 21 to 25 were mainly generated by northerly wind resulting

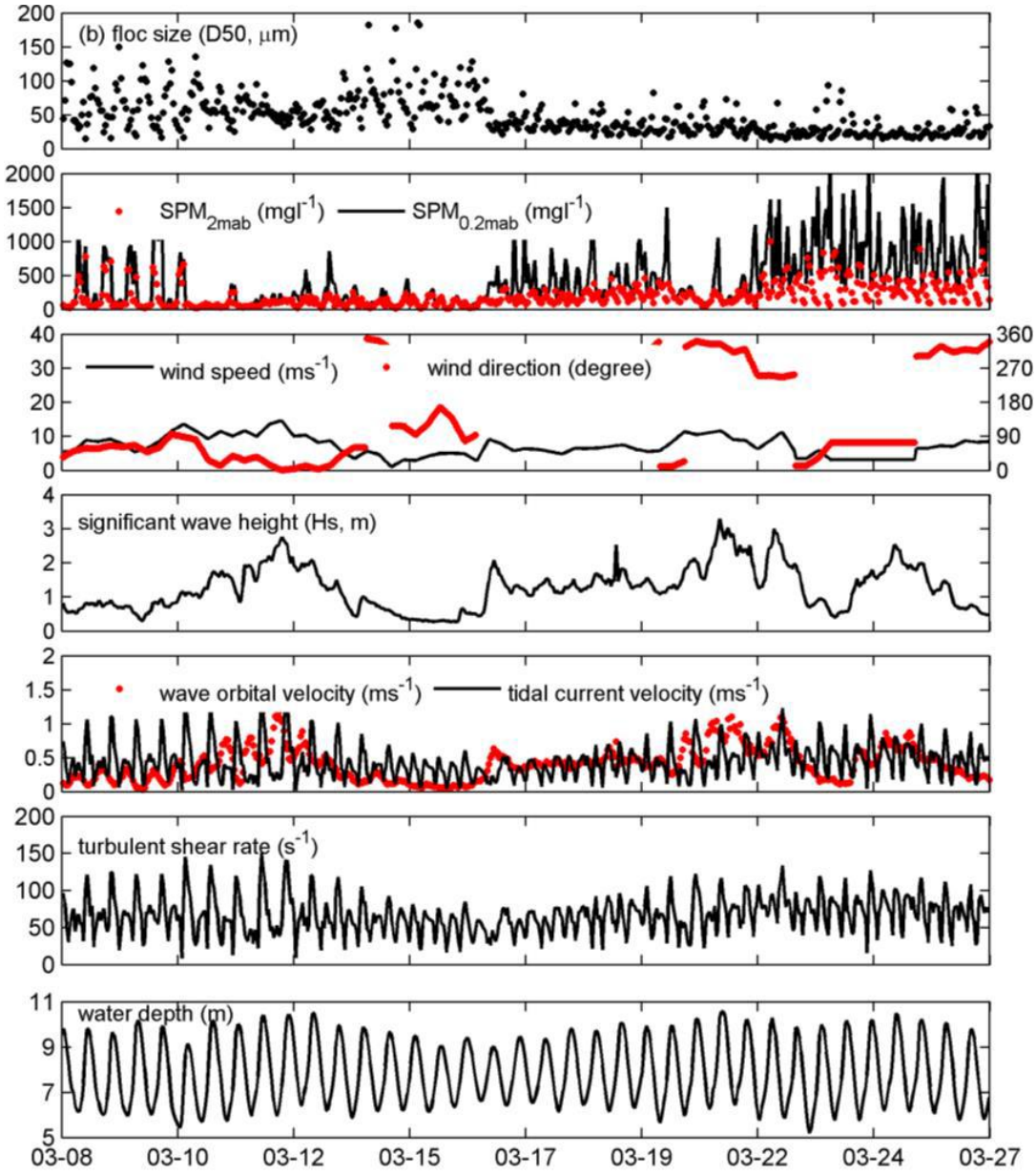

Figure 3.4: Time series of field data at the Blankenberge station for the period March 8 to 27 2008. The figure shows (from up to down) floc size (D50, μm), SPM concentration at 0.2 and 2 mab (mgl-1), wind speed (ms-1) and direction (degree), significant wave height (Hs, m), tidal and wave orbital velocities (ms-1), turbulent shear rate (s-1) and the Kolmogorov microscale (λ, μm), and water depth (m).

in negative (southward) subtidal alongshore flows directed toward the SW; all storms with these characteristics were named NE-ward storms (NE storms) in this study. The maximum Hs of the two NE storms reached 2.0 and 3.0 m, respectively.

Overall, the measurements indicated that a unimodal PSD of granular particles (mean value of approximately 50 μm) occurred during the SW storms (Figures 3.6a–c and Table 3.1), and that a multimodal PSD of mixed sediments (mean value D50 ≤ 50 μm) occurred during the NE storms (Figures 3.6d-e, and Table 3.1). For comparison, field data for a calm event during blooms from April 26–30 were subsequently collected, where the Hs was less than 0.5 m (Figure 3.5).

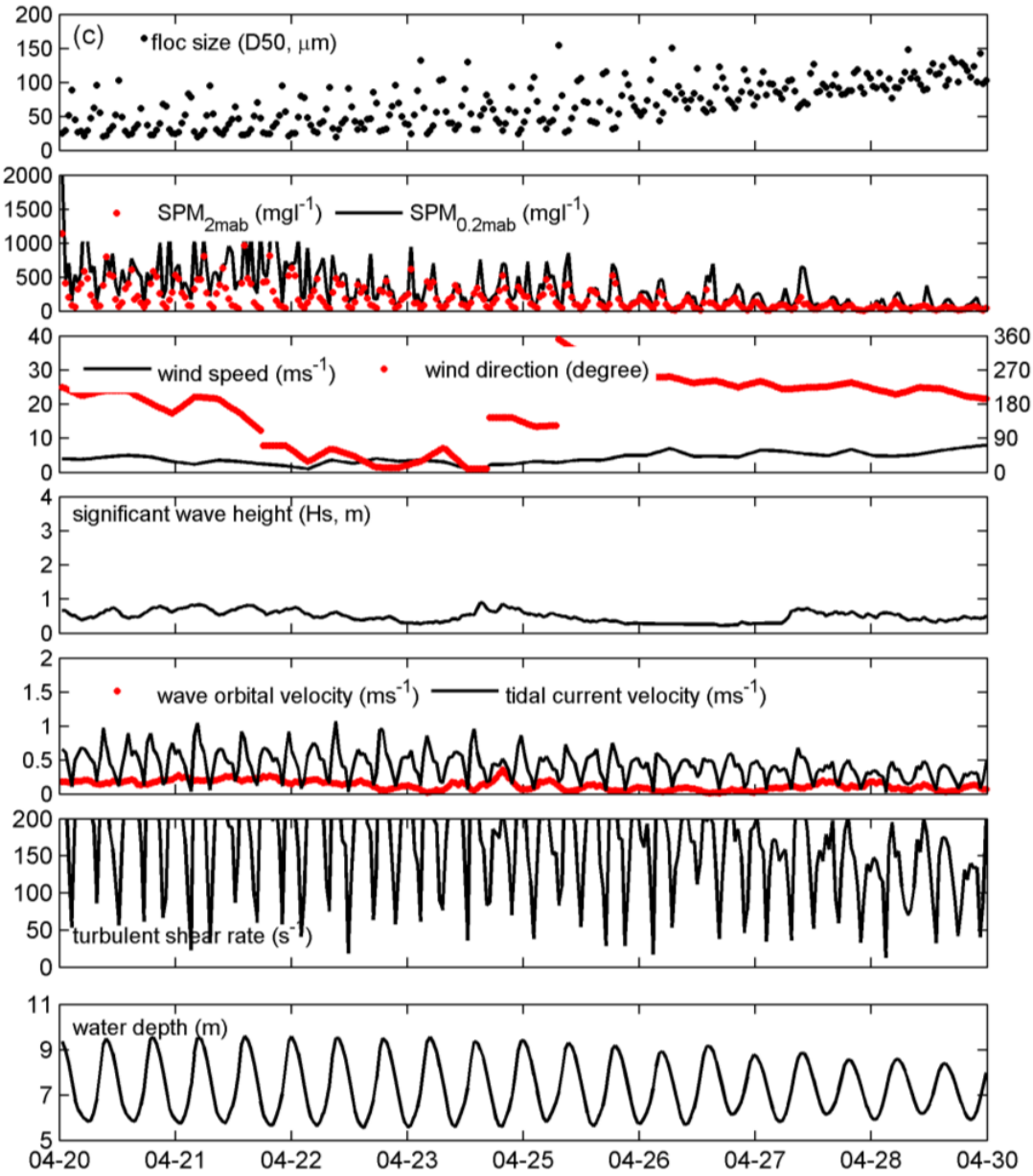

Figure 3.5: Time series of field data at the Blankenberge station for the period April 20 to 30 2008. The figure shows (from up to down) floc size (D50, µm), SPM concentration at 0.2 and 2 mab (mgl-1), wind speed (ms-1) and direction (degree), significant wave height (Hs, m), tidal and wave orbital velocities (ms-1), turbulent shear rate (s-1) and the Kolmogorov microscale (λ, µm), and water depth (m).

Table 3.1: Environmental characteristics of storm events in February, March and April

	1–2 Feb	5-7 Feb	10–13 Mar	16–19 Mar	21–25 Mar	26–30 Apr
Storm	SW	SW	SW	NE	NE	-
Wind speed (ms^{-1})	9.2	7.4	10.8	6.1	6.9	4.2
Tidal type	neap	spring	spring	mean	spring	mean
Max. H_s (m)	2.8	1.5	2.5	2.0	3.0	0.42
D50 (µm)	46	67	56	48	26	98
PSD	Unimodal	Unimodal	Unimodal	Multimodal	Multimodal	Multimodal

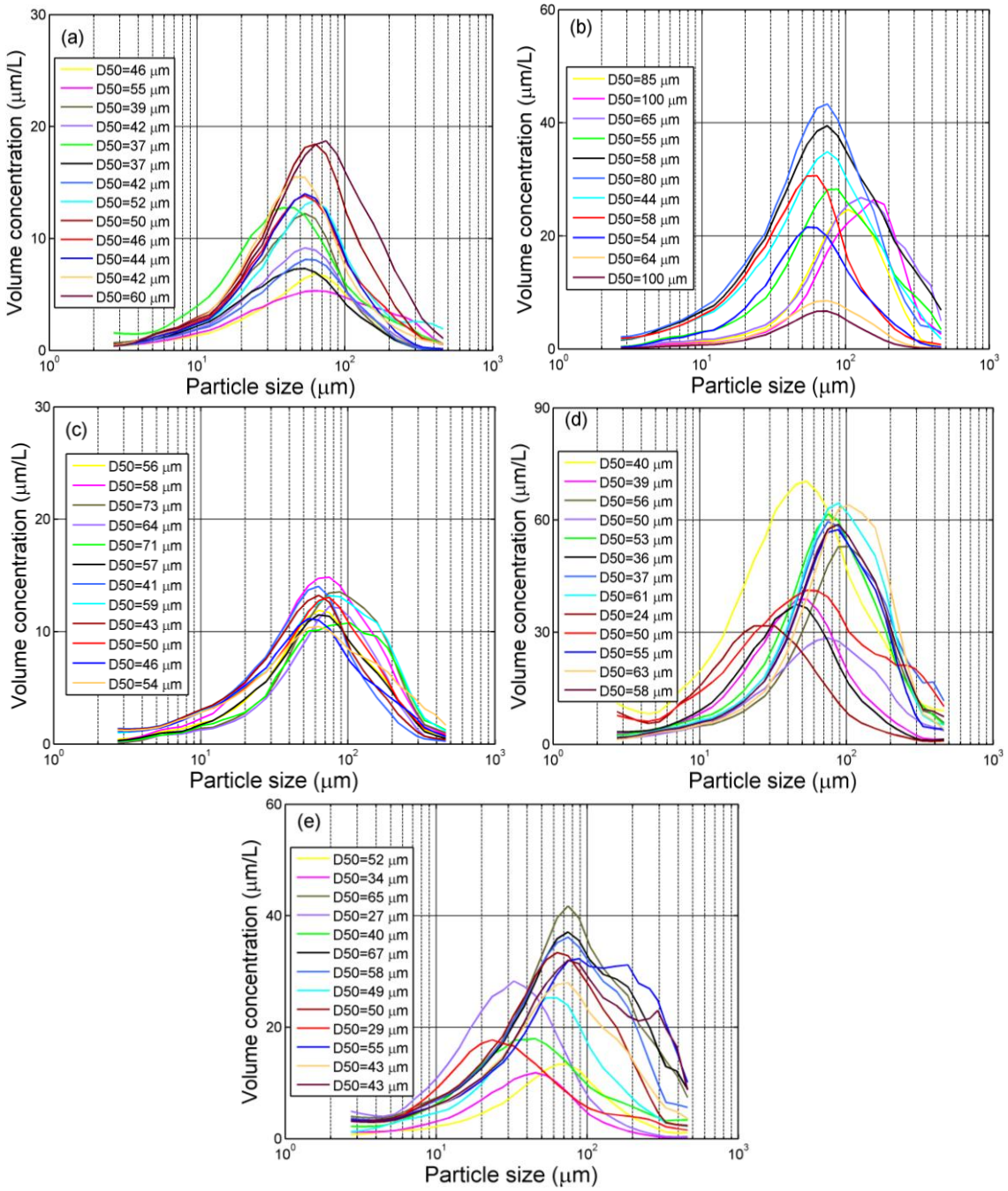

Figure 3.6: Hourly particle-size distribution (PSD) during a tidal cycle and during different storm events. (a) February 1 to 2, (b) February 5 to 7, (c) March 10 to 13, (d) March 16 to 19, and (e) March 21 to 25.

3.2.2. Model setup and parameterization

To investigate storm-influenced flocculation in the highly productive southern North Sea, the biomineral flocculation model of Maggi (2009) was further complemented by to include both tide- and wave-induced forcing. Finally, a model parameterization procedure was applied to ensure that the simulation results aligned with the measured data.

3.2.2.1. Flocculation model

The flocculation model includes mineral and biomass fractions. In particular, the biomass fraction considers the microbial effects (e.g., EPS, TEP, organic residues, and excreta) on floc-binding strength (Kiorboe et al. 1990). The floc solid volume V is the sum of mineral

volume (VM) and biomass volume (VB); the time derivative of floc volume is expressed as follows (see Table 3.2 for the description of the variables):

$$\mathrm{dV/dt} = \mathrm{dV_M/dt} + \mathrm{dV_B/dt} \tag{3.1}$$

$$\frac{\mathrm{dV_M}}{\mathrm{dt}} = (1-\alpha)\mathrm{nf}\frac{\mathrm{D^{nf-1}}}{\mathrm{D_p^{nf-3}}}\frac{\mathrm{k_a C_M G}}{\mathrm{D^{nf-4}}} - (1-\alpha)\mathrm{nf}\frac{\mathrm{D^{nf-1}}}{\mathrm{D_p^{nf-3}}}\frac{\mathrm{k_b}(1-\alpha)\mathrm{G}^{3/2}}{(\mathrm{D-D_p})^{\mathrm{nf-3}}}\mathrm{D}^2 \tag{3.2}$$

$$\frac{\mathrm{dV_B}}{\mathrm{dt}} = \alpha\mathrm{nf}\frac{\mathrm{D^{nf-1}}}{\mathrm{D_p^{nf-3}}}\frac{\mathrm{k_a C_B G}}{\mathrm{D^{nf-4}}} - \alpha\mathrm{nf}\frac{\mathrm{D^{nf-1}}}{\mathrm{D_p^{nf-3}}}\frac{\mathrm{k_b}\alpha\mathrm{G}^{3/2}}{(\mathrm{D-D_p})^{\mathrm{nf-3}}}\mathrm{D}^2 + \eta\mathrm{V_B}\left(1-\frac{\mathrm{V_B}}{\mathrm{K}}\right) \tag{3.3}$$

Variations in both mineral volume (dV_M/dt) and biomass volume (dV_B/dt) depend on floc aggregation and breakage of floc particles (Equations 3.2 and 3.3). The change in aggregation volume ($dV_{aggregation}$) and breakage volume ($dV_{breakage}$) in the whole floc volume is controlled by the turbulence shear rate (*G*) and can be written as

$$\mathrm{dV_{aggregation}} = \mathrm{dt}\left[(1-\alpha)\mathrm{nf}\frac{\mathrm{D^{nf-1}}}{\mathrm{D_p^{nf-3}}}\frac{\mathrm{k_a C_M G}}{\mathrm{D^{nf-4}}} + \alpha\mathrm{nf}\frac{\mathrm{D^{nf-1}}}{\mathrm{D_p^{nf-3}}}\frac{\mathrm{k_a C_B G}}{\mathrm{D^{nf-4}}}\right] \tag{3.4}$$

$$\mathrm{dV_{breakage}} = \mathrm{dt}\left[(1-\alpha)\mathrm{nf}\frac{\mathrm{D^{nf-1}}}{\mathrm{D_p^{nf-3}}}\frac{\mathrm{k_b}(1-\alpha)\mathrm{G}^{3/2}}{(\mathrm{D-D_p})^{\mathrm{nf-3}}}\mathrm{D}^2 + \alpha\mathrm{nf}\frac{\mathrm{D^{nf-1}}}{\mathrm{D_p^{nf-3}}}\frac{\mathrm{k_b}\alpha\mathrm{G}^{3/2}}{(\mathrm{D-D_p})^{\mathrm{nf-3}}}\mathrm{D}^2\right] \tag{3.5}$$

Moreover, $C_M = (1-\delta)C$ is the concentration of the SPM mineral fraction (δ = biomass fraction) and $\alpha = V_B/V$ is the floc biomass volume fraction. The aggregation rate (k_a) and breakup rate (k_b) functions are expressed as follows:

$$\mathrm{k_a} = (1+\alpha)\mathrm{k'_a}\frac{1}{\rho\,\mathrm{D_p^{3-nf}nf}} \tag{3.6}$$

$$\mathrm{k_b} = (1+\alpha)\mathrm{k'_b}\frac{1}{\mathrm{D_p^{3-nf}nf}}\left(\frac{\mu}{\mathrm{F_y}}\right)^{1/2} \tag{3.7}$$

where k'_a and k'_b are dimensionless aggregations and breakup calibration parameters, μ is the dynamic viscosity of water, and F_y is the floc strength. Additionally, ρ is the average density of the floc solid volume, which is computed as

$$\rho = (1-\alpha)\rho_\mathrm{M} + \alpha\rho_\mathrm{B} \tag{3.8}$$

where ρ_M and ρ_B are the mineral and biomass densities, respectively.

Microorganism growth affected the floc volume growth; the $\eta V_B\left(1-\frac{V_B}{K}\right)$ introduced in Equation 3.3 represents the microbial effects, where the specific growth rate (η) is expressed as follows:

$$\eta = \eta_\mathrm{max}\frac{\mathrm{N}}{\mathrm{N+k_m}} \tag{3.9}$$

where η_{max} is the maximum specific growth rate, *N* is the nutrient concentration, and k_m is the half-saturation concentration. Additionally, the floc-carrying capacity to express the maximum biomass volume in the aggregate microenvironment can be calculated as

$$\mathrm{K} = \beta\mathrm{V_p} = \beta(\mathrm{D^3} - \mathrm{V}) \tag{3.10}$$

where V_p is the floc pore volume and β is a dimensionless factor.

Thus, the single characteristic floc size (*D*) is obtained from the time-varying rate of the mineral and biomass volumes (dV_m/dt and dV_B/dt, respectively) in this model:

$$\mathrm{D} = \left(\mathrm{V/D_p^{nf-3}}\right)^{1/\mathrm{nf}} \tag{3.11}$$

where D_p is the primary particle size and *nf* is the fractal dimension. All of the parameters used in our SPM flocculation model are defined in Table 3.2.

Table 3.2: Definition of the model parameters.

Symbol	Unit	Definition	Symbol	Unit	Definition
D	[μm]	Floc size	t	[h]	Time
D_p	[μm]	Primary particle size	k'_a	[—]	Aggregation calibration parameter
nf	[—]	Fractal dimension	k'_b	[—]	Breakup calibration parameter
V	[mm^3]	Floc volume	F_y	[N]	Floc strength
V_M	[mm^3]	Floc mineral volume	η	[s^{-1}]	Specific growth rate
V_B	[mm^3]	Floc biomass volume	η_{max}	[s^{-1}]	Maximum specific growth rate
α	[—]	Floc biomass volume fraction	N	[mol l^{-1}]	Nutrient concentration
C	[g l^{-1}]	SPM concentration	k_m	[M]	Half-saturation concentration
C_M	[g l^{-1}]	SPM mineral concentration	K	[mm^3]	Floc carrying capacity
C_B	[g l^{-1}]	SPM biomass concentration	β	[—]	Factor
δ	[—]	SPM biomass fraction	G	[s^{-1}]	Turbulent shear rate
ρ	[kg m^{-3}]	Floc specific weight	μ	[kg $m^{-1}s^{-1}$	Water dynamic viscosity
ρ_M	[kg m^{-3}]	Mineral specific weight	v	[m^2s^{-1}]	Kinematic viscosity
ρ_B	[kg m^{-3}]	Biomass specific weight	λ	[μm]	Kolmogorov microscale

3.2.2.2. Combined dynamics of tides and waves

The effect of waves on flocculation is critical in storm-dominated environments. Wright et al. (2006) proposed that tides, waves, and gravity currents cause sediment transportation in a shelf sea, which can be calculated using the following equation:

$$\mathrm{U} = \sqrt{\mathrm{U_c^2} + \mathrm{U_w^2} + \mathrm{U_g^2}} \tag{3.12}$$

where U_c is the tidal current velocity, U_w is the wave orbital velocity, and U_g is the gravity current velocity. The latter can be disregarded for the flat-slope Belgian near-shore zone.

The tidal current velocity (U_c) was measured using an ADP. The wave orbital velocity (U_w) was calculated based on Soulsby (1997) who suggested that U_w can be characterized by its standard deviation (U_{rms}). This can be calculated from the wave height–period–velocity curve of the Joint North Sea Wave Project (JONSWAP) spectrum. The JONSWAP spectrum was established on the basis of wave measurements from the southern North Sea.

The turbulent shear rate (G) used in Equations 3.2 and 3.3 was obtained by calculating $G = v/\lambda^2$, where v is the kinematic viscosity. Notably, the Kolmogorov microscale (λ) is highly correlated with the current velocity (U) (Winterwerp, 1998). λ and U in the Belgian shelf sea were obtained using the 3D-COHERENS model. The results indicated that λ was inversely proportional to U and varied with the weather conditions (Equations 3.14 and 3.15). When only the tide-driven forces are considered, the Kolmogorov microscale (λ) is expressed as follows:

$$\lambda = 374.71\mathrm{U}^{-0.43} \tag{3.14}$$

where $U = U_c$, and R^2=0.86. However, when the combined velocity of tides and waves is considered, the Kolmogorov microscale (λ) is expressed as follows:

$$\lambda = 405.24\mathrm{U}^{-0.32} \tag{3.15}$$

where U is a combined velocity as represented in Equation 3.13, and R^2=0.90

3.2.2.3. Model parameterization

To determine the appropriate values of the model parameters for specific sites, the Monte Carlo method was used to analyze the sensitivity of the model to parameter changes (the calibrated parameters are listed between brackets in Table 3.3). Standard deviation was calculated considering 20% of each parameter.

The results revealed that the values of the model parameters for the present study site (BLA) were consistent with those measured in Zeebrugge, as reported by Maggi (2009). Additionally, the model was based on the conception of a single characteristic particle size to describe the floc geometric characteristics (i.e., primary particle size and fractal dimension) similar as in Maggi (2009). Therefore we evaluated the parameters used by Maggi (2009). The model parameter values used in the present study are listed in Table 3.3.

To test the model, each dataset simulation (Table 3.1) was calibrated on a set of full-cycle (13-hour) tidal data, and validated through other measurements. The time series of simulated floc particles during different weather conditions is depicted in Figure 3.5, where gray blocks represent the calibration periods and white blocks represent the validation periods). Finally, basic statistical analysis (the root mean square error, RMSE) was used to evaluate the simulation results.

Table 3.3: Summary of the model parameters used.

Parameter	*Unit*	*Value*	*Parameter*	*Unit*	*Value*
D_p	[μm]	2.0	k'_a	[—]	0.189
nf	[—]	2	k'_b	[—]×10^{-6}	11.41
δ	[—]	0.04	k_m	[M]×10^{-6}	1.159
V_M	[mm^3] ×10^{-8}	2.0	η_{max}	[s^{-1}]×10^{-4}	6.586
V_B	[mm^3] ×10^{-8}	1.0	F_y	[N]×10^{-11}	3.0
ρ_M	[kg m^{-3}]	2650.0	N	[M]×10^{-6}	20.0
ρ_B	[kg m^{-3}]	1025.0	β	[—]	0.226
μ	[kg $m^{-1}s^{-1}$]×10^{-3}	1.0	ν	[m^2s^{-1}] ×10^{-6}	1

3.3. Results

Two dynamic conditions were simulated using our SPM flocculation model. We considered tidal velocity alone (Equation 3.14) in the first condition, and included both wave and tidal velocities (Equation 3.15) in the second condition to evaluate the effect of waves on storm-influenced flocculation. SPM concentration at 2 mab and tidal current velocity were used as input data in modeling.

3.3.1. Calm-day simulation

On calm days, the tidal current was the dominant hydrodynamic force, as indicated in Figure 3.5, and both wave height and orbital velocity were small. The results revealed that the simulation obtained by considering tidal dynamics alone aligned with the measured data (Figure 3.7a). Specifically, a RMSE of 23 $\pm$ 2 μm was obtained through the tide-only dynamic condition and a larger RMSE (30 $\pm$ 5 μm) was obtained through the combined tide–wave dynamic condition. Thus, a tide-induced dynamic condition is most suitable for calm-day simulation.

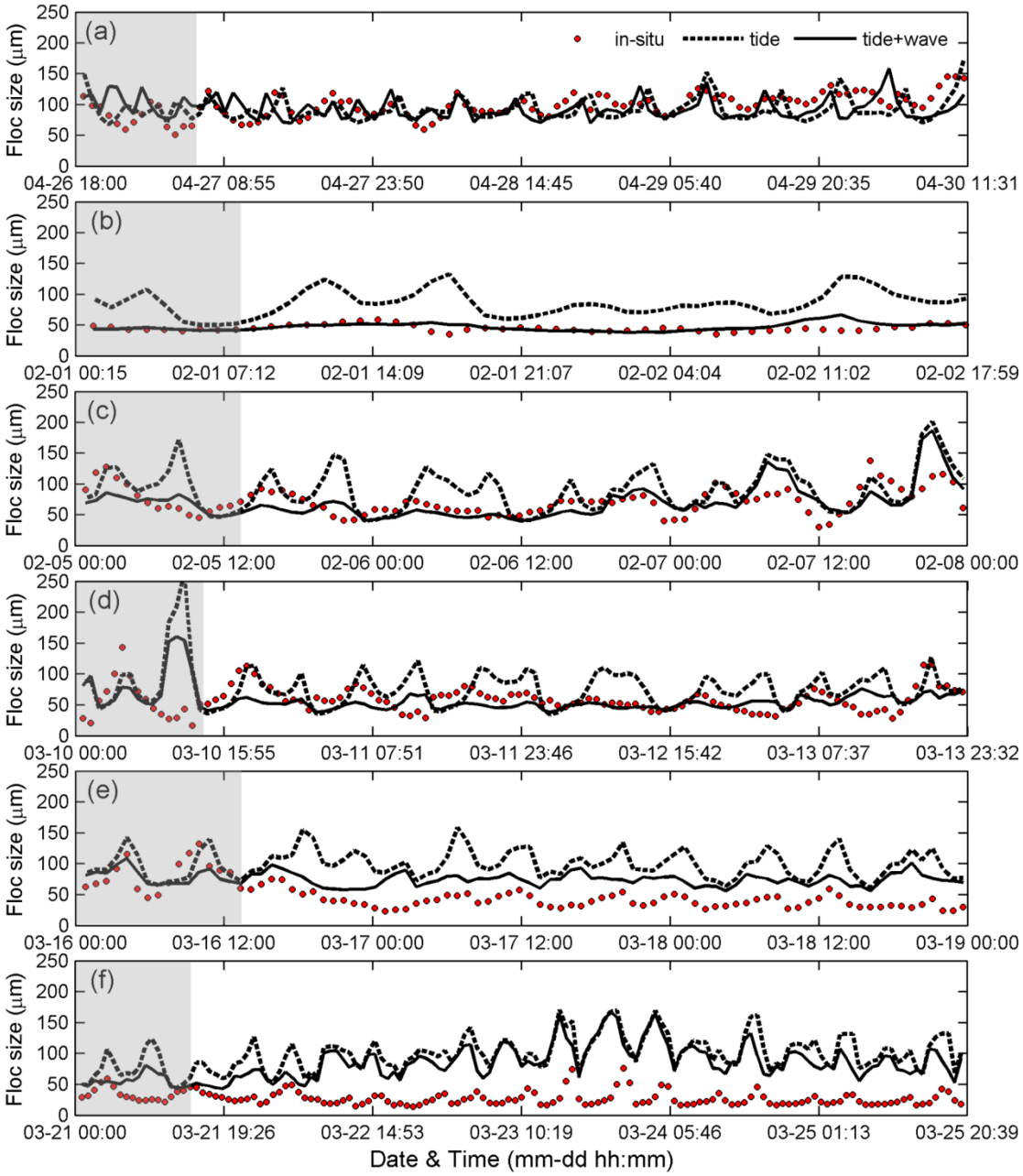

Figure 3.7: Measured (dots) and simulated values of floc size (µm) under tide (dashed line) and combined tide–wave (solid line) forcing during (a) the calm events from April 26 to 30, and the storm events in (b) February 1 to 2, (c) February 5 to 7, (d) March 10 to 13, (e) March 16 to 19, and (f) March 21 to 25. The grey shaded period has been used for calibrating the model.

3.3.2. Storm simulations with tidal dynamics

The floc particles were smaller and the turbulent shear during H_s (> 1.5 m) was stronger during the storm days than during calm days (Figures 3.3 and 3.4). However, the model predicted particle sizes for the storm events obtained by considering tidal dynamics alone were larger than the measured D50 (Figure 3.7b-f). Overestimations mainly occurred in the simulations of fine particles (D_{field}, <50 µm; Figure 3.8a-b). The RMSEs of all storm simulations were higher than 44 µm, and the highest RMSE (87 $\pm$ 10 µm) occurred during the March 21–25 storm (Table 3.4).

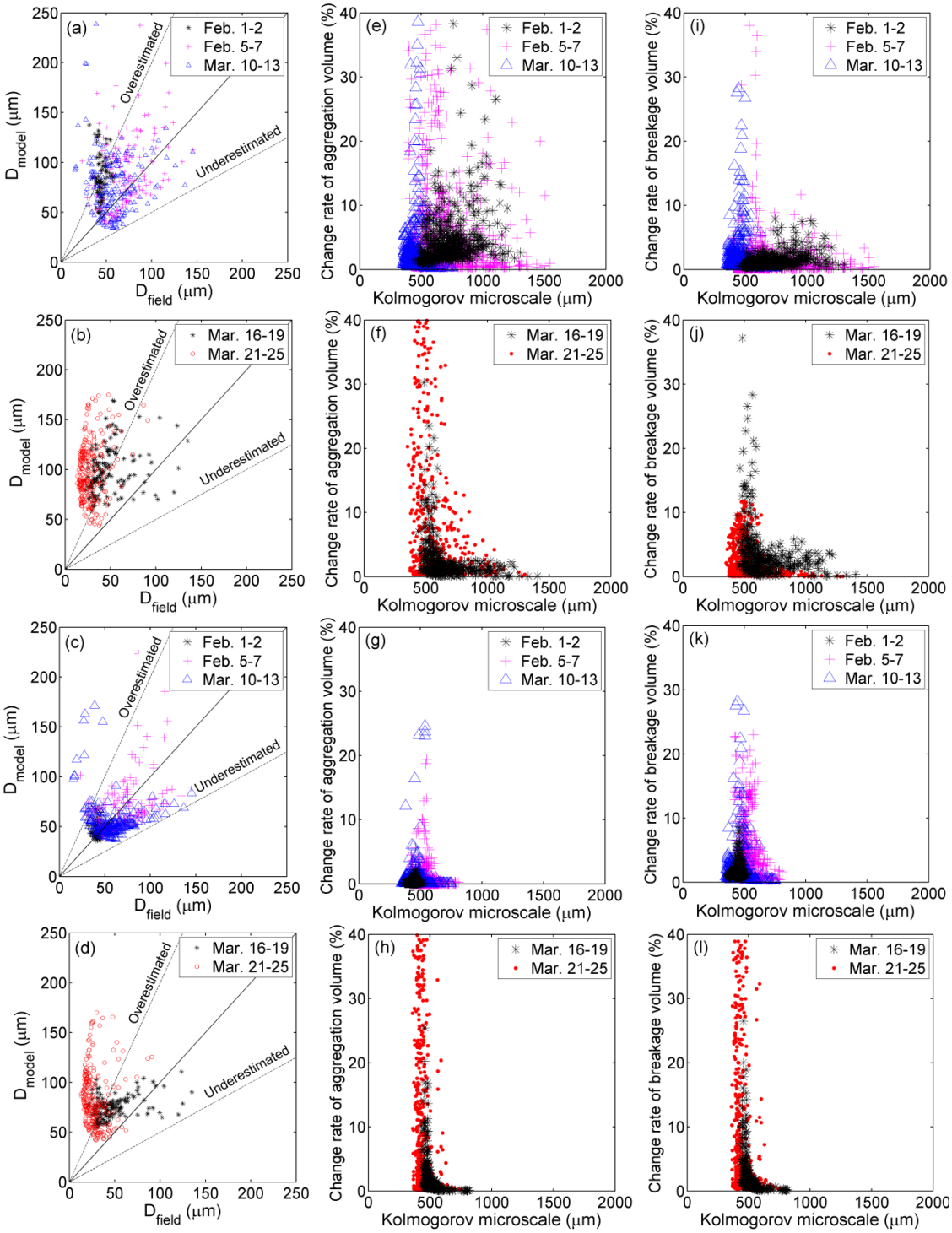

Figure 3.8: ***Left****: Comparison of the modeled and measured floc sizes during (a) SW storms, (b) NE storms when only tide-induced dynamics was considered, (c) SW storms, and (d) NE storms when tide–wave-induced dynamics was considered.*

Middle: *Correlation between the Kolmogorov microscale and the rate of change for the aggregation volume per measured floc volume during (e) SW storms, (f) NE storms when only tide-induced dynamics was considered, (g) SW storms, and (h) NE storms when tide–wave-induced dynamics was considered.*

Right: *Correlation between the Kolmogorov microscale and the rate of change for the breakage volume per measured floc volume during (i) SW storms, (j) NE storms when only tide-induced dynamics was considered, (k) SW storms, and (l) NE storms when tide–wave-induced dynamics was considered.*

The large Kolmogorov microscale (500–1500 µm; Figure 3.8e, f, i, j) indicates that a small turbulent shear occurred when considering tidal dynamics alone. These smaller hydrodynamic forces accelerated the aggregation mechanism (i.e., a higher rate of change for the aggregation volume, $dV_{aggregation}/V_{field}$; Figure 3.8e-f), but decreased the breakage mechanism (i.e., a lower rate of change for the breakage volume, $dV_{breakage}/V_{field}$; Figure 3.8i-j). Even the spring tidal force (i.e., those simulations from February 1 to 2, March 10 to 13 and March 21 to 25) was insufficient to break floc particles during storms when tidal currents were the only hydrodynamic force included in the model.

3.3.3. Storm simulations with combined tide–wave dynamics

By accounting for the effect of wave orbital motion on flow velocity in our model, we obtained improved results that more accurately represented the measured floc size, compared with the purely tidal-driven modeling (Figure 3.7b–f and Figure 3.8c-d). Specifically, the smaller Kolmogorov microscale (high turbulent shear), which was governed by the combined tide–wave velocity, enhanced the fractions of the floc volume with sufficient breakage forces. In other words, the rate of change for the breakage and aggregation volume increased and decreased, respectively (Figure 3.8g, 3.8h, 3.8k, and 3.8l).

Overall, combining the dynamic conditions in the model more accurately represented the measured data, particularly during SW storms. The highest accuracy was obtained in the simulations from February 1 and 2, where the RMSE was 13 µm, followed by those from February 5 to 7 and from March 10 to 13 (Table 3.4). However, the simulations of NE storms were less consistent with measured D50 (Figure 3.6e-f); in these situations, the model overestimates the measurements (Figure 3.7d) and the RMSE exceeded 40 µm.

The aforementioned results indicated that the turbulent shear generated by tidal currents, which dominated floc dynamics on calm days, was insufficient to force floc breakup under storm conditions. As detailed in Table 3.1, this can be observed from the small particles (<50 µm) in measured data. Finally, we compared the RMSEs of both dynamic conditions during storm events and determined that the average RMSE value decreased from 67 µm (tide-only dynamic) to 32 µm (combined dynamic), revealing a 50% modeling improvement through a wave-induced turbulent shear.

Table 3.4: Root mean square error and simulation error in floc size (refers to the difference between field and model floc size) on tide-induced and combined tide–wave velocity. F_y, floc strength (N); F, field data; M, model results

Month	*February*			*March*	
Date	*1–2*	*5–7*	*10–13*	*16–19*	*21–25*
Tide-induced dynamics (referred to the study of Maggi, 2009)					
$F_y = 3 \times 10^{-11}$, RMSE (µm)	68	61	45	75	87
Tide-wave dynamics					
$F_y = 3 \times 10^{-11}$, RMSE (µm)	13	23	22	40	62
F − M < − 10 µm (%)	28	25	24	88	99
|F − M| ≤ 10 µm (%)	60	31	38	6	1
F − M > 10 µm (%)	12	44	38	6	0
$F_y = 1 \times 10^{-11}$, RMSE (µm)	13	23	23	23	36
$F_y = 5 \times 10^{-11}$, RMSE (µm)	28	41	40	55	85

3.4. Discussion

The model results represented that the turbulent shear generated by tidal currents dominated floc dynamics on calm days. The tide–wave-combined turbulence must be incorporated when simulating flocculation in a tide–wave-dominated environment. The results also indicated that the hydrodynamic force causes the discrepancies between the model results and observations under the storm conditions, even during the calibration period.

To explore the difference in floc behaviors during the NE and SW storms, this section discusses the factors governing the sediment sources and the transport processes at BLA. Additionally, the variations in floc strength among the seasons were estimated to further enhance our model's accuracy.

3.4.1. Floc behaviors under different storm conditions

In the southern North Sea, winds dominate the subtidal alongshore flow and change the flocculation mechanisms during storms (Baeye et al. 2011; Fettweis et al. 2012). Therefore, even under identical hydrodynamic conditions (e.g. tides and waves), the floc size distributions can have distinct variations depending on the storm directions. For instance, the storm events from March 10 to 13 and March 21 to 25 had similar hydrodynamic conditions (spring tide, Hs>2.5 m) but different storm directions (SW and NE, respectively); the D50 during these two storms was also different (Table 3.1). Specifically, the average D50 during the SW storm was 56 µm (unimodal PSD; Figure 3.8c), whereas that of the NE storm was only 26 µm (multimodal PSD; Figure 3.8e). This can be explainded by the occurrence of granular particles (silt and sand) eroded and resuspended from the seabed by wave orbital stress during SW storms with a NE-directed alongshore subtidal current (Fettweis et al. 2012). Furthermore, the SPM consisted of mixed cohesive and non-cohesive particles resulting in more unimodal PSDs. The model behavior coincides with this unimodal PSD during SW storms (Figure 3.8a–c).

However, the subtidal alongshore flow directions during NE storms exhibited floc characteristics entirely different from those during SW storms. The alongshore flows during NE storms caused the resuspension of soft mud deposits located in the navigation channels and the adjacent areas and a stronger outflow of SPM from the Westerschelde estuary (Figure 3.1). Fettweis et al. (2010, 2012) also noted an increase in the cohesive SPM concentration, the formation of HCMSs, causing an armoring of the sand. These pure cohesive particles are indicated by the presence of multimodal PSDs, which contain many small-sized particles (i.e., high tails of small PSDs; Figure 3.8d-e). Thus, because the applied model is based on a single characteristic diameter of floc dynamics, it is appropriate for simulating particles with unimodal PSDs but less accurate for particles that exhibit multimodal behaviors.

3.4.2. Seasonal floc strength

Charged particles in suspension, such as clays or exopolymers, may become attached to each other and to other particles to form flocs with compositions, sizes, densities, and structural complexities that vary as a function of turbulence and bio-chemical composition (e.g. Pavoni et al. 1972; Eisma 1986; Winterwerp 1998; Droppo 2001; Mietta et al. 2009; Tan et al. 2012; Maggi and Tang 2015). The algae bloom and associated biological activities have been connected to an enhancement in the production of particle-binding microbial exudates such as TEPs (Alldredge et al. 1993; Logan et al. 1995; Engel 2000; Passow et al. 2001). TEPs may increase not only the floc size and but also the floc strength, resulting in the formation of larger amounts of macroflocs (Lee et al. 2012; Fettweis et al. 2014). The existence of macroflocs has been demonstrated for both open oceans and turbid coastal and estuarine environments (e.g. Alldredge et al. 1993; Jago et al. 2007). In turbid coastal

and estuarine environments, such as the southern North Sea, the phytoplankton bloom is affected by the high nutrient availability and affects SPM dynamics (Lacroix et al. 2007). An experimental study reported that the average settling velocity of the larger biomass-affected flocs was nearly equal to that of the smaller biomass-free flocs because of the opposing effects of floc size and density (Tang and Maggi 2016); however, in situ measurements suggest that flocs during spring and summer are larger and settle faster than flocs during winter (Fettweis et al. 2014). During spring and summer when TEPs are more abundant, the SPM concentration reduces, thus increasing the light conditions, which further enhances algal growth (Desmit et al. 2005). Lower SPM concentrations and higher Chl concentrations in summer have been observed at the measuring size, as shown in Figure 3.2. By contrast, low solar radiation decelerates physical (e.g., thermal stratification, light, and temperature) and biological (e.g., primary production) processes during winter, thus reducing primary production and the release of exopolymers (Droppo et al. 2005; Fettweis et al. 2014). Because the biological effects on floc dynamic are complicated and not yet fully understood, we used floc strength to investigate their effects on seasonal floc-size variations.

To investigate the seasonal signal of floc-binding ability, various floc strengths were used to test and estimate the model's accuracy across seasons. First, we tested the situations without floc strength (F_y = 0 N) to understand the effect of floc strength on floc dynamic. The floc strength that has been suggested in theoretical (Matsuo and Unno 1981) and experimental (Van Leussen, 1994) studies is approximately 10^{-11} N. Therefore, four floc strength values were applied to our model, including 0 N (without floc strength), 1×10^{-11} N, 3×10^{-11} N (Maggi 2009), and 5×10^{-11} N (Table 3.4). Compared with field data, the simulations without floc strength (0 N) had deviations (RMSEs large than 100 μm) whether under tidal-only or by combining dynamic systems. The results without floc strength indicated that floc strength is a key factor in determining floc particle evolution. Meanwhile, the simulations of summer conditions (April case) were obtained using 3×10^{-11} N, and were closer to the measured data than those obtained using the other two floc strength values (Table 3.4 and Figure 3.9a). The inverse relationship between floc strength and the breakage rate (Equation 3.7) implies that the breakage rate decreases as floc strength increases. Additionally, a gradually increasing trend in D50 floc size (Figure 2.5) revealed that the floc aggregation mechanism was stronger than the breakage mechanism in the summer. Therefore, a floc strength of 3×10^{-11} N is appropriate for representing summer conditions.

By contrast, using a smaller floc strength (1×10^{-11} N) significantly improved the simulation for winter conditions (February and March cases; Table 3.4 and Figure 3.9b–f) because of the small floc particles, which indicate that a weaker floc strength accelerates the floc breakage dynamics. Therefore, the floc strength used in the model must vary with season. We suggest using 3×10^{-11} N and 1×10^{-11} N as the floc strengths for simulating summer and winter seasons, respectively, in the southern North Sea.

3.5. Conclusion

We tested a biomineral flocculation model by using a single characteristic diameter (D50) to simulate the floc variations under different weather and seasonal conditions in the southern North Sea. We proposed a conception of tide-wave combined turbulence to investigate storm-influenced flocculation.

A 50% improvement in the model accuracy, compared with simulations that have only been forced by tidal velocity, demonstrates the importance of waves for SPM dynamics and transport during storm-dominated environments. Additionally, the results confirm

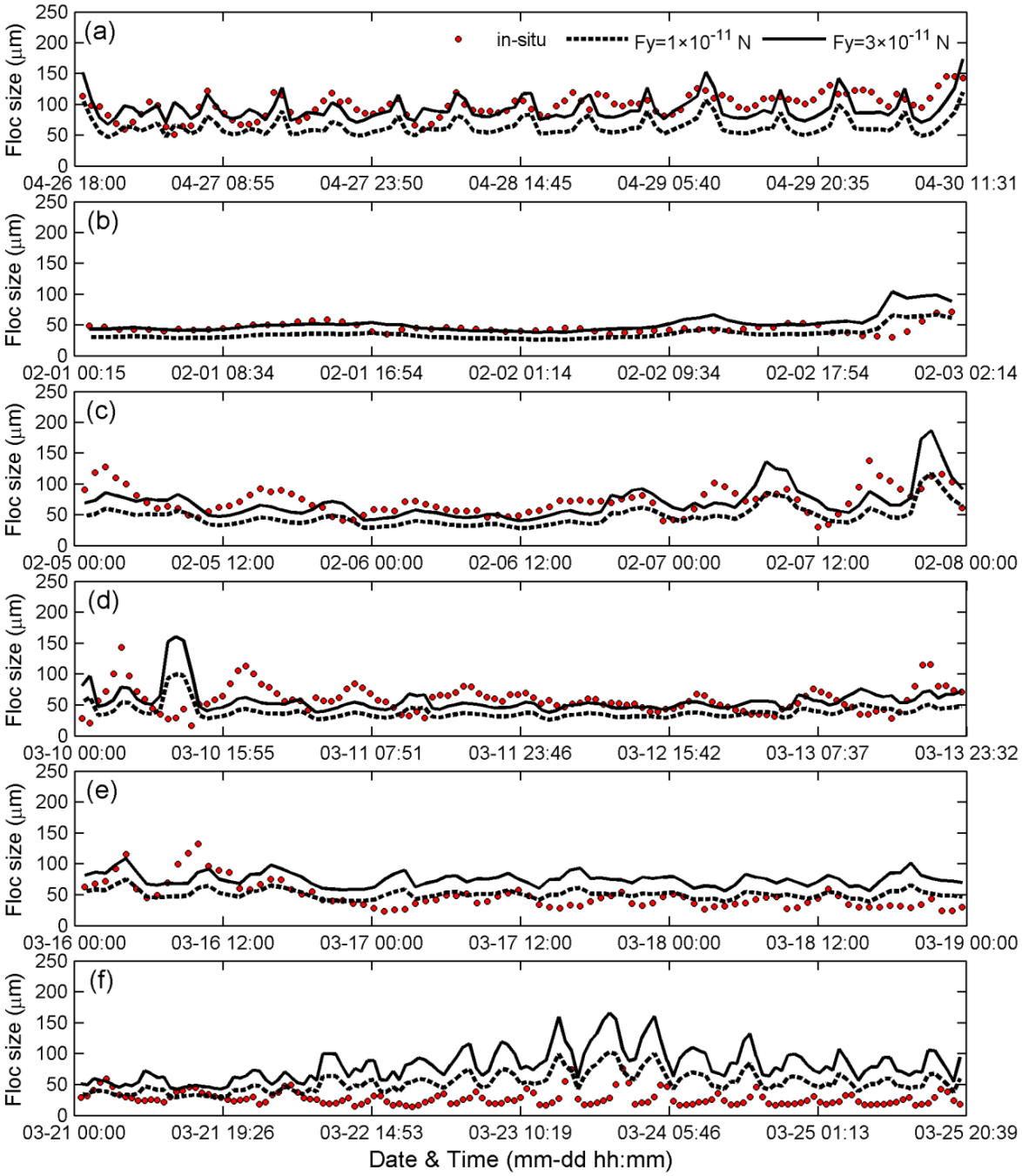

Figure 3.9: Floc size simulated with different values of floc strengths (Fy; circle: measured data, dash line: Fy = 1×10^{-11} N, solid line: Fy = 3×10^{-11} N) for (a) April 26 to 30 (calm days), (b) February 1 to 2 (SW storm), (c) February 5 to 7 (SW storm), (d) March 10 to 13 (NE storm), (e) March 16 to 19 (NE storm), and (f) March 21 to 25 (NE storm).

that floc strength has a seasonal influence on floc development. We observed a stronger floc-binding strength in the summer season (April–September), during which flocculation was influenced by abundant sticky organic substances, compared with the biomass-lacking (Figure 3.2) winter season (October–March). Therefore, applying different floc strengths is essential to successfully model seasonal variations in the southern North Sea; according to our study, the ideal floc strengths are 3×10^{-11} N during summer and 1×10^{-11} N during winter.

The present model assumed a unimodal size distribution and simulated single charac-

teristic particles. Future studies on flocculation using multimodal PSDs are warranted. Additionally, the constant values of the floc strength used in this model are insufficient to represent seasonal characteristics. Thus, accurate understanding of the correlations between floc strength properties and physical, chemical, and biological environments (e.g., hydrometeorological conditions, sunlight intensity, microorganisms, and Chl), and their seasonal effects on floc-binding ability, require further investigation.

4. Referenties

Alldredge AL, Passow U, Logan BE. 1993. The abundance and significance of a class of large, transparent organic particles in the ocean. Deep-Sea Research I 40, 1131–1140.

Arcadis. 2017. MER baggerstortlocatie Zeebrugge West. Voorbereiding en opmaak MER Baggerstortlocatie Zeebrugge West. Fase 1 - Verkennende fase locaties & exploitatie-scenario's, 9 juni, 87pp.

Baeye M, Fettweis M, Voulgaris G, Van Lancker V. 2011. Sediment mobility in response to tidal and wind-driven flows along the Belgian inner shelf, Southern North Sea. Ocean Dynamics 61, 611–622. doi:10.1007/s10236-010-0370-7

Berlamont J, Ockenden M, Toorman E, Winterwerp J. 1993. The characterisation of cohesive sediment properties. Coastal Engineering 21, 105–128.

Borges AV, Gypens N. 2010. Carbonate chemistry in the coastal zone responds more strongly to eutrophication than to ocean acidification. Limnology and Oceanography 55, 346–353. doi:10.4319/lo.2010.55.1.0346

Desmit X, Vanderborght JP, Regnier P, Wollast R. 2005. Control of phytoplankton production by physical forcing in a strongly tidal, well-mixed estuary. Biogeosciences 2, 205–218. doi:10.5194/bg-2–205-2005

Droppo IG. 2001. Rethinking what constitutes suspended sediment. Hydrological Processes 15, 1551–1564. doi:10.1002/hyp.228

Droppo IG, Nackaerts K, Walling DE, Williams N. 2005. Can flocs and water stable soil aggregates be differentiated within fluvial systems? Catena, 60, 1-18. doi:10.1016/j.catena.2004.11.002

Dyer KR. 1989. Sediment processes in estuaries: Future research requirements. Journal of Geophysical Research 94, 14327–14339.

Eisma D. 1986. Flocculation and de-flocculation of suspended matter in estuaries. Netherlands Journal of Sea Research 20, 183-199.

Engel A. 2000. The role of transparent exopolymer particles (TEP) in the increase in apparent particle stickiness during the decline of a diatom bloom. Journal of Plankton Research22, 485–497.

Fettweis M, Francken F, Van den Eynde D. 2005. MOMOactiviteitsrapport (1 april 2005 – 30 september 2005). BMM-rapport MOMO/2/MF/200512/NL/AR/2. 27pp.

Fettweis M, Francken F, Pison V, Van den Eynde D. 2006. Suspended particulate matter dynamics and aggregate sizes in a high turbidity area. Marine Geology 235, 63–74.

Fettweis M, Van den Eynde D, Francken F. Van Lancker V. 2009. MOMO activiteits-rapport 2 (januari 2009 – juli 2009). BMM-rapport MOMO/4/MF/200909/NL/AR/2, 33pp + app.

Fettweis M, Francken F, Van den Eynde D, Verwaest T, Janssens J, Van Lancker V. 2010. Storm influence on SPM concentrations in a coastal turbidity maximum area with high anthropogenic impact (Southern North Sea). Continental Shelf Research 30, 1417–1427. doi:10.1016/j.csr.2010.05.001

Fettweis M, Baeye M, Lee BJ, Chen P, Yu JCR. 2012. Hydro-meteorological influences and multimodal suspended particle size distributions in the Belgian nearshore area (Southern North Sea). Geo-Marine Letters 32, 123–137. doi:10.1007/s00367-011-0266-7

Fettweis M, Baeye M, Van der Zande D, Van den Eynde D, Lee BJ. 2014. Seasonality of floc strength in the Southern North Sea. Journal of Geophysical Research 119, 1911–1926. doi:10.1002/2013JC009750

Fettweis M, Baeye M, Francken F, Van den Eynde D. 2015. MOMO activiteitsrapport (1 januari – 30 juni 2015). BMM-rapport MOMO/7/MF/201508/NL/AR/3, 76pp + app.

Fettweis M, Baeye M, Cardoso C, Dujardin A, Lauwaerts B, Van den Eynde D, Van Hoestenberghe T, Vanlede J, Van Poucke L, Velez C, Martens C. 2016. The impact of disposal of fine grained sediments from maintenance dredging works on SPM concentration and fluid mud in and outside the harbor of Zeebrugge. Ocean Dynamics, 66, 1497-1516. doi:10.1007/s10236-016-0996-1

Green MO, Vincent CE, McCave IN, Dickson RR, Rees JM, Pearson ND. 1995. Storm sediment transport: Observations from the British North Sea Shelf. Continental Shelf Research 15, 889–912.

Howarth MJ, Dyer KR, Joint IR, Hydes DJ, Purdie DA, Edmunds H, Jones JE, Lowry RK, Moffat TJ, Pomroy AJ, Proctor R, Van Leussen W. 1993. Seasonal cycles and their spatial variability. Philosophical Transaction of the Royal Society A 343, 383–403.

Jago CF, Kennaway GM, Novarino G, Jones SE. 2007. Size and settling velocity of suspended flocs during a phaeocystis bloom in the tidally stirred Irish Sea, NW European Shelf. Marine Ecology Progress Series 345, 51–62. doi:10.3354/meps07006.

Kiorboe T, Andersen KP, Dam HG. 1990. Coagulation efficiency and aggregate formation in marine phytoplankton. Marine Biology 107, 235–245.

Kirby R. 2011. Minimising harbour siltation - findings of PIANC Working Group 43. Ocean Dynamics 61, 233–244.

Lacroix G, Ruddick K, Park Y, Gypens N, Lancelot C. 2007. Validation of the 3D biogeochemical model MIRO&CO with field nutrient and phytoplankton data and MERIS-derived surface chlorophyll a images. Journal of Marine Systems 64, 66-88. doi: 10.1016/j.jmarsys.2006.01.010.

Lancelot C, Billen G, Sournia A, Weisse T, Colijin F, Veldhuis MJW, Davies A, Wassman P. 1987. Phaeocystis blooms and nutrient enrichment in the continental coastal zones of the North Sea. Ambio, 16, 38–46.

Lauwaert B, Fettweis M, De Witte B, Devriese L, Van Hoei G, Timmermans S, Martens C. 2016. Synthesis report on the effects of dredged material disposal on the marine environment (licensing period 2012-2016). RBINS-ILVO-AMT-AMCS-FHR report BL/2016/09, 107pp.

Lee HL, Wiberg PL. 2002. Character, fate, and biological effects of contaminated, effluent-affected sediment on the Palos Verdes margin, southern California: An overview. Continental Shelf Research 22, 835–840.

Lee BJ, Toorman E, Molz FJ, Wang J. 2011. A two-class population balance equation yielding bimodal flocculation of marine or estuarine sediments. Water Research 45, 2131–2145. doi:10.1016/j.watres.2010.12.028

Lee BJ, Fettweis M, Toorman E, Molz FJ. 2012. Multimodality of a particle size distribution of cohesive suspended particulate matters in a Coastal Zone. Journal of Geophysical Research 117, C03014. doi:10.1029/2011JC007552

Li Y, Mehta AJ. 2000. Fluid mud in the wave-dominated environment revisited. Proceedings in Marine Science 3, 79–93.

Logan BE, Passow U, Alldredge AL, Grossartt H, Simon M. 1995. Rapid formation and sedimentation of large aggregates is predictable from coagulation rates (half-lives) of Transparent Exopolymer Particles (TEP). Deep Sea Research II 42, 203–214.

Maerz J, Wirtz K. 2009. Resolving Physically and Biologically Driven Suspended Particulate Matter Dynamics in a Tidal Basin with a Distribution-Based Model. Estuarine Coastal and Shelf Science 84, 128–138. doi:10.1016/j.ecss.2009.05.015

Maggi F. 2009. Biological flocculation of suspended particles in nutrient-rich aqueous ecosystems. Journal of Hydrology 376, 116–125. doi:10.1016/j.jhydrol.2009.07.040

Maggi F, Tang FHM. 2015. Analysis of the effect of organic matter content on the architecture and sinking of sediment aggregates. Marine Geology 363, 102-111. doi:10.1016/j.margeo.2015.01.017

Manning AJ, Bass SJ, Dyer KR. 2006. Floc properties in the turbidity maximum of a mesotidal estuary during neap and spring tidal conditions. Marine Geology 235, 193–211.

Matsuo T, Unno H. 1981. Forces acting on flocs and strength of flocs. Journal of Environmental Engineering 107, 527–545.

Mietta F, Chassagne C, Manning AJ, Winterwerp JC. 2009. Influence of shear rate, organic matter content, pH and salinity on mud flocculation. Ocean Dynamics 59, 751–763, doi:10.1007/s10236-009-0231-4.

Passow U, Shipe R, Murray A, Pak D, Brzezinski M, lldredge A. 2001. The origin of transparent exopolymer particles (TEP) and their role in the sedimentation of particulate matter. Continental Shelf Research 21, 327-346.

Pavoni JL, Tenney MW, Echelberger Jr WF. 1972. Bacterial exocellular polymers and biological flocculation. Journal (Water Poll. Control Federat.), 414-431.

Soulsby R. 1997. Dynamics of marine sands: A manual for practical applications. Thomas

Telford, London, 249pp.
Tan XL, Zhang GP, Hang YIN, Furukawa Y. 2012. Characterization of particle size and settling velocity of cohesive sediments affected by a neutral exopolymer. International Journal of Sediment Research 27, 473-485. doi:10.1016/S1001-6279(13)60006-2
Tang FHM, Maggi F. 2016. A mesocosm experiment of suspended particulate matter dynamics in nutrient- and biomass-affected waters. Water Research 89, 76-86. doi:10.1016/j.watres.2015.11.033.
Traykovski P, Wiberg PL, Geyer WR. 2007. Observations and modeling of wave-supported sediment gravity flows on the Po prodelta and comparison to prior observations from the Eel shelf. Continental Shelf Research 27, 375–399. doi:10.1016/j.csr.2005.07.008
Van den Eynde D, Fettweis M. 2006. Modelling of fine-grained sediment transport and dredged material on the Belgian Continental Shelf. Journal of Coastal Research SI39, 1564-1569.
Van den Eynde D, Fettweis M. 2015. Modellering van een alternatieve stortstrategie voor de onderhoudsbaggerwerken in de voorhaven van Zeebrugge. Momo Technisch rapport, MOMO/7/DVDE/201506/NL/TR/1, 16pp.
Van Kessel T, Kranenburg C. 1998. Wave-induced liquefaction and flow of subaqueous mud layers. Coastal Engineering 34, 109–127.
Van Leussen W. 1994. Estuarine macroflocs: Their role in fine grained sediment transport. Ph.D. thesis, University of Utrecht, 488pp.
Verney R, Lafite R, Brun-Cottan JC, Le Hir P. 2010. Behaviour of a floc population during a tidal cycle: Laboratory experiments and numerical modeling. Continental Shelf Research 31, S64–S83. doi:10.1016/j.csr.2010.02.005
Winterwerp JC. 1998. A simple model for turbulence induced flocculation of cohesive sediment. Journal of Hydraulic Research 36, 309–326.
Winterwerp JC. 2002. On the flocculation and settling velocity of estuarine mud. Continental Shelf Research 22, 1339–1360.
Wright LD, Friedrichs CT. 2006. Gravity-driven sediment transport on continental shelves: a status report. Continental Shelf Research 26, 2092-2107. doi:10.1016/j.csr.2006.07.008

COLOPHON

Dit rapport werd voorbereid door de BMM in augustus 2017
Zijn referentiecode is MOMO/8/MF/201708/NL/AR/1

De scheepstijd met de RV Belgica werd voorzien door BELSPO en KBIN-OD Natuur

Indien u vragen hebt of bijkomende copies van dit document wenst te verkrijgen, gelieve een e-mail te zenden naar mfettweis@naturalsciences.be, met vermelding van de referentie, of te schrijven naar:

Koninklijk Belgisch Instituut voor Natuurwetenschappen
OD Natuur – BMM
t.a.v. Michael Fettweis
Gulledelle 100
B–1200 Brussel
België
Tel: +32 2 773 2132

BEHEERSEENHEID VAN HET
MATHEMATISCH MODEL VAN DE NOORDZEE

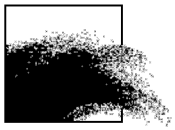

APPENDIX 1

Bijdrage Schelde-Ems workshop 16-17 februari, Antwerpen

Quantitative clay mineralogy as provenance indicator for the recent muds located at the marine limit of influence of the Scheldt estuary

Rieko Adriaens[1], Edwin Zeelmakers[1], Michael Fettweis[2], Elin Vanlierde[3], Joris Vanlede[3], Peter Stassen[1], Jan Elsen[1], Jan Środoń[4], Noël Vandenberghe[1]

[1]Department of Earth and Environmental Sciences, KU Leuven, Celestijnenlaan 200E, B-3001 Heverlee, Belgium
[2]Royal Belgian Institute of Natural Sciences, OD Natural Environment, Gulledelle 100, B-1200 Brussels, Belgium
[3] Department of Mobility and Public Works, Flanders Hydraulics Research, Berchemlei 115, 2140 Antwerp, Belgium
[4] Institute of Geological Sciences, Polish Academy of Sciences, Research Centre in Kraków, ul. Senacka 1, PL-31002 Kraków, Poland

In order to assess the present state of a marine sedimentary environment and to predict changes induced by natural variability, human activities or climate change, qualitative understanding and quantitative estimates of sediment fluxes and budgets are needed. Although sediment fluxes and budgets are a key element to assess the fine-grained sediment dynamics on a regional scale, data are often not available to qualitatively understand the fluxes on a time-scale longer than the duration of in-situ measurement campaigns. One of the difficulties lays in the fact that regional fine-grained sediment dynamics is the sum of all the local sources and sinks, such as rivers, coastal erosion and accretion, deposition in inter- or subtidal areas and erosion of the geological substratum that are often not well known and that reflects the recent geological history of the area. This is also the case for the fine-grained sediment transport, the coastal turbidity maximum and the cohesive sediment deposits in the French-Belgian-Dutch nearshore area and in the Scheldt estuary, where the provenance is still under debate, see Figure 1.

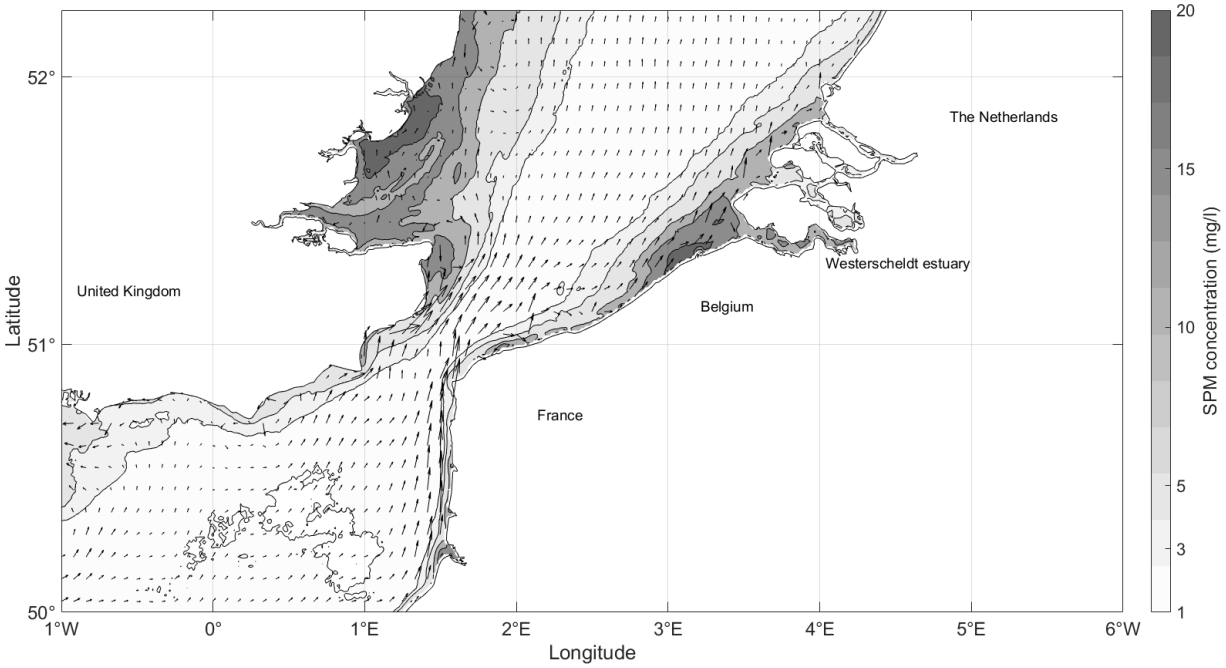

Figure 1: Geographical overview of the southern North Sea showing the turbidity maximum located in the Belgian nearshore area and at the mouth of the Westerscheldt estuary. The arrows indicate the residual water transport calculated by a numerical model. The map shows the surface SPM concentration averaged over 2003-2011 derived from MODIS satellite.

The existing hypotheses for the mud provenance are based on the understanding of the residual flow patterns and general sedimentological and regional geological considerations (e.g. Prandle et al. 1996; Velegrakis et al. 1999; Lafite et al. 2000; Fettweis et al. 2007). Few systematic compositional provenance investigations have been carried out so far in support. The aim of the current study is therefore to make a contribution towards qualitative and quantitative fine-grained sediment budgets

and dynamics in the southern North Sea by identifying how the provenance of the fine-grained bottom and suspended sediments is related to regional and local fine-grained sediment sources.

Method

As provenance indicator clay minerals have been used. Qualitative and semi-quantitative clay mineral analysis has already been successfully applied as tracers of fine-grained sediment pathways in marine, tidal and fluvial environments (Irion and Zöllmer 1999; Sandler and Herut 2000; Ramaswamy et al. 2007; Liu et al. 2008; Pache et al. 2008; Dou et al. 2010; Kessarkar et al. 2010; Liu et al. 2010; Howell et al. 2014; Li et al. 2014). The advantage of clay minerals is the obvious abundance of these minerals in the mud deposits and in the SPM and their stability or very minor changes if any during transport between provenance and deposition areas. This makes them more suited than other tracers such as geochemical properties of the mud who are considered a more tedious approach and more easily influenced by different environments during transport. Clay minerals can furthermore be considered as representative tracers as the transport of fine-grained sediment occurs either in flocs or as suspended particulate matter. Grain-size and mineralogical analyses hereof typically show that at least 85% of the mineralogical composition consists of clay minerals, silt- to fine sand-sized quartz and carbonates, demonstrating that clay minerals are not transported independently. Whereas quartz is obviously also detrital, a large percentage of the carbonate particles are without any doubt biogenic in origin. Clay minerals are therefore the best choice as provenance indicator. In the present study proven robust quantitative clay mineral analyses are used following the approach outlined by Drits et al. (1997), Sakharov et al. (1999), Środoń et al. (2001), Aplin et al. (2006), Środoń (2009) and Hubert et al. (2009, 2012).

An extensive sampling campaign was set up in different phases to characterize the clay mineral composition of the mud deposits off the Belgian nearshore (further referred to as BCS), the SPM in the English Channel and the southern North Sea, and its possible source areas. These comprise both present-day sources, which were sampled by collecting bottom mud and/or suspension water samples, outcrop material and older, geological sources, which were sampled from borehole core material. For each source area, the clay mineral composition <2µm, referred to as the clay fraction, was quantified and compared with the mud composition from the Belgian nearshore area (BCS).

Results

The clay mineral compositional field for each analyzed source area is shown in Figure 2 with reference to the BCS muds and SPM compositional field. This figure demonstrates that English Channel waters, outcropping Paleogene sea floor bottom and Rhine-Meuse river water and deposits have to be excluded as an important clay mineral source of the BCS muds. The BCS muds and SPM clay mineral composition is also found in the SPM occurring in the Dutch coastal waters. This demonstrates that the clay minerals in the Dutch coastal waters do not originate from the Rhine-Meuse River but have as major source the turbidity maximum overlying the BCS muds. The turbidity maximum in the Belgian nearshore area is thus formed by erosion of the BCS mud. Erosion of the medium consolidated BCS muds occurs during storms as observed near Zeebrugge (Fettweis et al. 2010).

The close relationship between the mud from the Scheldt estuary and the BCS mud raised the question whether the estuary effectively discharges the mud to the BCS where it is deposited or whether the inverse happens and BCS mud is imported into the estuary by tidal currents. This question was solved by looking at the clay mineral composition being discharged by the different upstream non-tidal tributaries towards the estuary. To investigate the mixture of clay minerals from the rivers entering the Scheldt estuary, the clay mineral composition of each tributary river was analyzed and combined with discharge and SPM concentration data in order to obtain annual mean clay mineral fluxes. As demonstrated in Figure 2, this combined fluvial discharge clay mineral composition plots very close to the Scheldt estuary and BCS mud composition. Furthermore, in the 1991-2009 time range little annual variation occurs, suggesting a stable flux of a constant clay mineral association into the estuary. Nevertheless, the estuary clay composition seems more variable

and contains elevated smectite contents which do not occur in any of the individual tributaries. In the clay mineral flux calculation estuarine erosion is not included however it will obviously further influence the sediment composition. As the estuary is eroding mainly smectite-rich Eocene deposits, similar in composition to the Paleogene sea floor bottom, this might explain the small discrepancy between the calculated clay mineral river fluxes and the estuarine clay mineral compositions. It can be concluded that the BCS mud composition can only be produced by Scheldt river system.

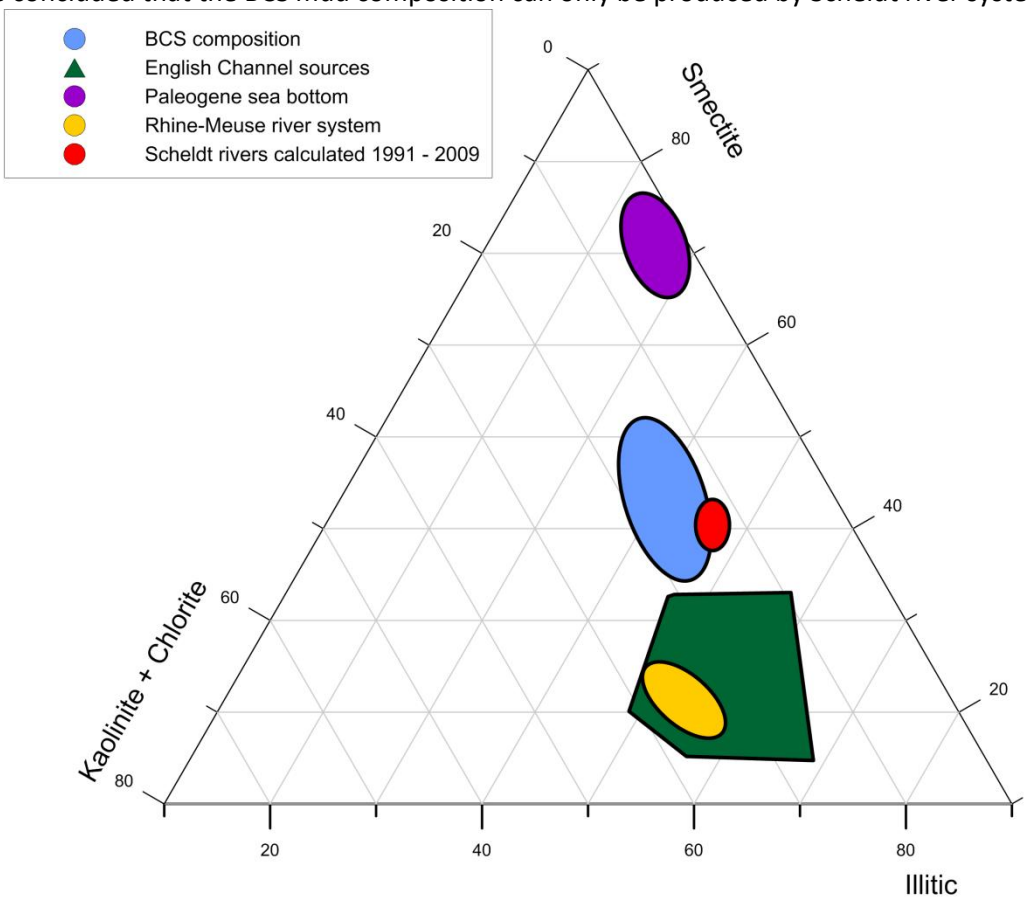

Figure 2: Triangular diagram of the quantitative clay composition <2µm of the different analyzed regional sources and comparison with the compositional domain of the Belgian nearshore area (BCS).

Still, the current tidal regime in the Scheldt estuary is marine-dominated with only negligible amounts of fluvial mud being discharged into the North Sea. Presently, marine SPM dominates the estuarine regime (Verlaan 2000). This apparent contradiction with the results of the clay mineral provenance analysis can only be satisfactorily solved if the short period of hydrodynamic and sediment flux measurements in the estuary since the start of the measurements (Baeteman et al. 1992; Houziaux et al. 2011) represents an unusual situation compared to the much longer period before with excess fluvial mud export from the estuary to the sea. The geological history suggest that the mud deposition with the BCS clay mineral composition has started since a few 100.000 years in contrast to the present hydrodynamics in the estuary and the coastal zone that exhibits a fine-grained sediment flux from out of the estuary towards inside. A consequence of this analysis is that the modern mud is derived from the erosion and resuspension of previously deposited mud. Resuspended muds contribute to a large part to the coastal turbidity maximum and represent a significant source of material in the estuary itself.

References

Aplin AC, Matenaar IF, McCarty DK, van der Pluijm BA. 2006. Influence of mechanical compaction and clay mineral diagenesis on the microfabric and pore scale properties of deep-water Gulf of Mexico mudstones. Clays & Clay Minerals, 54**,** 500-514.

Baeteman C, de Lannoy W, Paepe R, van Cauwenberghe C. 1992. Vulnerability of the Belgian coastal lowlands to future sea-level rise. In: Tooley M, Jelgersma S (Eds.), Impact of Sea-level Rise on European Coastal Lowlands, 56-71, Blackwell Publications.

Dou Y, Yang S, Liu Z, Clift PD, Yu H, Berne S, Shi X. 2010. Clay mineral evolution in the central Okinawa Trough since 28 ka: Implications for sediment provenance and paleoenvironmental change. Palaeogeography, Palaeoclimatology, Palaeoecology, 288, 108–117.

Drits VA, Lindgreen H, Sakharov BA, Salyn AL. 1997. Sequential structure transformation of illite-smectite- vermiculite during diagenesis of Upper Jurassic shales, North Sea. Clay Minerals, 33**,** 351-371.

Fettweis M, Nechad B, Van den Eynde D. 2007. An estimate of the suspended particulate matter (SPM) transport in the southern North Sea using SeaWiFS images, in-situ measurements and numerical model results. Continental Shelf Research, 27, 1568–1583.

Fettweis M, Francken F, Van den Eynde D, Verwaest T, Janssens J, Van Lancker V. 2010. Storm influence on SPM concentrations in a coastal turbidity maximum area (southern North Sea) with high anthropogenic impact. Continental Shelf Research 30, 1417-1427.

Howell AL, Bentley SJ, Xu K, Ferrell RE, Muhammad Z, Septama E. 2014. Fine sediment mineralogy as a tracer of latest Quaternary sediment delivery to a dynamic continental margin: Pandora Through, Gulf of Papua, Papua New Guinea. Marine Geology, 357, 108-122.

Houziaux J-S, Fettweis M, Francken F, van Lancker V. 2011. Historic (1900) seafloor composition in the Belgian-Dutch part of the North Sea: a reconstruction based on calibrated visual sediment descriptions. Continental Shelf Research, 31, 1043–1056.

Hubert F, Caner L, Meunier A, Lanson B. 2009. Advances in characterization of the soil clay mineralogy using X-ray diffraction: from decomposition to profile fitting. European Journal of Soil Science, 60, 1093-1105.

Hubert F, Caner L, Meunier A, Ferrage E. 2012. Unraveling complex <2µm clay mineralogy from soils using X-ray diffraction profile modeling on particle-size sub-fractions: Implications for soil pedogenesis and reactivity. American Mineralogist, 97, 384-398.

Irion G, Zöllmer V. 1999. Clay mineral associations in fine-grained surface sediments of the North Sea. Journal of Sea Research, 41, 119-12.

Kessarkar PM, Rao VP, Ahmad SM, Badu BA. 2003. Clay minerals and Sr–Nd isotopes of the sediments along the western margin of India and their implication for sediment provenance. Marine Geology, 202, 55–69.

Lafite R, Shimwell S, Grochowski N, Dupont J-P, Nash L, Salomon J-C, Cabioch L, Collins M, Gao S. 2000. Suspended particulate matter fluxes through the Strait of Dover, English Channel: observations and modelling. Oceanologica Acta, 23, 687–700.

Li J, Hu B, Wei H, Zhao J, Zou L, Bai F, Dou Y, Wang L, Fang X. 2014. Provenance variations in the Holocene deposits from the southern Yellow Sea: Clay mineralogy evidence. Continental Shelf Research, 90, 41-51.

Liu Z, Tuo S, Colin C, Liu JT, Huang C-Y, Selvaraj K, Chen C-TA, Zhao Y, Siringan FP, Boulay S, Chen Z, 2008. Detrital fine-grained sediment contribution from Taiwan to the northern South China Sea and its relation to regional ocean circulation. Marine Geology, 255, 149–155.

Liu Z, Colin C, Li X, Zha Y, Tuo S, Chen Z, Siringan FP, Liu JT, Huang C-Y, You C-F, Huang K-F. 2010. Clay mineral distribution in surface sediments of the northeastern South China Sea and surrounding fluvial drainage basins: Source and transport, Marine Geology, 277, 48-60.

Pache T, Brockamp O, Clauer N. 2008. Varied pathways of river-borne clay minerals in a near-shore marine region: A case study of sediments from the Elbe- and Weser rivers, and the SE North Sea. Estuarine Coastal and Shelf Science, 78, 563-575.

Prandle D, Ballard G, Flatt D, Harrison AJ, Jones SE, Knight PJ, Loch SG, McManus JP, Player R, Tappin A. 1996. Combining modelling and monitoring to determine fluxes of water, dissolved and particulate metals through the Dover Strait. Continental Shelf Research, 16, 237–257.

Ramaswamy V, Nagender NB, Vethamony P, Illangovan D. 2007. Source and dispersal of suspended sediment in macro-tidal Gulf of Kachchh. Marine Pollution Bulletin, 54, 708–719.

Sakharov BA, Lindgreen H, Salyn AL, Drits VA. 1999. Determination of illite-smectite structures using multispecimen X-ray diffraction profile fitting. Clays and Clay Minerals, 47, 555-566.

Sandler A, Herut B. 2000. Composition of clays along the continental shelf off Israel: contribution of the Nile versus local sources. Marine Geology, 167, 339-354.

Środoń J, Drits VA, McCarty DK, Hsieh JCC, Eberl DD. 2001. Quantitative XRD analysis of clay-rich rocks from random preparations. Clays & Clay Minerals, 49, 514-528.

Środoń J, McCarty DK. 2009. Surface area and layer charge of smectite from CEC and EGME/H_2O-retention measurements. Clays and Clay Minerals, 56, 155–174.

Velegrakis AF, Michel D, Collins MB, Lafite R, Oikonomou EK, Dupont JP, Huault MF, Lecouturier M, Salomon JC, Bishop C. 1999. Sources, sinks and resuspension of suspended particulate matter in the eastern English Channel. Continental Shelf Research 19, 1933–1957.

Verlaan PAJ. 2000. Marine vs Fluvial Bottom Mud in the Scheldt Estuary. Estuarine, Coastal and Shelf Science (2000) 50, 627–638.

APPENDIX 2

Rapport over 'Measuring, using ADV and ADP sensors, and modelling bottom shear stresses at the MOW1 site (Belgian continental shelf)

ROYAL BELGIAN INSTITUTE FOR NATURAL SCIENCES
OPERATIONAL DIRECTORATE NATURAL ENVIRONMENT

Section Ecosystem Data Analysis and Modelling
Suspended Matter and Sea Bottom Modelling and Monitoring Group

Measuring, using ADV and ADP sensors, and modelling bottom shear stresses at the MOW1 site (Belgian continental shelf)

Dries Van den Eynde

MOMO-INDI67/1/DVDE/201608/EN/TR01

Prepared for MOMO and INDI67projects

RBINS-OD Nature
100 Gulledelle
B–1200 Brussels
Belgium

Table of Contents

I. Introduction

The bottom shear stress is an important factor for the calculation of sediment transport. The bottom shear stress determines the erosion and resuspension of the material. Furthermore, different total load and bottom load formulae take into account the bottom shear stress (or a related parameter). The calculation of the bottom shear stress, under the combined influence of currents and waves, is however not a trivial task. Different methods and techniques are available in literature, sometimes using many parameters, which are not well known. The methods can vary from very simple models to very complex and time-consuming models. Also for the bottom roughness length, one of the main parameters determining the bottom shear stress, different models are available in literature. All these different models can give results that can vary over a large range.

Furthermore the measuring of the bottom shear stress is very complex and reliable bottom shear stress measurements, that could be used to validate the model predictions, are at the moment not available. Different methods are available to "measure" the bottom shear stress. In Francken and Van den Eynde (2010) a method was described, to calculate the bottom shear stress from the measurements from a high frequency point velocity meter (Acoustic Doppler Velocimeter ADV), where the bottom shear stress can be calculated, using the decay in the turbulent velocity spectrum in the high frequency range, the. Also the turbulent kinetic energy or the Reynolds stresses, which can be calculated from the high frequency velocity variations, can be used to calculate the bottom shear stress. Finally, the bottom shear stress can be calculated from the logarithmic profile of the water currents in the lower water column. These current profiles can be measured using an Acoustic Doppler Profiler (ADP).

In Van den Eynde (2015) measurements from 70 deployments with ADP and ADV sensors installed on bottom landers between 2005 and 2013 were analysed. The results of different numerical models for bottom shear stress and bottom roughness lengths (as a function of bottom ripples) were presented and their results were validated, using the measured bottom shear stresses. These first results showed that the bottom shear stress calculated using different methods do not correlate very well with each other and it is not straightforward to obtain reliable measurements of the bottom shear stress. The turbulent kinetic energy method seems to give the most reliable estimates of the bottom shear stress. Two deployments, one offshore and one nearshore, were analysed in more detail to validate the results. The results showed that the bottom shear stress could be modelled with a sufficient accuracy but that the value of the bottom roughness length could vary over different order of magnitudes. Overall, reasonable results for all deployments were obtained with the Soulsby model and with a bottom roughness length of 0.01 m.

In the present report, measurements of the bottom shear stress from one deployment at the MOW1 site are analysed in more detail. A new method to derive the bottom shear stress from high frequency measurements of current velocity, i.e. the eddy correlation method, was used additionally. Some more pre-processing of the data was included to try to increase the quality of the measurements.

The measurements and the numerical models are discussed in the first two

sections. Hereafter the analysis of the bottom stress measurements is presented. In the next section, the validation of the numerical models is discussed. Finally some overall conclusions from the comparison of the model results with the measurements and plans for further work are given at the end.

2. Description of the measurements

To measure the bottom shear stress, measurements were executed with bottom landers that are deployed at the bottom of the sea (see **Error! Reference source not found.**). The frame is, amongst others, equipped with a SonTek ADV Ocean point velocity meter, at 36 cm above the bottom (measuring at 18 cm above the bottom) and a downward looking SonTek 3 MHz ADP current profiler, at 228 cm above the bottom. Measurements of the ADP could be used to calculate the bottom stress from the current profile, while the measurements of the ADV could be used to calculate the bottom stress, using the inertial dissipation method, the eddy correlation method or the turbulent kinetic energy method.

The deployment 071 was executed at station MOW1 (51.360668 °N, 3.114650 °E), near the harbour of Zeebrugge in a water depth of about 10 m. The deployment was executed from 21/08/2013 till 23/09/2013. The position of the stations is presented in Figure 2.

The period comprises more than two spring-neap tidal cycles, with spring-times around days 4, 17 and 31 (Figure 3Figure 19). The significant wave height is below 1 m during the first 20 days of the deployment (Figure 4Figure 22). From day 20 till day 30, higher waves occur, with a peak in significant wave height above 3.0 m at day 21.

Figure 1: Tripod bottom lander.

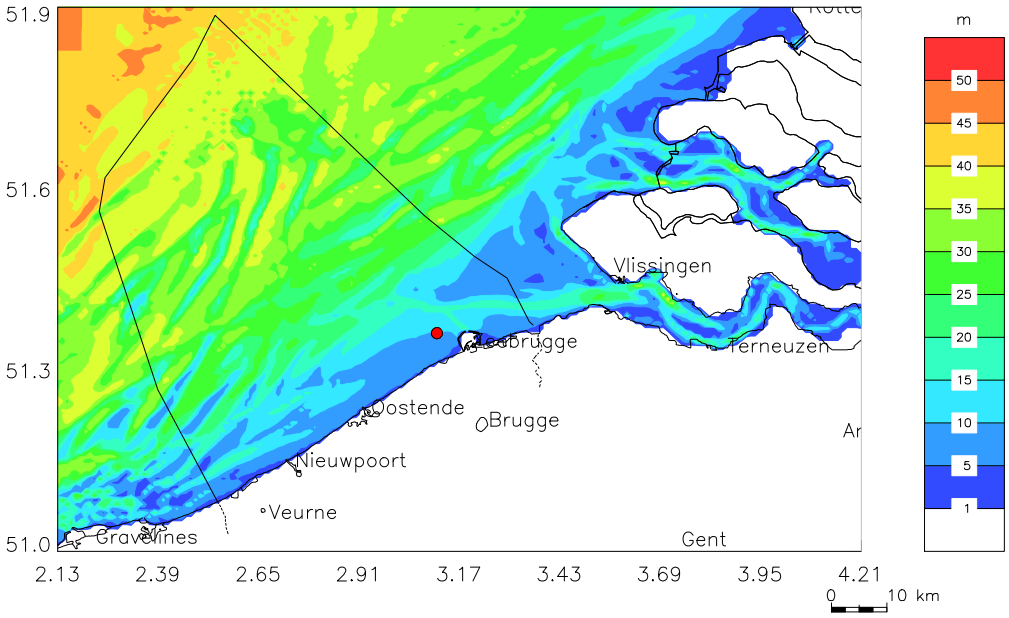

Figure 2: Position of the measuring station. Bathymetry of the OPTOS-BCZ model.

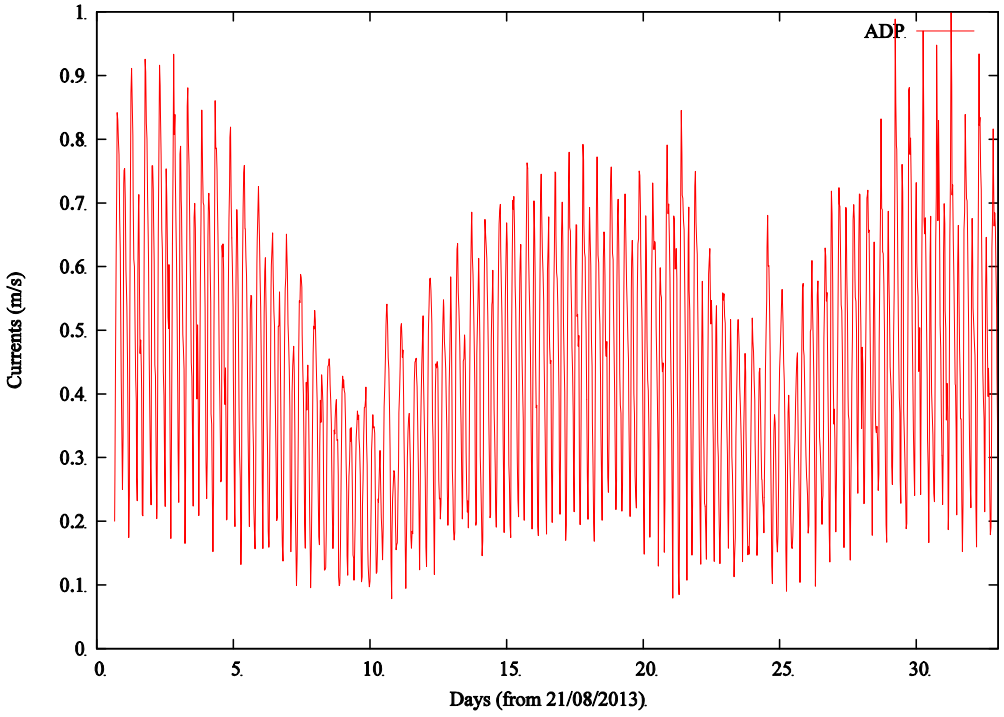

Figure 3: Currents, measured with the ADP during deployment 071.

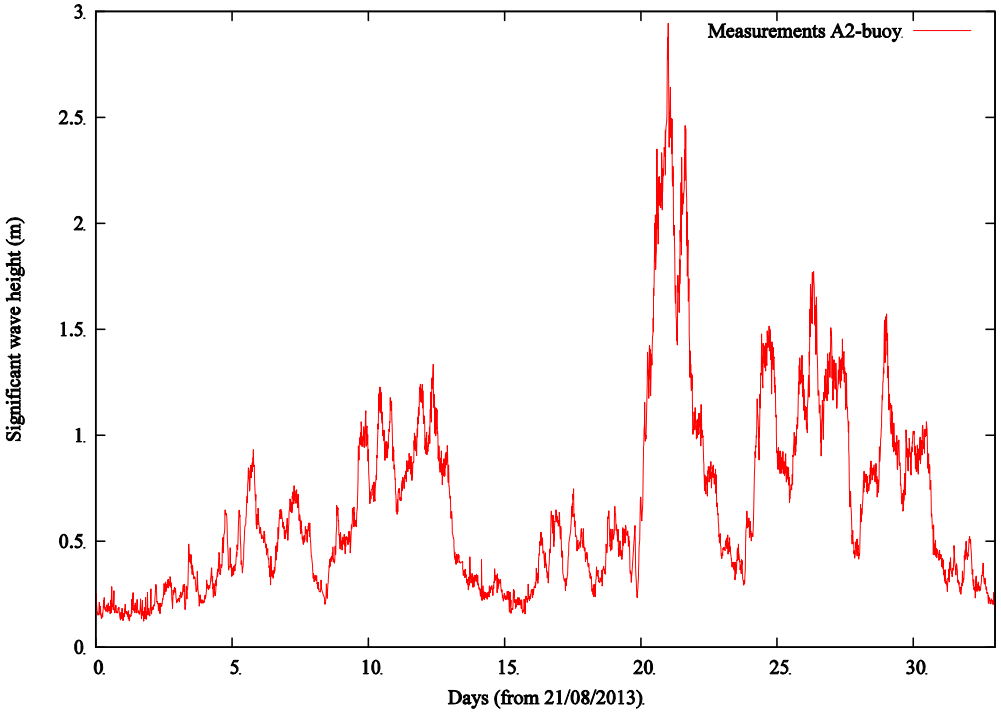

Figure 4: Waves measured at the A2-buoy (data from Vlaamse Gemeenschap, Meetnet Vlaamse Banken).

3. Numerical models

3.1. Introduction

To calculate the bottom shear stress under the influence of the currents and the waves, numerical models are used. A three-dimensional hydrodynamic model is used for the calculation of the water elevations and the currents. A third generation wave model is used to calculate the waves. Both models will be discussed shortly.

Furthermore, different methods and models are available in literature to calculate the bottom shear stress from the currents and waves. The different models that are used in this study, together with the models to calculate the bottom roughness under the influence of bottom ripples and bed load, are discussed in the next section.

3.2. Hydrodynamic model OPTOS-BCZ

The three-dimensional hydrodynamic modelling software COHERENS calculates the currents and the water elevation under the influence of the tides and the atmospheric conditions. The model was developed between 1990 and 1998 in the framework of the EU-MAST projects PROFILE, NOMADS and COHERENS. The hydrodynamic model solves the momentum equations and the continuity equation with, if necessary, equations for the sea water temperature and salinity. The momentum and continuity equations are solved using the 'mode splitting' technique. COHERENS disposes over different turbulent closures. A good description of the turbulence is necessary for a good simulation of the vertical profile of the currents. A new version of the COHERENS software has been developed recently (Luyten *et al.*, 2014), mainly allowing the model to use parallel computing, while adding also some new features, such as improving the numerical scheme and adding a wetting-drying mechanism.

The model OPTOS-BCZ is based on this COHERENS code and is implemented on the Belgian Continental Shelf with a grid with a resolution of 42.8″ in longitude (816 to 834 m) and 25″ in latitude (771 m). This model has a 10 σ-layers distributed over the total water depth. Along the open boundaries, the OPTOS-BCZ model is coupled with two regional models. The OPTOS-CSM model comprises the entire Northwest European Continental Shelf and calculates the boundary conditions of the North Sea model OPTOS-NOS. The latter model calculates the boundary conditions of the OPTOS-BCZ model. The OPTOS-CSM model calculates the depth-averaged currents and is driven by the water elevations at the open sea boundaries, using four semi-diurnal and four diurnal constituents. The bathymetry of OPTOS-BCZ model is shown in Figure 2.

The OPTOS-BCZ model was validated, amongst others, in the framework of the Marebasse project (Van Lancker *et al.*, 2004) and the BOREAS project (Dujardin *et al.*, 2010; Mathys *et al.*, 2011).

3.3. Wave model WAM

The WAM model is a third generation wave model, developed by the WAMDI Group (1988) and described by Günther *et al.* (1992). The WAM model is used both for

research and for operational wave forecasting. It includes 'state-of-the-art' formulations for the description of the physical processes involved in the wave evolution. In comparison with the 2nd generation model, the wave spectrum has no restrictions and the wind sea and the swell spectrum are not treated separately.

At the Operational Directorate Natural Environment, the model is running on three coupled model grids. A coarse model grid comprises the entire North Sea, the Fine model models the central North Sea and the Local model calculates the waves in the Southern Bight. The local model has a grid resolution of 0.033° in latitude and 0.022° in longitude. The bathymetry of this local model grid is presented in Figure 5.

The WAM model was recently validated by Van den Eynde (2013).

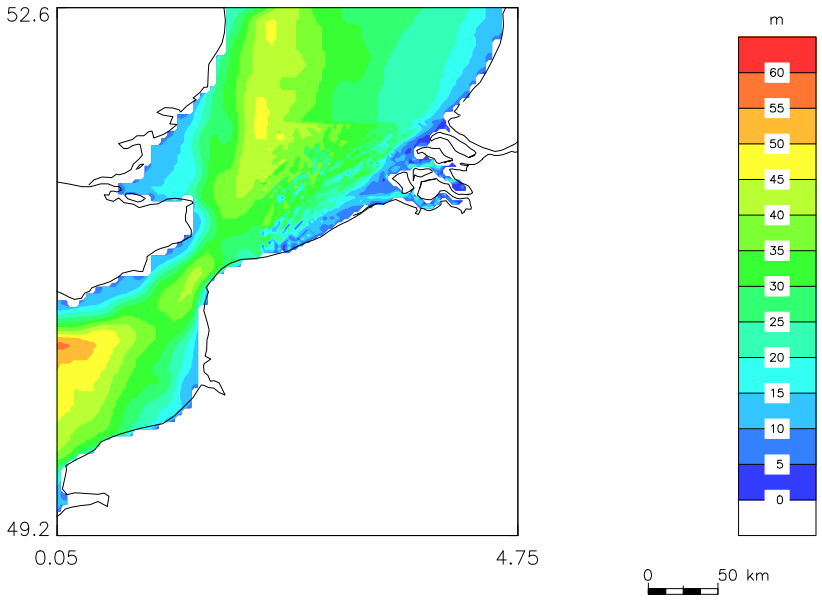

Figure 5: Model grids of the local grid WAM model.

3.4. *Calculation of the bottom shear stress*

3.4.1. Introduction

The calculation of the bottom shear stress is the topic of much research. The bottom shear stresses under the influence of currents alone and under the influence of waves alone over a flat bottom are quite well known. However, the calculation of the bottom shear stress under the combined influence of currents and waves, over a rippled sea bed is complex. First of all, the calculation of the bottom shear stress under the influence of currents and waves is not the simple vector addition of the bottom stress vectors for the currents and the waves alone. Non-linear interactions increase the mean bottom shear stress.

Furthermore, the bottom roughness length, which is an important factor for the calculation of the bottom shear stress, is influenced by different factors. At the bottom itself, the roughness is a function of the grain size. This bottom shear stress, felt by the sediments is called the skin friction. However, at a distance more

than a tenth of the length of the bottom ripples, the bottom roughness is also influenced by the bed load and by the height and the length of the bottom ripples. Further away from the bottom, a new logarithmic profile is followed with an apparently increased bottom roughness. The ratio between the skin bottom roughness and the total bottom roughness varies between 1.5 and 20.

In the next sections the bottom shear stress under the influence of the currents, under the influence of the waves and under the influence of the combined effect of currents and waves are discussed separately. Furthermore, also the calculation of the bottom roughness length is discussed in a following section.

3.4.2. Bottom shear stress under the influence of currents

The bottom shear stress under the influence of currents can be written as:

$$\tau_c = \rho C_D \bar{u}^2 = \rho \left(\frac{\kappa}{ln \frac{h}{e z_0}} \right)^2 \bar{u}^2 = \rho u_*^2 \qquad (1)$$

with

τ_c	bottom shear stress under the influence of currents
ρ	water density
C_D	drag coefficient
$\bar{u}$	depth-averaged current
κ	Von Karman constant=0.4
h	water depth
e	2.7182
z_0	bottom roughness length
u_*	shear velocity

As stated above, for the bottom roughness length, a difference has to be made between the skin bottom roughness felt by the grains itself at the bottom, and the total bottom roughness that is felt by the currents and that is also influenced by the bottom load and by the bottom ripples.

3.4.3. Bottom shear stress under the influence of waves

The bottom shear stress under the influence of waves is calculated using the (maximum) orbital velocity at the bottom. Using linear wave theory, the maximal orbital velocity of a monochromatic wave can be calculated as:

$$u_w = \frac{\pi h_s}{T \sinh(kh)} \qquad (2)$$

with

h_s	significant wave height
T	wave period
k	wave number

When calculating the wave orbital velocity of a wave spectrum, most of the time the significant wave height and the mean water period are taken as characteristics, although some other recommendations can be found in literature. The wave orbital

excursion A can be calculated as:

$$A = \frac{u_w T}{2\pi} \tag{3}$$

The (maximum) bottom shear stress under the influence of waves is then calculated as:

$$\tau_w = \frac{1}{2}\rho f_w u_w^{\ 2} \tag{4}$$

with τ_w bottom shear stress under the influence of waves
f_w wave factor

Also for the wave factor, different theories or models are available, however, with relative small differences.

3.4.4. Bottom shear stress under the influence of currents and waves

For the calculation of the bottom shear stress under the influence of currents and waves, a distinction must be made between the mean bottom stress, averaged over a wave cycle and the maximum bottom stress, during a wave cycle. First of all, the mean bottom stress over a wave cycle is augmented by non-linear interactions between the currents and the waves. The maximum bottom stress is the maximum bottom stress during a wave cycle and therefore is not a simple addition of the bottom stress under the influence of the currents and the waves.

Many different models can be found in literature, varying from simple models to very complex iterative models, resolving the stresses in the wave boundary layer and during a complete wave cycle. These very complex models are however very time consuming and not really useful to be used in sediment transport models. In Van den Eynde and Ozer (1993), different simple models were compared with each other and with the results of more complex models, as they were presented in Dyer and Soulsby (1988). The Bijker (1966) model was selected as a good model, giving realistic model results. This model however does not give realistic results for the bottom shear stress under the influence of waves with very small currents. Additionally, no formulation was given for the mean bottom shear stress over a wave cycle. Therefore, this model is not used in this study.

Recently, more realistic and simple models for the combined bottom shear stress were proposed in literature. Therefore, three new formulations were implemented and tested.

First of all, the Soulsby (1995) formulae were implemented which were the results of a two-coefficient optimisation of a simple model to 131 data points, from more complex theoretical models.

More recently, Soulsby and Clarke (2005) developed a new model, assuming an eddy viscosity varying over the water column, but constant in time. The eddy viscosity varies linearly above the bottom in the thin wave boundary layer and has a parabolic function outside the wave boundary layer. Remark that the eddy viscosity is much higher in the thin wave boundary layer than outside. Furthermore, the eddy viscosity in the wave boundary layer is only a function of

waves and currents, so that no iterative calculations are needed.

In the wave boundary layer, the shear stress is constant, outside the wave boundary layer, the shear stress varies linearly, to zero at the water surface. A current profile can be calculated by integration of the current profile over the water depth, giving a quadratic equation that can be used to solve the bottom shear stress. The model of Soulsby and Clarke (2005) gives both a formulation for the maximal bottom shear stress during a wave cycle, and the mean bottom shear stress, averaged over a wave cycle. Furthermore, the theory was developed, both for flow over rough and over smooth bottom.

Finally, Malarkey and Davies (2012) developed the theory of Soulsby and Clarke further to include additional non-linearity in the model, which is present in the more complex theoretical models, but is not found in the Soulsby-Clarke model.

More information and some comparison of the results of the different models can be found in Van den Eynde (2015).

3.4.5. Calculation of the bottom roughness

As indicated above, the bottom shear stress under the influence of currents and waves is a function of the bottom roughness length z_0 (for turbulent flow with a rough bottom). A division has to be made between the bottom roughness length at the bottom itself, the skin bottom roughness, caused by the bottom material itself, and the total roughness, felt by the currents and the waves, which are also influenced by the bottom load and the bottom ripples. The skin and the total bottom roughness can be specified by the user itself, or can be calculated by a model. The bottom roughness length, the height above the bottom where the logarithmic current profiles becomes zero, is normally written as a function of the Nikuradse bottom roughness k_s, of the viscosity of the water ν and the friction velocity:

$$z_0 = \frac{k_s}{30} + \frac{\nu}{9u_*} \tag{5}$$

For hydrodynamic rough flows (as is the case for flows over a sandy bed), the second part of the bottom roughness length can be neglected.

The skin bottom roughness is mostly written as a function of the grain-size distribution. A much used formulation is:

$$k_{ss} = 2.5d_{50} \tag{6}$$

with d_{50} the grain size for which 50% is smaller.

Values for the total bottom roughness can be found in tables. Typical values, found in literature, are k_s=0.2 mm for a mud bottom or k_s=6 mm for a rippled sand bottom. Wang et al. (2000) uses a bottom roughness z_0 of 0.1 cm, thus a bottom roughness k_s of 0.03 m. Drake *et al.* (1992) measured a bottom roughness z_0 over a rippled bed in the order of 1-2 cm.

For the roughness as a function of the bottom load, a division is made between current-domination and wave-domination. For current-domination, the

formula, proposed by Wilson (in Soulsby, 1997) is used. For wave-domination, five different possibilities were implemented, which are: 1) the Grant and Madsen (1982) model; 2) the Soulsby model; 3) the Grant and Madsen (1982) model, assuming wave-domination; 4) the Nielsen model and 5) the Raudkivi formulation (all in Soulsby, 1997). For the exact formulations, the reader is referred to Soulsby (1997).

Finally, the bottom roughness length is a function of the bottom ripples. Normally the bottom roughness, due to bottom ripples is written as:

$$k_{sv} = 27.7\frac{\eta^2}{\lambda} \qquad (7)$$

with η the ripple height
λ the ripple length

The ripple geometry itself can be calculated by the model again. Also here, a distinction is made between current-dominated ripples and wave-dominated ripples. Two models to calculate the ripple geometry were implemented. The first model uses the ripple geometry, proposed by Soulsby (1997) for the current-dominated ripples and the ripple geometry, proposed by Grant and Madsen (1982) for the wave-dominated ripples. More recently, a new ripple predictor was proposed by Soulsby and Whitehouse (2005). The model was validated against many laboratory and field experiment results and has the advantage that the time evolution of the ripples can be accounted for. Furthermore, for the current-dominated ripples, sheet flow and ripples that are washed out under larger currents are taken into account.

Again more information and some comparison of the results of the different models can be found in Van den Eynde (2015).

4. Analysis of the measurements

4.1. Bottom stress from ADP data

The ADP measured over 12 bins, with a bin size of 0.15 m. The highest bin was at 1.90 m above the bottom (mab), the lowest bin at 0.25 mab. The bottom shear stress can be calculated from the assumed logarithmic profile of the current near the bottom:

$$u = \frac{u_*}{\kappa} \ln \frac{z}{z_0} \tag{8}$$

with u the horizontal current velocity at z m above the bottom, κ the von Kármán constant, equal to 0.4, u_* the shear velocity and z_0 the bottom roughness length. This relation should be valid in the lowest 20% of the water column, below an outer turbulent region (Wilcock, 1996).

The shear velocity is related to the bottom shear stress, using the relation:

$$\tau = \rho u_*^2 \tag{9}$$

When the equation is rewritten as:

$$u = \frac{u_*}{\kappa} \ln z - \frac{u_*}{\kappa} \ln z_0 \tag{10}$$

the measured profile can be fitted to this logarithmic profile, using a least squares method (Wilkinson, 1984).

In Figure 6, current profiles, averaged over all current profiles in a certain direction, are shown. It can be seen that the current profiles in East and East-East-north (EEN) direction are showing a logarithmic profile neat the bottom, but are disturbed higher in the water column. This is probably due to the acoustic transponder that was installed on the tripod. This is also visible to a lesser extent in the profiles in East-north-north, in North, in South-East-East and South-South-East directions. Furthermore, it can be observed that the lowest current (at 0.25 mab) is often a little bit higher than the currents in the second lowest bin, see e.g. the profile in the West and the West-West-South directions. This lowest bin is possible disturbed by the bottom and/or by high concentrations of sediments near the bottom. Finally, one has to observe that during most of the profiles, not disturbed by the transponder, are more or less constant and don't show a clear logarithmic profile. Remark however, that it is expected that the actual profiles can differ significantly from the averaged profiles (Gross et al., 1992).

Taking into account the disturbance of the current profile in the region above 0.8 m, and the disturbance of the lowest current measurements, the bottom shear stress is calculated for the current profile over the region 0.30 mab to 0.90 mab, taking into account 4 current measurements at 0.40 mab, 0.55 mab, 0.70 mab and 0.85 mab. Drake et al. (1992) used the logarithmic profile to calculate the bottom shear stress, using measurements at three levels above the bottom. The only used the profiles (4 % of the profiles) with a correlation coefficient (see Appendix 1 for

the definition of the statistical parameters, used in this report) higher than 0.997, since for lower correlation coefficients, the errors on the bottom stress estimates becomes too high. If only data with a coefficient of determination R^2 higher than 0.99 would be used, only 59 data points would be used. Therefore, this criterium is lowered for this study, so that all bottom stresses are used, with a R^2 higher than 0.95. In this case, 1478 profiles (6 %) can be used, to calculate the bottom shear stress. Remark that, due to the disturbance of the current profiles, the distribution of the good profiles over the different directions is not uniform (see Figure 7). For the current going to East, almost 10 % of the data are used to calculate the bottom shear stress. For currents going to the North, West or South, only about 2 % of the data can be used. Remark that these values do not change significantly, when only the first 20 days, with moderate waves, are taken into account.

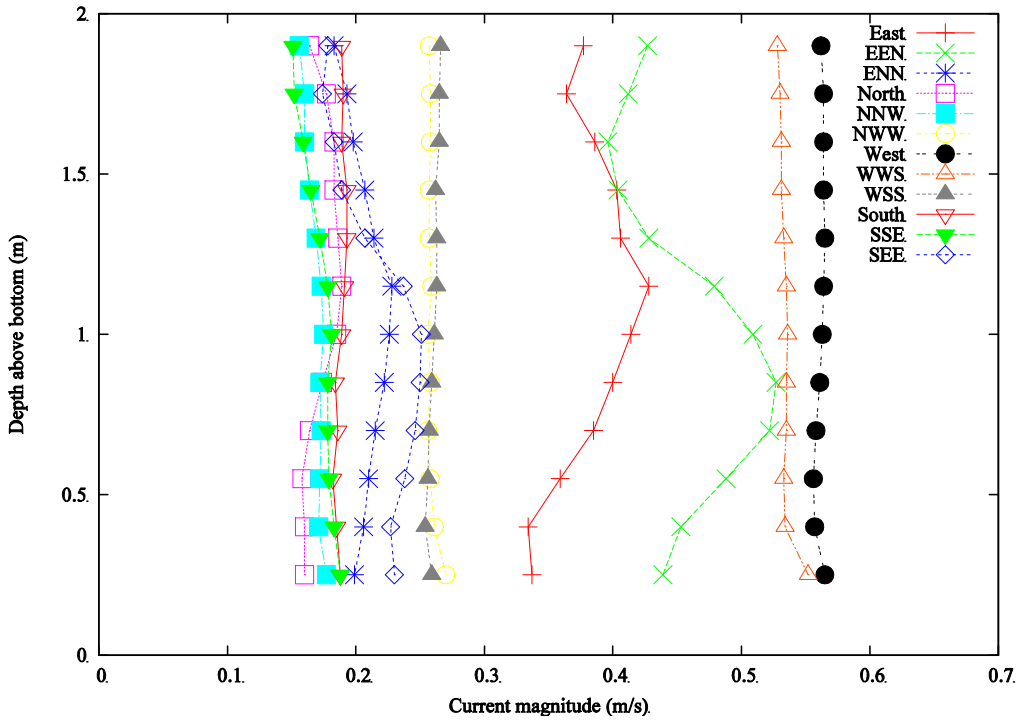

Figure 6: Current profile above the bottom, averaged over the entire deployment 071, for the different current directions.

The calculated bottom shear stresses are shown in Figure 8. Remark that the data from the altimeter on the ADV is used to follow the evolution of the bottom below the tripode. The data from the altimeter is used to correct the level above the bottom where the currents measurements were performed. The correction of the altimeter data is shown in Figure 9.

The bottom shear stress clearly shows a tidal and a spring-neap tidal cycle. Data after day 26 start to get much higher and could not be reliable. Overall, the calculated bottom shear stresses seem high. Remark that when the current nearest the bottom (at 0.15 mab) is taken into account for calculating the bottom shear stresses, the calculated bottom shear stress is much lower. The correlation coefficient however decreases and a minimum correlation coefficient of 90% must

be used (instead of a minimum correlation coefficient of 95%) to obtain sufficient results. The fact that the bottom stress calculation from the current profile gives large estimates could be due to effects of stable stratification, associated with suspended sediments (Kim *et al.*, 2000; Fugate and Chant, 2005).

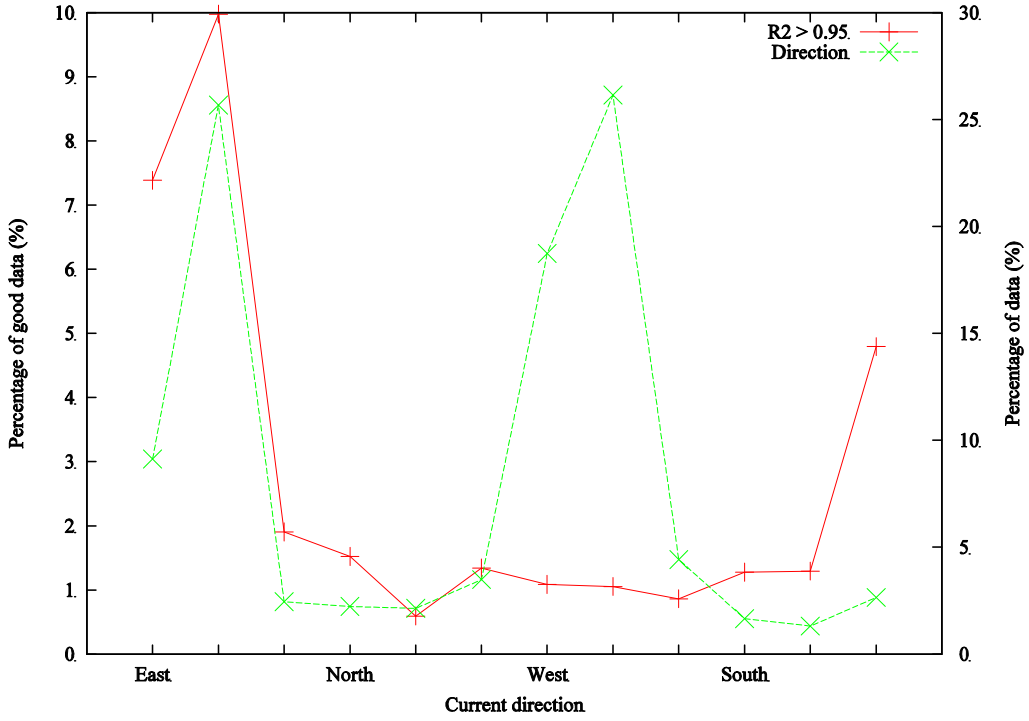

Figure 7: Percentage of good data, as a function of the current direction (red) and the distribution of the current direction of the full deployment.

4.2. *Bottom stress from ADV data*

4.2.1. Preprocessing of the data

The ADV data contain of burst of 7500 samples with a sampling frequency of 25 Hz. The burst interval is 15 minutes. The high frequency data contain, the three dimensional currents, measured at 18 cm above the bottom (when no bottom evolution is present). Also the "correlation" between the three beams of the ADV is recorded. This correlation factor is a measure for the quality of the data, which can be disturbed, e.g. by bubbles or suspended sediments (Elgar et al., 2005). According to the manual of the instrument, the data are suspicious when the correlation falls below 70 %.

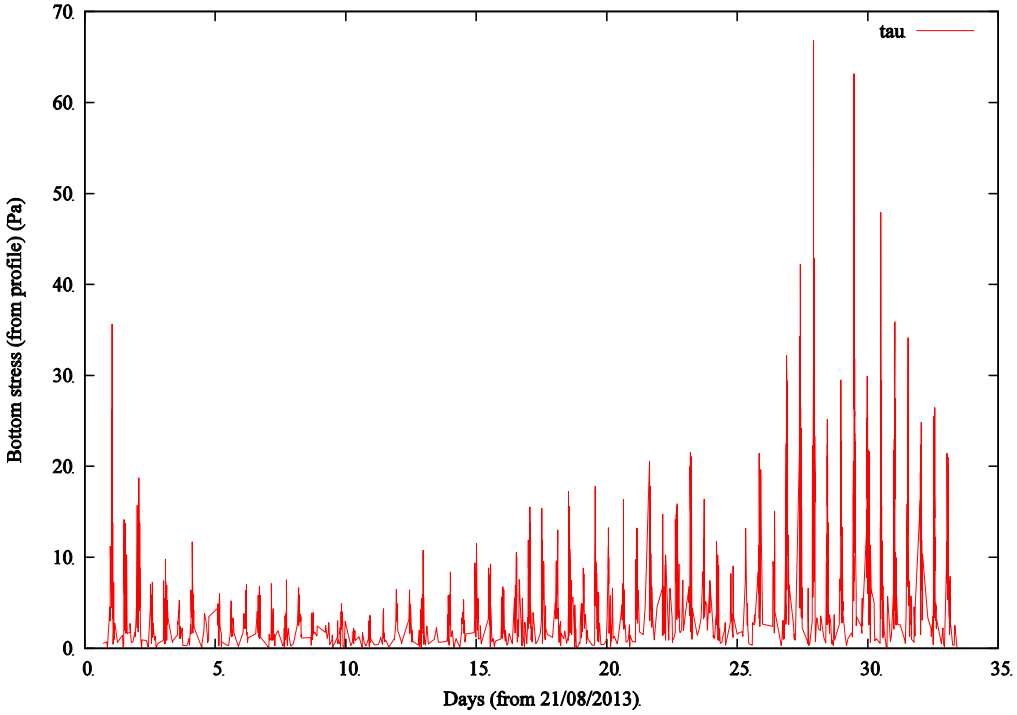

Figure 8: Bottom shear stress, calculated from the current profiles.

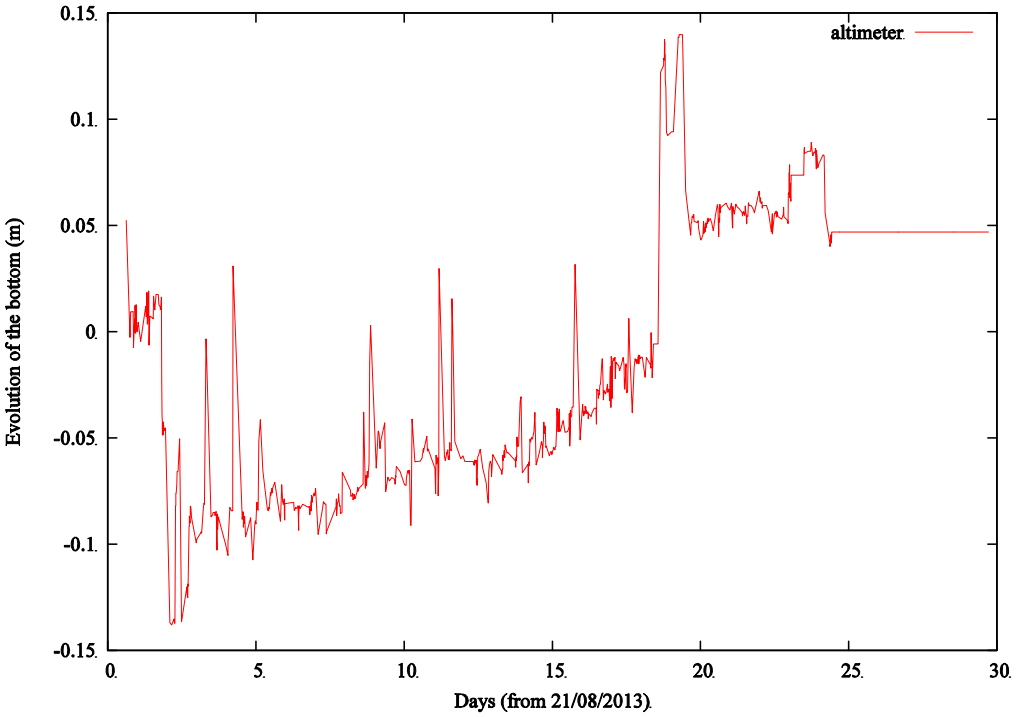

Figure 9: Altimeter data, used to correct the level above the bottom from the current measurements.

The data analysis starts with removing the bad or suspicious bursts. If more than 5 % of the burst data have a correlation (one of the three) that falls below 70 % (or

80 %), the burst data is considered bad and these data are skipped. In total, 220 (490) data burst (8.5 % (19.0 %) of the data) are removed this way. One must remark that the most data were removed in the period with higher waves (after day 21). For the bursts, where less than 5 % of the data have a correlation below 70 %, the bad data, with a correlation below 70 %, were replaced by the mean values at the borders, or were (linearly) interpolated. Also here the most interpolations were executed during the period with higher waves. Finally, the first 17 samples in the burst were removed, during which the compass was not working correctly.

A second step was to remove the spikes from the data. This despiking is executed following the method of Goring and Nikora (2002). In this method the original data, the first and the second derivatives are plotted against each other in a space-phase plot. The points outside the ellipsoid, defined by the Universal criterion are designated as spikes. These spikes are replaced by a third order polynomial using 6 points on either side of the spike. The method iterates until all spikes are removed. An example of the phase-space plots for the first burst is shown in Figure 10.

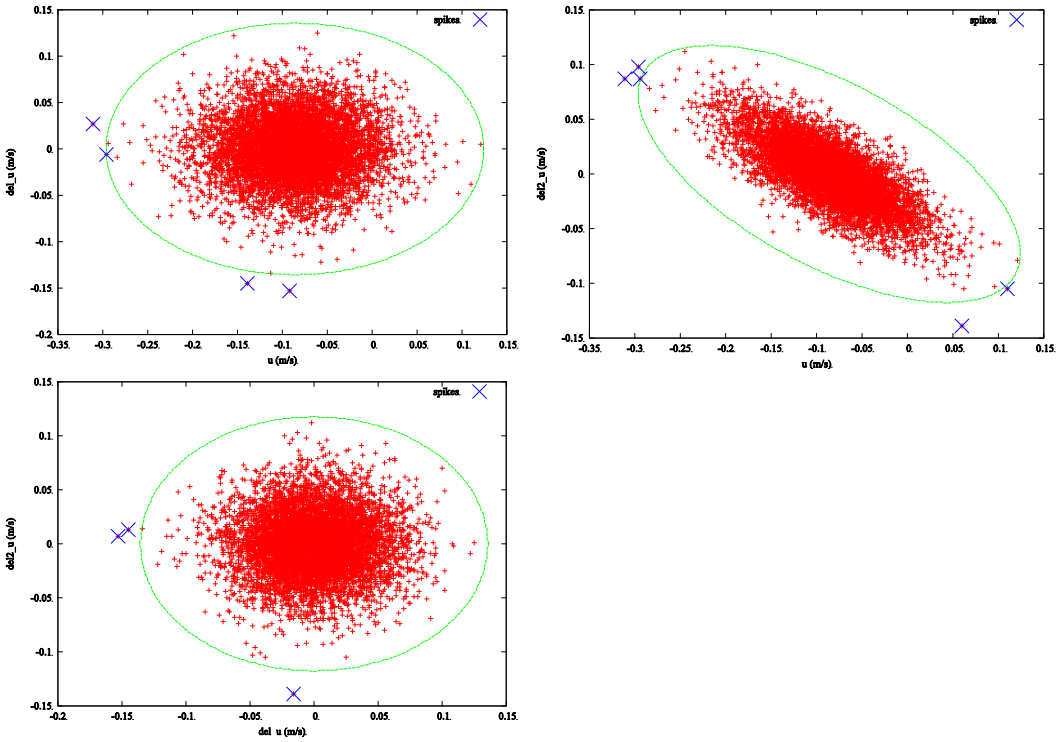

Figure 10: Phase-space plots for the u-velocity of the first burst of the deployment with the ellipsoid defined by the Universal criterion. Left-upper: u-velocity plotted against derivative of u-velocity; right-upper: u-velocity against second derivative of the u-velocity; left-lower: derivative of u-velocity against second derivative of u-velocity.

The total number of spikes, removed in u-velocity, v-velocity and w-velocity is shown in Figure 11. A tidal signal is visible and more spikes are occuring during the period with higher waves. Overall only 206 spikes has to be replaced during one burst, which is less than 1 %.

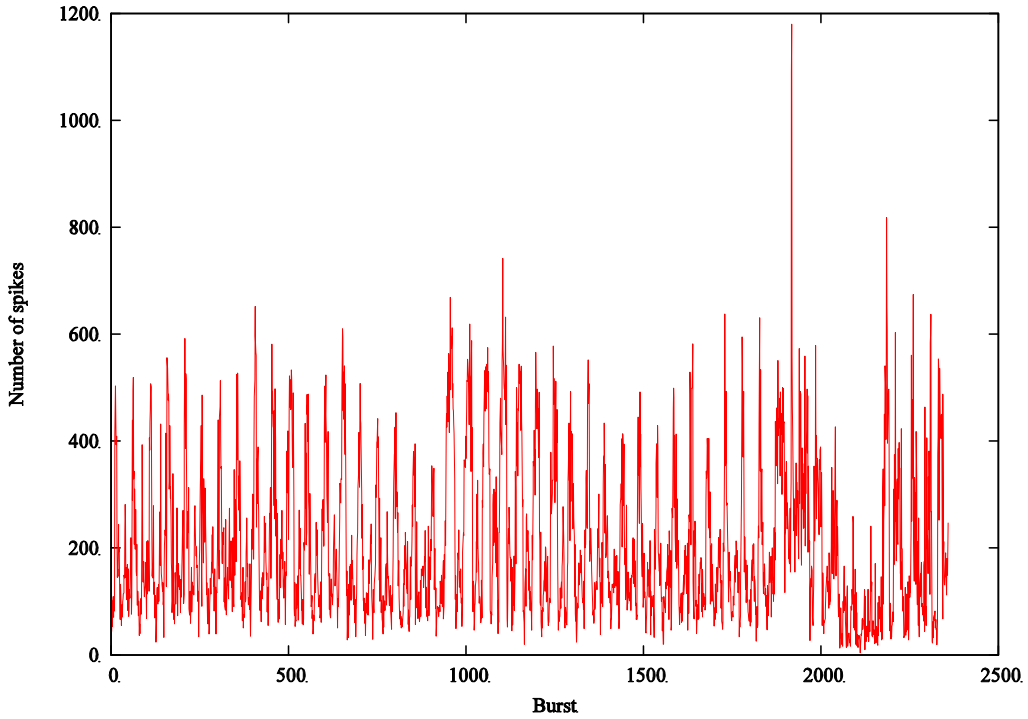

Figure 11: Number of total spikes (u,v,w) over the bursts.

Three methods can be used to calculate the bottom shear stress (e.g. Lecouturier, 2000; Williams *et al.*, 2003), which are discussed shortly hereafter.

4.2.2. Reynold stresses of Eddy Correlation Method

A first method to calculate the bottom shear stress is to calculate the bottom shear stress from the total Reynold stresses (e.g. Huthnance *et al.*, 2002; Williams *et al.*, 2003):

$$\tau = \rho\left(\overline{u'w'}^2 + \overline{v'w'}^2\right)^{1/2} \qquad (11)$$

This method is easy to apply, but the calculations are very sensitive to the correct vertical alignment of the velocimeter (Dyer *et al.*, 2004; Inoue *et al.*, 2011, Huntley, 1988). In theory, waves do not contribute to Reynolds stresses because the horizontal and vertical components of the wave-currents are 90° out of phase. However, if the vertical alignment is not correct, horizontal velocities can 'leak' into estimates of vertical verlocity and vice versa. Different methods are used to correct for this vertical misalignment (e.g., Elgar *et al.*, 2005). In Kim *et al.* (2000) and Lohrman *et al.* (1995) is is suggested to rotate the coordinate system first around the vertical axis until the mean flow is zero along one horizontal axis and afterwards rotating around the the horizontal axis where the mean velocity is zero, until the mean vertical velocity is zero. The rotation was calculated for the data within each tide and for the data within 4 successive tides. The calculated rotations are shown in Figure 12 and Figure 13. One can see that the rotation angles when calculated during each single tide can change considerable. The rotation angle around the vertical axis is around -20°. Indeed, the residual currents at the station

is in the direction WSW (at angle 200°). Rotation around the vertical axis over 20° in clock-wise direction results in a mean velocity in West-direction. The rotation over the vertical axis between 10° and 20°, which is relatively high.

The calculated Reynolds-stresses before and after rotation (calculated over 4 tidal cycles) are shown in Figure 14. While it is expected that during the periods with high waves, the Reynolds-stresses would decrease after rotation of the ADV currents, this is not the case. On the contrary, the Reynolds-stresses increase considerable during the periods with high waves.

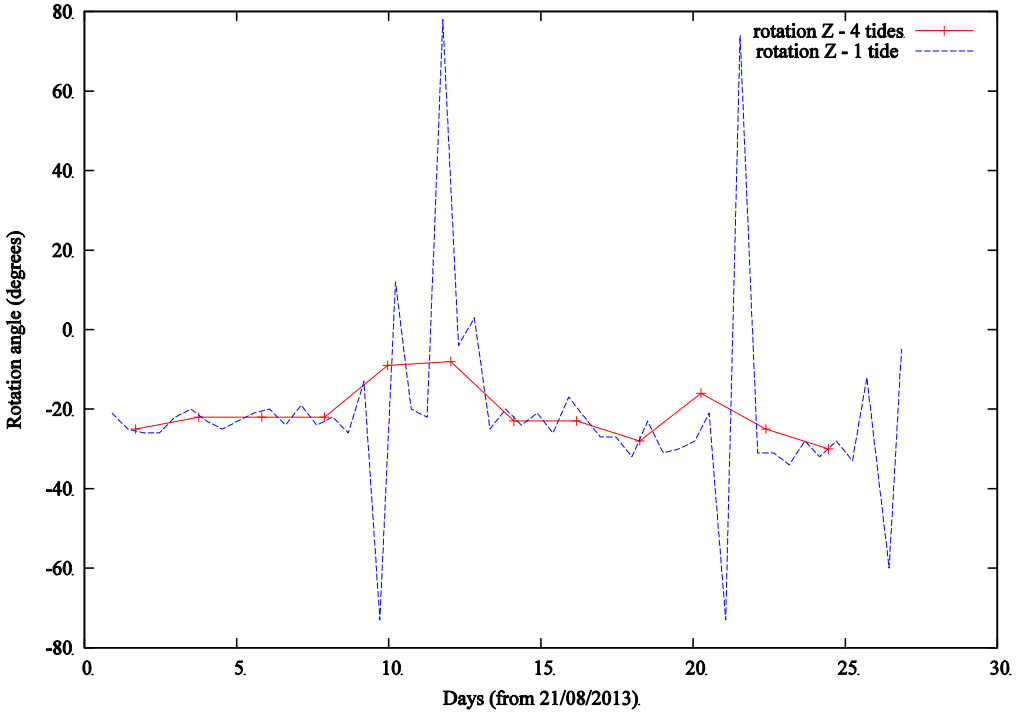

Figure 12: Rotation angle over the Z-axis to correct the vertical alignment of the ADV data.

Therefore another method to rotate the currents, to remove the effect of the waves on the calculation of the Reynolds-stresses was tested. In Lohrman *et al.*, 1995, it was suggested to rotate the currents around the x-axis and y-axis until both the mean vertical velocity is zero and the mean variance of the vertical velocity fluctuations $\overline{w'w'}$ is minimal. Since in this case, the mean vertical velocity and the variance of the vertical velocity fluctuations are calculated for all combinations of rotations over the x- and the y-axis, this method however takes much more computer power. Tests however showed that no better results were obtained using this method.

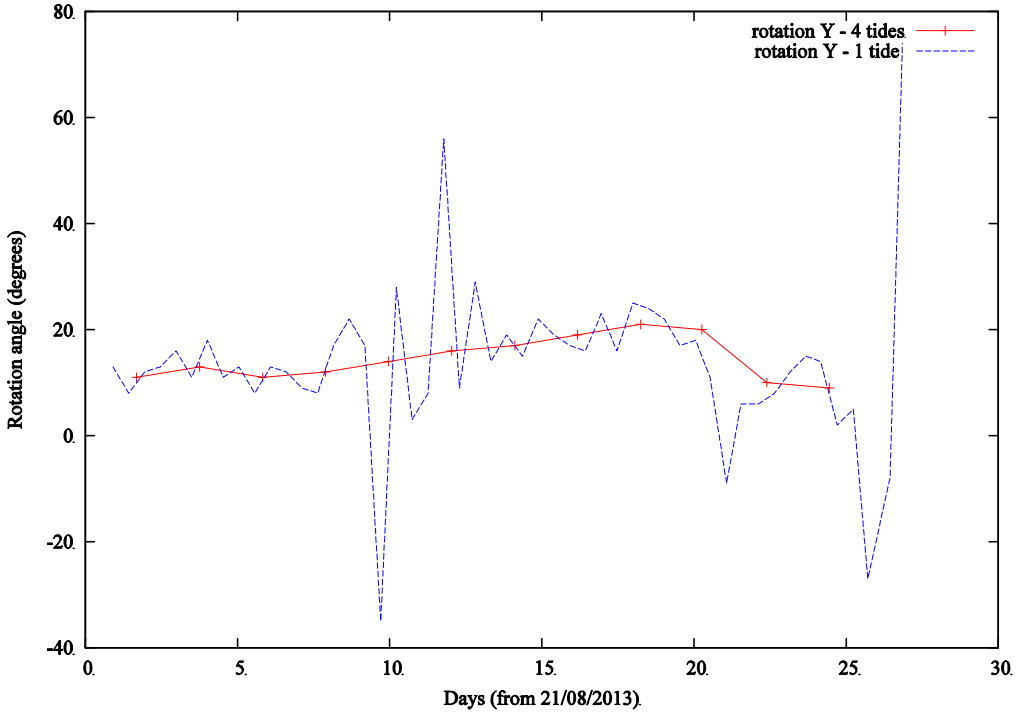

Figure 13: Rotation angle over the Y-axis to correct the vertical alignment of the ADV data.

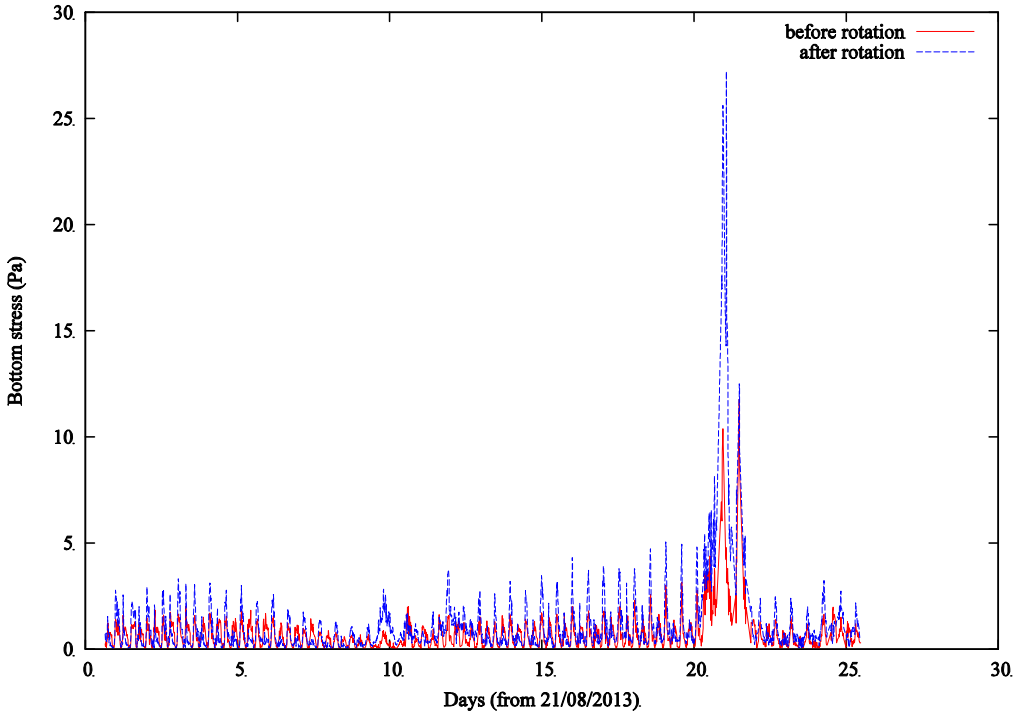

Figure 14: Reynolds-stresses before and after rotation of the ADV velocities.

Remark that in literature, not always good results were obtained using the rotation of the currents. Better estimates of the Reynolds stresses could be obtained by using two ADV sensors near each other (Trowbridge, 1998; Trowbridge and Elgar, 2001).

This technique should be used in the future. Reynolds stresses could also be calculated from the different along-beam velocities from the ADV (Fugate and Chant, 2005; Lohrman *et al.*, 1990; Stacey *et al.*, 1999, Nystrom *et al.*, 2007). Walter *et al.* (2014) uses a spectral phasee decomposition method to separate the turbulent and the wave part in the Reynolds stresses. Also these methods could be explored in the future.

Taking into account the bad results after rotation of the currents, in this study the Reynolds-stresses are used, without rotation.

4.2.3. Intertial dissipation method

In the second method, the intertial dissipation method, the shear velocity if related to the energy dissipation, which is calculated from the velocity spectrum (Huntley, 1988; Sherwood et al., 2006). In the wave spectrum a region exists, the intertial subrange, where three-dimensional spectrum of turbulent motions *E(k)* is scaled by the turbulent dissipation rate ε and decreases with the three-dimenional wave number k at the characteristic -5/3 slope, according to:

$$E(k) = \alpha \varepsilon^{2/3} k^{-5/3} \tag{12}$$

The turbulent dissipation is calculated from a transformed spectrum in a frequency range (typically between 1 Hz And 2.5 Hz) not disturbed by the instrument noise, at higher frequencies. Furthermore the spectrum is further corrected with a correction factor to account for the presence of waves (Trowbridge and Elgar, 2001). In the present model, the turbulent dissipation is calculated from the frequency region, where the slope of the transferred spectrum is closest to zero, i.e., the frequency region where the -5/3 decay rate is the closest followed. Using the turbulent dissipation, the bottom shear stress is then calculated from the following relation:

$$\tau = \rho[\varepsilon \kappa z]^{2/3} \tag{13}$$

An disadvantage of this method is that the bottom shear stress is a function of the height above the bottom. To calculate this height, the measured height above the bottom, using the altimeter of the ADV, is used. Remark that the normalised power density spectrum of the vertical velocity is used, since this normally is less disturbed by noise. More information on this method and the implementation can be found in Francken and Van den Eynde (2010).

A typical power density spectrum for the vertical velocity is shown in Figure 15, with a characteristic -5/3 decay in the higher frequencies. The power density spectrum is calculated, using the despiked data and after detrenting the data. The power density spectrum was calculated with 4096 points (i.e., for 2048 frequencies) and with overlap.

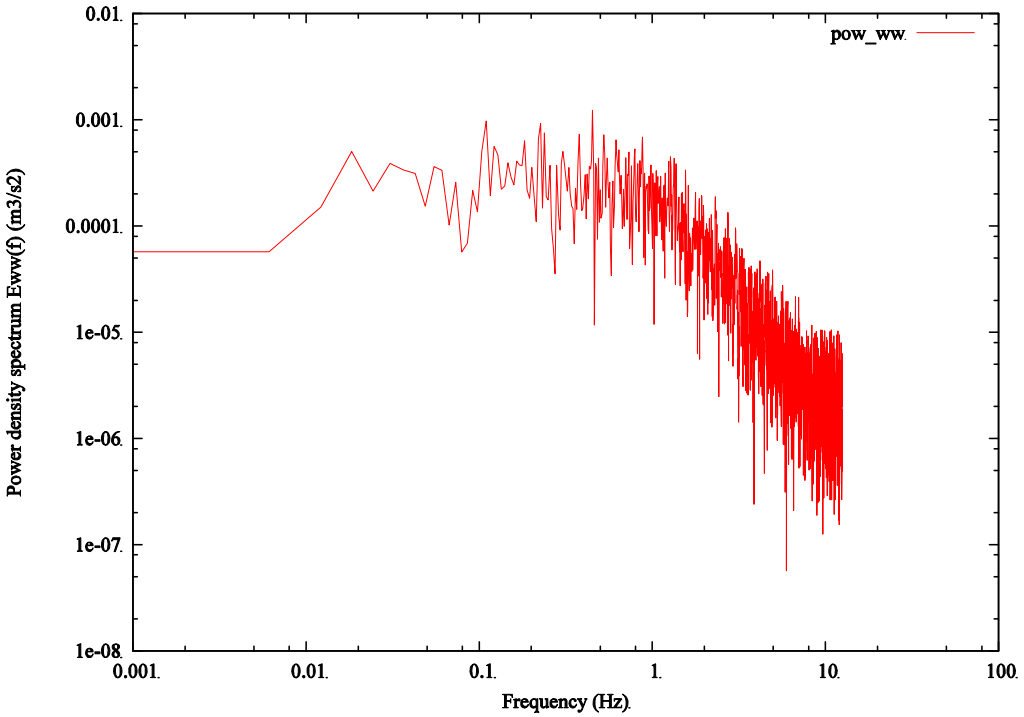

Figure 15: Power density spectrum for the vertical velocity (burst 3).

Remark that the detrenting of the data, before calculating the power density spectrum, results in a slightly higher bottom stress, using the inertial dissipation method, due to the normalisation of the power density spectrum, to the variance of the data.

4.2.4. Turbulent kinetic energy method

A second method to calculate the bottom shear as a function of the total turbulent kinetic energy, which is calculated from the variance of the velocity fluctuations u', v' and w':

$$\tau = C.TKE = C.\rho\left(\overline{u'^2} + \overline{v'^2} + \overline{w'^2}\right) \qquad (14)$$

with the factor C equal to 0.19, as proposed by Stapleton and Huntley (1995) and Thompson *et al.* (2003). The advantage of the method is that this method is quite straightforward. However, the turbulent kinetic energy, mainly the variance of the horizontal velocity fluctuations, is not only influenced by the turbulence but also by the prevailing waves. This is clearly seen in Figure 16, where the power spectral density for the U-velocity is shown for a period with high waves. Between the frequencies 1/6 Hz and 1/25 Hz a increase in the spectrum can be observed with a characteristic well-known -5 power decay, typically for wave spectra. Different methods are available in literature to split the two spectral densities, but in the present study, the method, proposed by Soulsby and Humphery (1990) is used. To calculate the power in the turbulence, the power spectral density in interpolated across the base of the wave peak, as shown in Figure 16. In the same figure, also the effect on the spectral density is shown of detrenting the burst data first. This

detrenting is mainly removing very slow variations, which are not due to turbulence.

As Verney *et al.* (2007) and Verney (2008) suggests the bottom stress, calculated using the total turbulent kinetic energy could be compared to the maximal bottom shear stress under the influence of currents and waves, while the bottom stress, using the turbulent kinetic energy, after removement of the wave and long-period variations, should be a measure of the mean bottom stress under the influence of the waves and the currents. This last bottom stress should be comparable with the bottom shear stress, calculated with the intertial dissipation method, from the Reynolds stresses or from the velocity profile.

4.3. Analysis of the bottom stress measurements

Different techniques were discussed to measure the bottom shear stress, i.e., 1) bottom shear stress, measured from the current profile, 2) bottom shear stress calculated from the inertial dissipation method (with correction for waves) 3) bottom shear stress from the Reynolds stresses and 4) bottom shear stress from the turbulent kinetic energy. Using the last method, a separation can be made between the mean bottom shear stress and the maximum bottom shear stress, during a wave cycle. Unfortunately, not all bottom shear stresses, calculated using the different methods, correlate very well with each other. In Figure 17, the bottom stresses, derived from measurement, using different methods, are shown for the entire deployment. In Figure 18, the results during the first 3.5 days are shown. Remark that for the bottom stresses, derived from the current profiles, the profile from 0.15 to 0.90 mab is used (giving lower bottom stresses than when using the profile from 0.30 to 0.90 mab, see section 4.1).

It can be seen that the bottom stresses, derived from the current profiles and the inertial dissipation method are clearly higher than the bottom stresses, derived using the Reynolds stresses or the turbulent kinetic energy. As mentioned in 4.2.2, the influence of the waves on the bottom stress, derived from the Reynolds stresses is clear, and is mainly a results of the misalignment of the ADV. The (Pearson's) correlation factor r between the different results is given in Table 1. Only the correlation between the bottom shear stress, derived from the turbulent kinetic energy and the intertiall dissipation method is higher than 0.70. For the period with lower waves (days 1 to 19), the correlation factor is a little bit higher and also the correlation factor between the bottom shear stress, derived from turbulent kinetic energy and derived from the Reynolds stresses, is higher than 0.85. During the period with higher waves, the correlation between the different results decrease further.

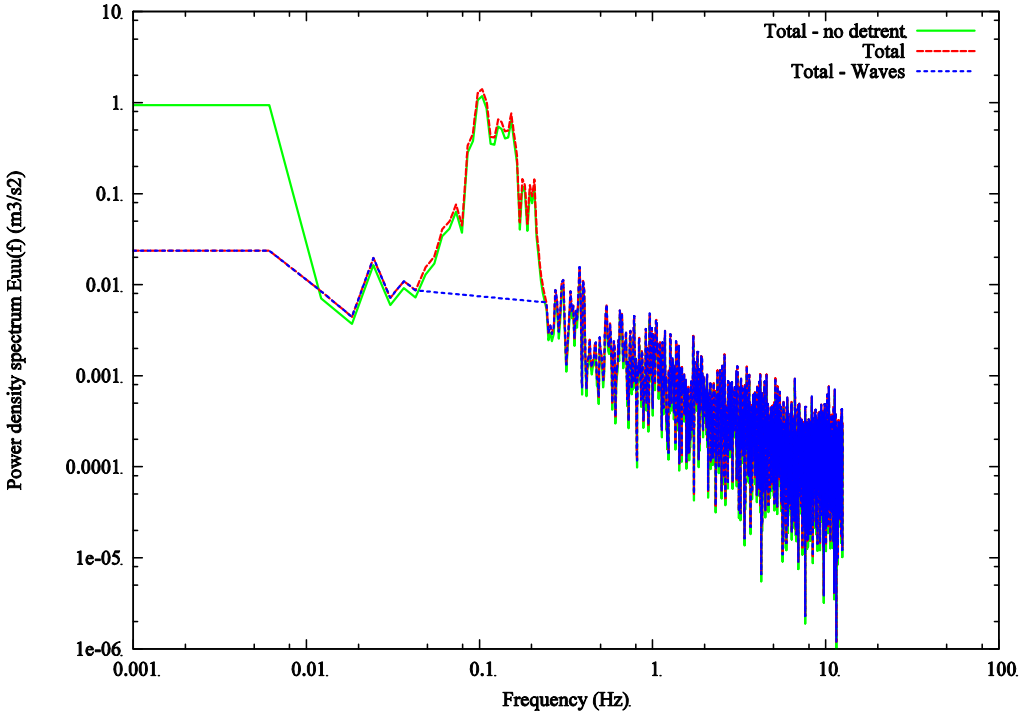

Figure 16: Power density spectrum for the horizontal velocity U during a period with waves (burst 1958). Total power spectrum without detrenting the data (yellow), total power spectrum with detreting the data (red) and power spectrum with waves removed (blue).

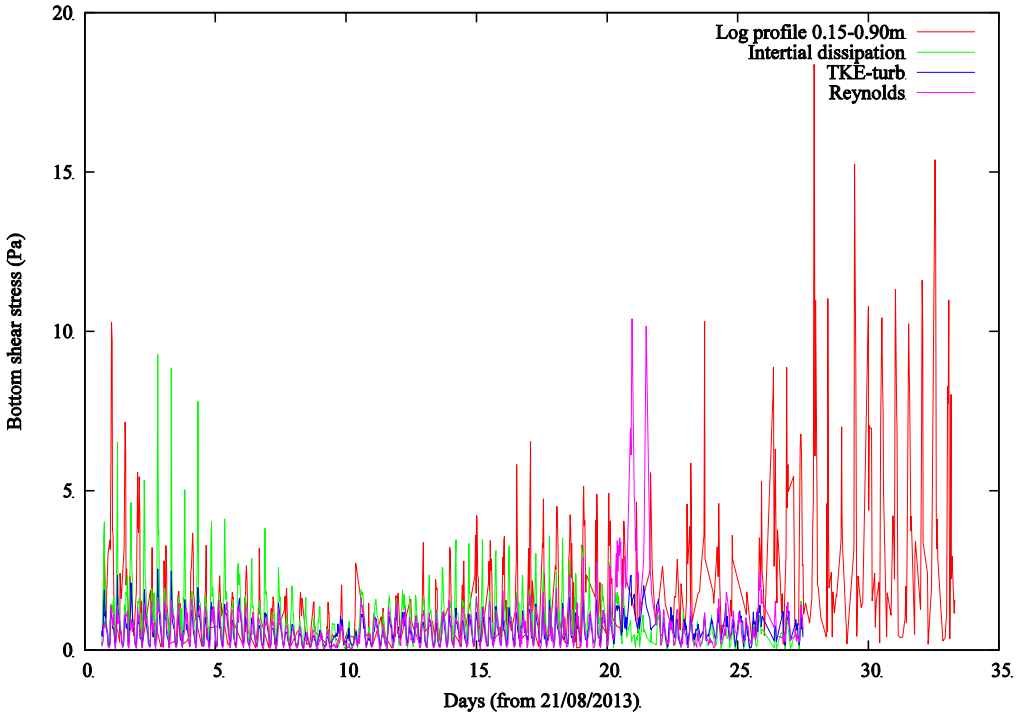

Figure 17: Time series of the different measured bottom stresses.

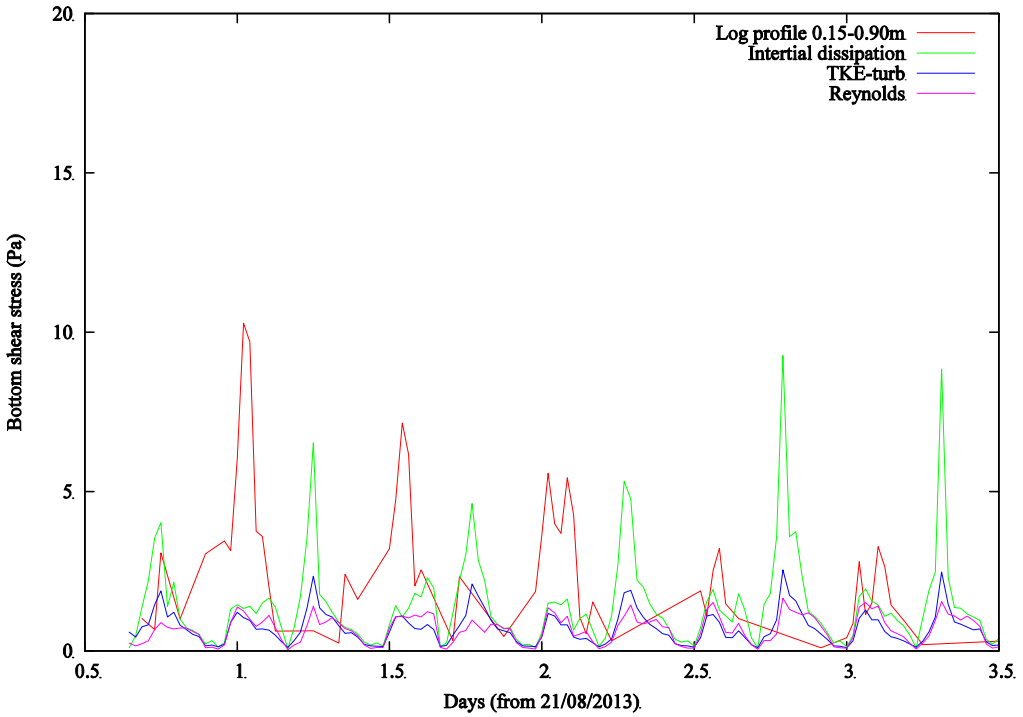

Figure 18: Time series of first 3.5 days of the different measured bottom stresses.

Table 1: Correlation factor between the bottom stresses, derived from measurements with different methods. Inter/I: intertial dissipation method; TKE/T: turbulent kinetic energy method (without waves); Reyn/R: Reynolds stresses; Profile/P: from logarithmic profile. Full: full deployment; No waves: period with lower waves (day 1 – 19); Waves: period with higher waves (day 19 – 27).

	Full				No waves				Waves			
	I	T	R	P	I	T	R	P	I	T	R	P
Inert	1.00	0.74	0.31	0.28	1.00	0.87	0.66	0.35	1.00	0.62	0.26	0.33
TKE	0.74	1.00	0.66	0.46	0.87	1.0	0.85	0.47	0.62	1.00	0.62	0.35
Reyn	0.31	0.66	1.00	0.49	0.66	0.85	1.0	0.57	0.26	0.62	1.00	0.31
Profile	0.28	0.46	0.49	1.00	0.35	0.47	0.57	1.00	0.33	0.35	0.31	1.0

It is clear that the different methods could give quite different results. Given the difficulties with the bottom shear stress derived from the logarithmic profile and with the Reynolds stresses, it is expected that these bottom shear stress estimates are less reliable. Furthermore the intertial dissipation method seems to results in quite high calculated bottom shear stresses. Therefore, it is expected that the best results for the validation will be obtained using the bottom shear stresses, derived from the turbulent kinetic energy. Furthermore, using these bottom shear stresses has the advantage that both the validation of the mean bottom shear stress and of the maximum bottom shear stress can be executed.

5. Validation of the model results

5.1. *Currents and the waves*

In a first section, the validation of the currents and the waves are discussed. For the entire deployment period, the currents were calculated with the OPTOS-BCZ model, while the waves were simulated using the WAM model.

In Figure 19 the model currents results are given for the entire deployment period. One can see that the model results show the same spring-neap tidal cycle as the ADV measurements (see Figure 3). In Figure 20, a comparison is given between the modelled currents and the measurements with the ADP and the ADV for the day 1 to day 4 of the deployment.

For the ADP, the mean over the measured profile is given. The correlation coefficient with the model results is 0.766, with a small bias of -0.013 m/s. The ADP measurements are a slightly smaller than the model results, due to the fact that the measurements are closer to the bottom. It can be seen while in the model results the flood currents are significantly higher than the ebb currents, this is not the case for the ADP measurements, where the ebb currents are higher than the flood currents. It is not clear what is the origin of these differences.

The ADV measurements are similar as the ADP measurement but are a factor 1.66 lower than the ADP measurements. This is again due to the fact that the ADV measurements are taken much more near the bottom at about 0.18 mab. The differences between the ebb and the flood currents are much less for the ADV currents than for the ADP currents. The correlation coefficient between the ADP and the ADV measurements is 0.907.

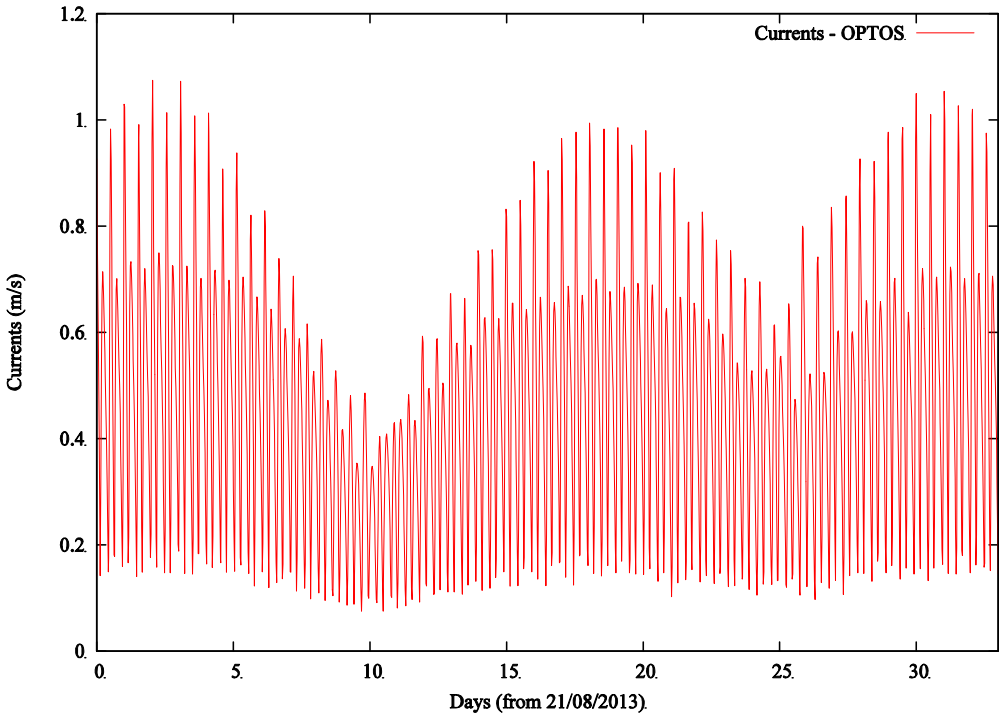

Figure 19: Currents, calculated with the OPTOS-BCZ model during deployment 071.

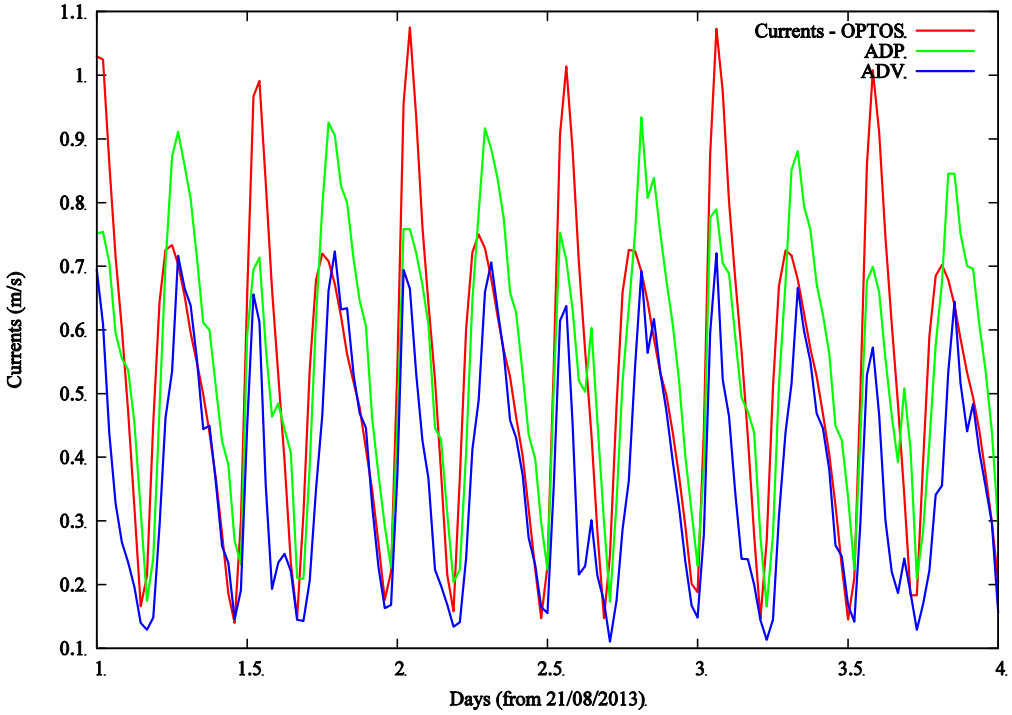

Figure 20: Currents, calculated with the OPTOS-BCZ model, measured currents from the ADP and the ADV for day 1 to day 4.

The current direction is well reproduced by the model, as can be seen in Figure 21.

There is a good agreement between the waves, modelled by the WAM model and the waves measured at the A2-buoy (measurements from Vlaamse Gemeenschap, Afdeling Waterwegen Kust, Meetnet Vlaamse Banken). The correlation between the model results and the measurements is 0.962, the Scatter Index is 22.8 %.

5.2. *Bottom stress with constant bottom roughness*

During the first test, a constant bottom roughness was used to calculate the bottom shear stress. The four different bottom shear stress models were applied. For the mean bottom stress, the model results were compared with the bottom shear stress from the logarithmic profile, the bottom shear stressed, calculated using the intertial dissipation or the eddy correlation method, and the bottom shear stresses, derived from the turbulent kinetic energy, without the influence of the waves. The maximum bottom shear stress is compared with the bottom shear stress, derived from the total turbulent kinetic energy. To be able to compare the model results and the measurements, the measurements were averaged over a period of 30 minutes first.

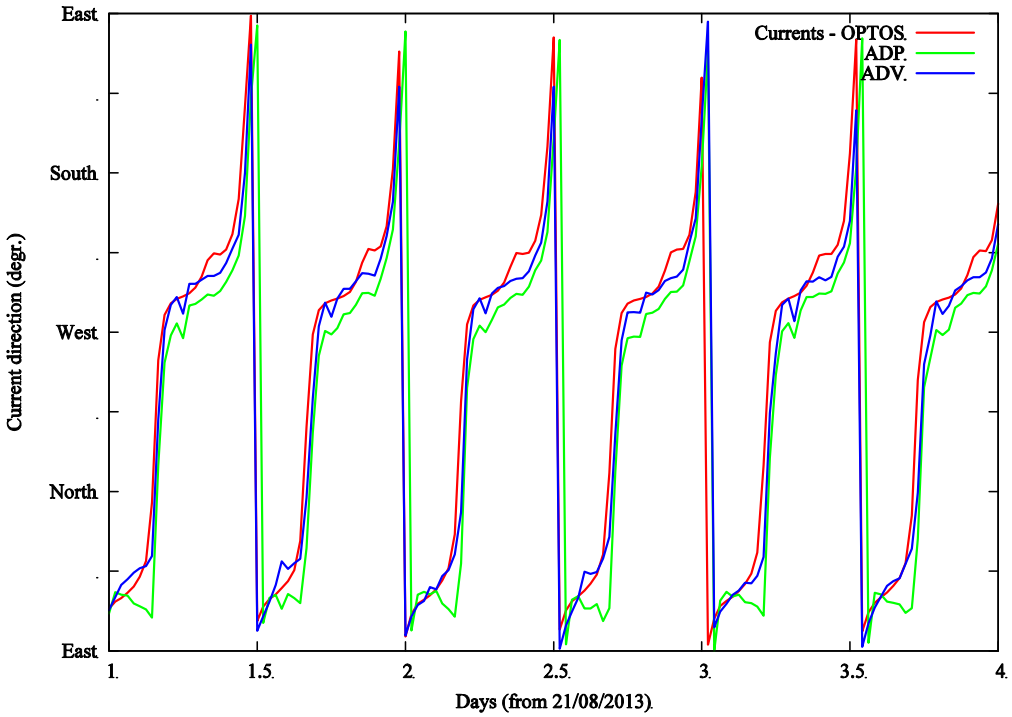

Figure 21: Currents direction, calculated with the OPTOS-BCZ model, measured currents from the ADP and the ADV for day 1 to day 4.

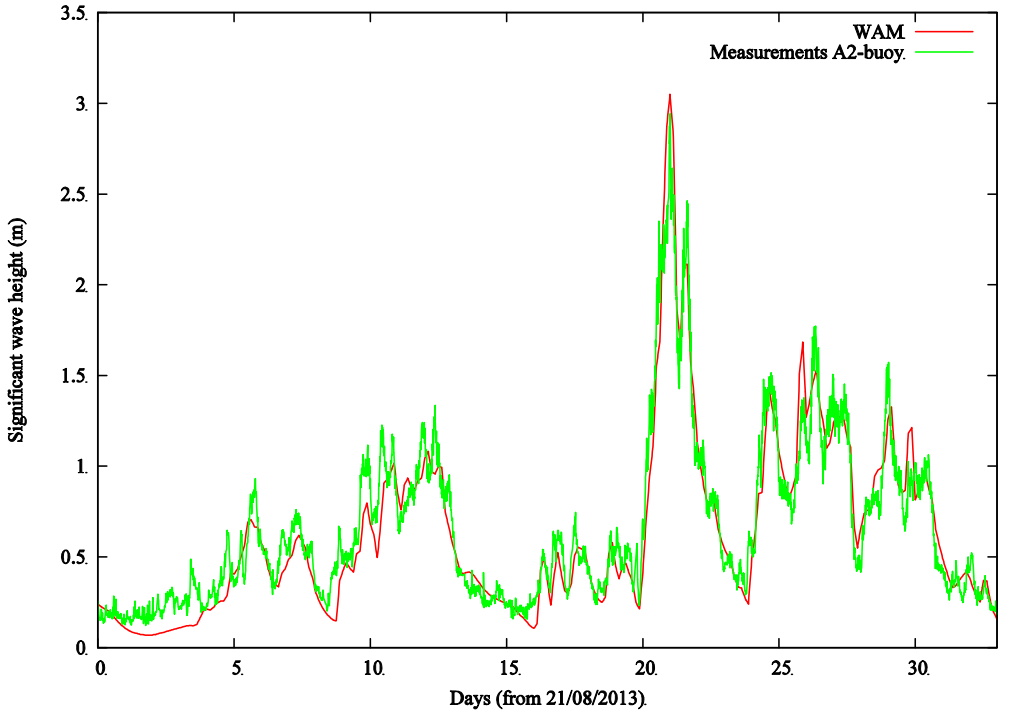

Figure 22: Waves calculated with the WAM model and measurements from the A2-buoy (data from Vlaamse Gemeenschap, Meetnet Vlaamse Banken).

In Table 2, the "best" results for each of the bottom stress measurements are given. The best results are hereby defined as the results with the lowest Root-Mean-Square-Error (RMSE). It is clear that the best results are obtained when using the bottom shear stress, derived from the turbulent kinetic energy, removing the wave influence. In this case, the RMSE remains limited to 0.260 Pa, with a bias of -0.14 Pa. The mean (measured) bottom shear stress is 0.62 Pa. The best result is obtained with the Soulsby model, with a (constant) bottom roughness of 0.01 m.

Table 2: Statistical parameters for the validation of the mean bottom shear stress calculations, using constant bottom roughness.

Measurements	Mean (Pa)	RMSE (Pa)	Bias (Pa)	Corr	Model	Roughn. (m)
TKE-tur	0.624	0.260	-0.136	0.832	Soulsby	0.010
Intertial Dissipation	0.922	0.675	-0.106	0.631	Malarkey-Davies	0.100
Reynolds	0.711	0.618	-0.063	0.628	Soulsby	0.030
Logarithmic Profile	2.429	1.600	-0.392	0.423	Soulsby	0.600

When the model results are compared with the bottom shear stress, derived with the intertial dissipation method or from the Reynolds stresses, the RMSE is around 0.61 Pa. When the bottom stress from the logarithmic profile is used, the RMSE is even much higher, at 1.60 Pa. It is clear that the best results are obtained using the bottom shear stress, derived from the turbulent kinetic energy. Therefore, only the bottom shear stress, derived from the turbulent kinetic energy will be used, further in the report. When comparing the results of the different numerical models, the Soulsby, Soulsby-Clarke and Malarkey-Davies model gives very similar results. The best results for the different models are given in Table 3. While the RMSE are very similar for the different models, the bias is lower for the Soulsby-Clarke model. In this case however, the roughness length is higher (0.03m). Remark however that previous studies showed that the shear stress computation was relatively insensitive to the value of the bottom roughness (Drake and Cacchione, 1986).

Table 3: Statistical parameters for the validation of the mean bottom shear stress calculations, using constant bottom roughness, using the bottom shear stress from the turbulent kinetic energy.

Model	Mean (Pa)	RMSE (Pa)	Bias (Pa)	Corr	Measurements	Roughness (m)
Soulsby	0.624	0.260	-0.136	0.832	TKE-tur	0.010
Soulsby-Clarke	0.624	0.262	-0.024	0.829	TKE-tur	0.030
Malarkey-Davies	0.624	0.265	-0.143	0.831	TKE-tur	0.010

Remark finally that the results during the first period, with lower waves (21/8/2013 till 9/9/2013), the results are slightly better than during the period with higher waves (9/9/2013-27/9/2013). For the Soulsby model, with a bottom roughness of 0.010 m, the RMSE for the first period is 0.220 Pa, while for the second period, the RMSE increases to 0.344 Pa. The modelled results with the Soulsby and the Soulsby-Clarke model are shown in Figure 23 to Figure 25. The

results are clearly satisfactory.

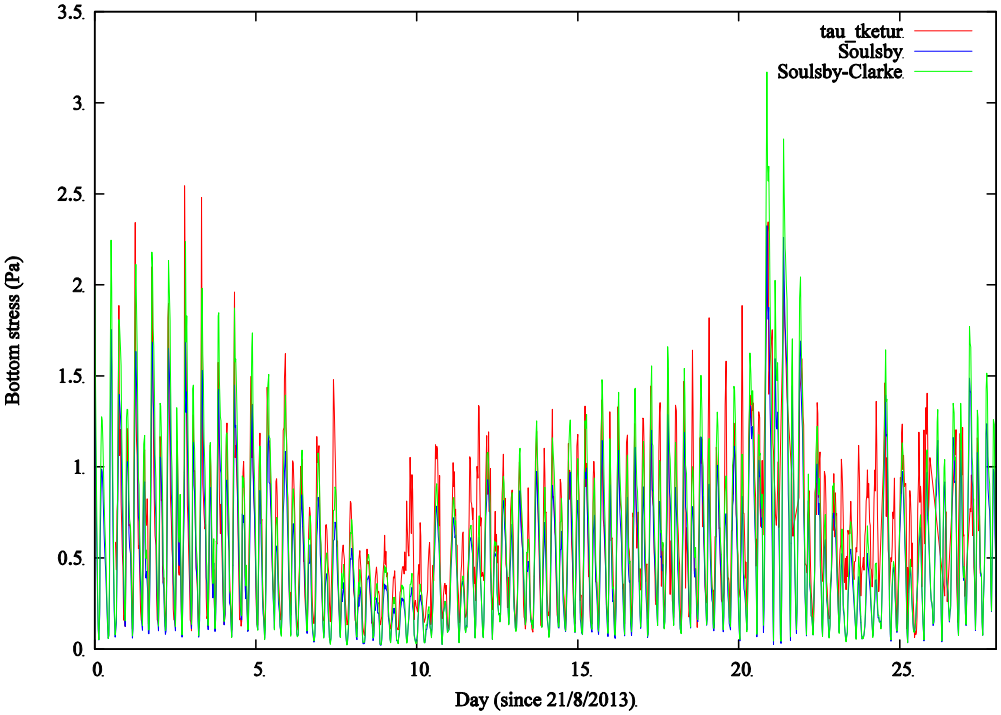

Figure 23: Time series of the mean bottom shear stress, derived from the turbulent kinetic energy and modelled using the Soulsby and the Soulsby-Clarke method.

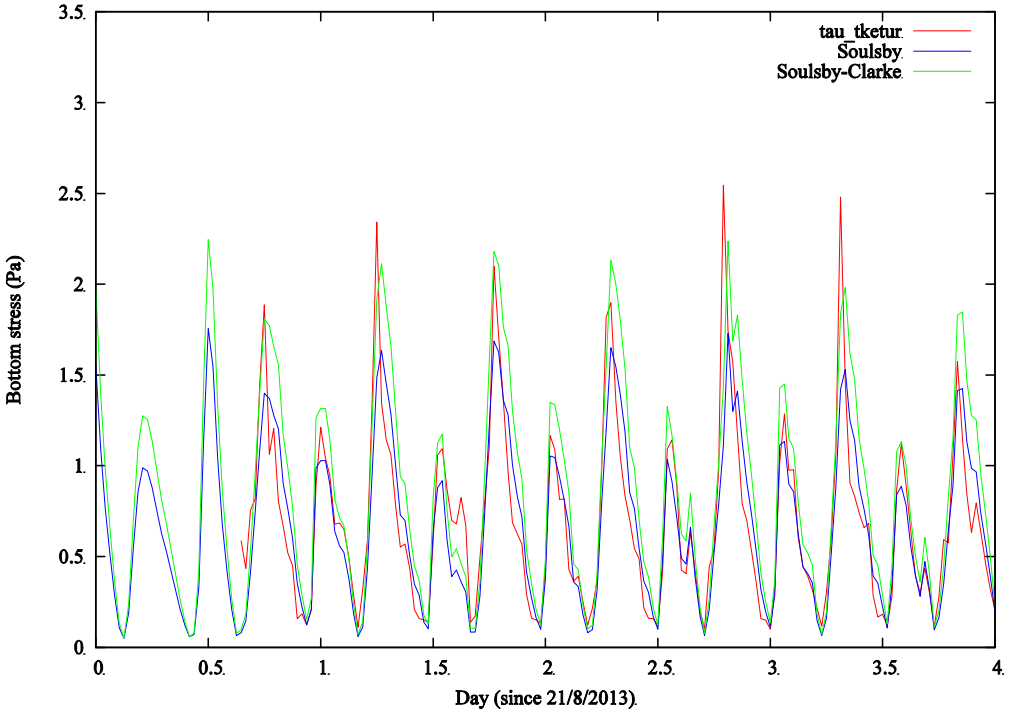

Figure 24: Time series of the mean bottom shear stress, derived from the turbulent kinetic energy and modelled using the Soulsby and the Soulsby-Clarke method for day 0 to day 4.

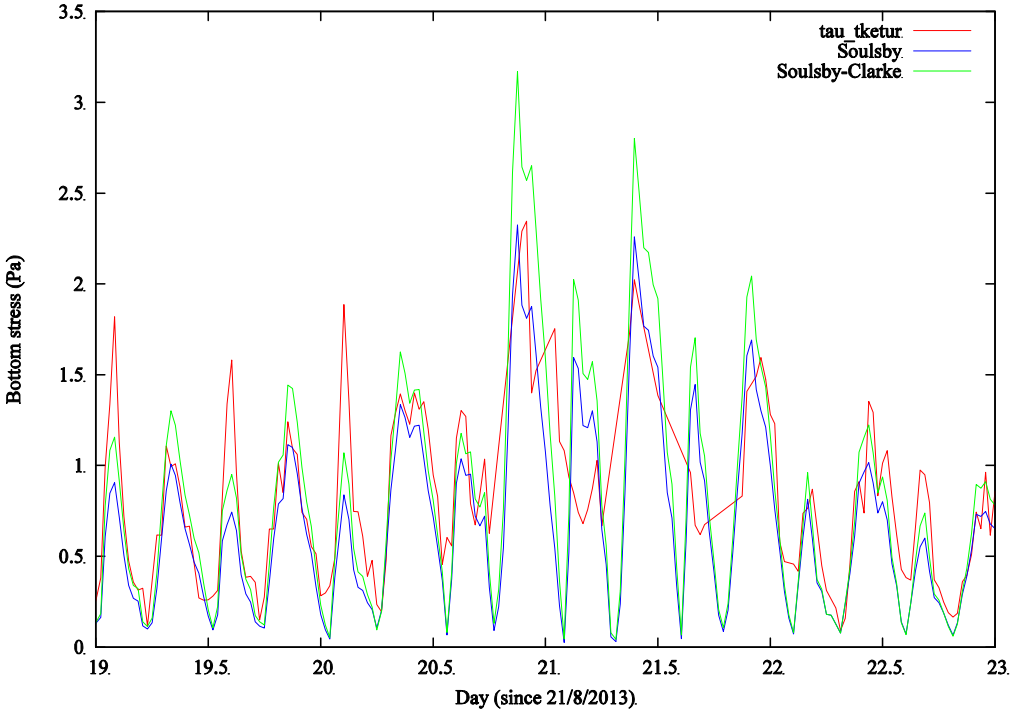

Figure 25: Time series of the mean bottom shear stress, derived from the turbulent kinetic energy and modelled using the Soulsby and the Soulsby-Clarke method for day 19 to day 23.

Using the bottom shear stress from the total turbulent kinetic energy, also the modelled maximum bottom shear stress can be validated (Verney *et al.*, 2007; Verney, 2008). The results of the different models are presented in Table 4.The results for the different model are again very similar. Best results are obtained by the Soulsby-Clarke model, with a bottom roughness of 0.010 m. In this case the RMSE is 0.62 Pa (compared to a mean of the measurements of 1.16 Pa). Also the Soulsby model obtains the best results with a bottom roughness of 0.010 m. Again, the bias is a little bit lower for the Soulsby-Clarke model.

Table 4: Statistical parameters for the validation of the maximum bottom shear stress calculations, using constant bottom roughness.

Model	Mean (Pa)	RMSE (Pa)	Bias (Pa)	Corr	Measurements	Roughness (m)
Soulsby	1.164	0.624	-0.103	0.939	TKE-tot	0.010
Soulsby-Clarke	1.164	0.616	-0.070	0.940	TKE-tot	0.010
Malarkey-Davies	1.164	0.698	0.060	0.920	TKE-tot	0.007

In Figure 26 to Figure 28, the time series for the maximum bottom shear stress are shown, together with the Soulsby and the Soulsby-Clarke model results, both with a bottom roughness of 0.01 m. One can see that during the period with high waves (Figure 28) the Soulsby-Clarke model underestimates the measurements, while the Soulsby model overestimates them. Overall the results are certainly satisfactory.

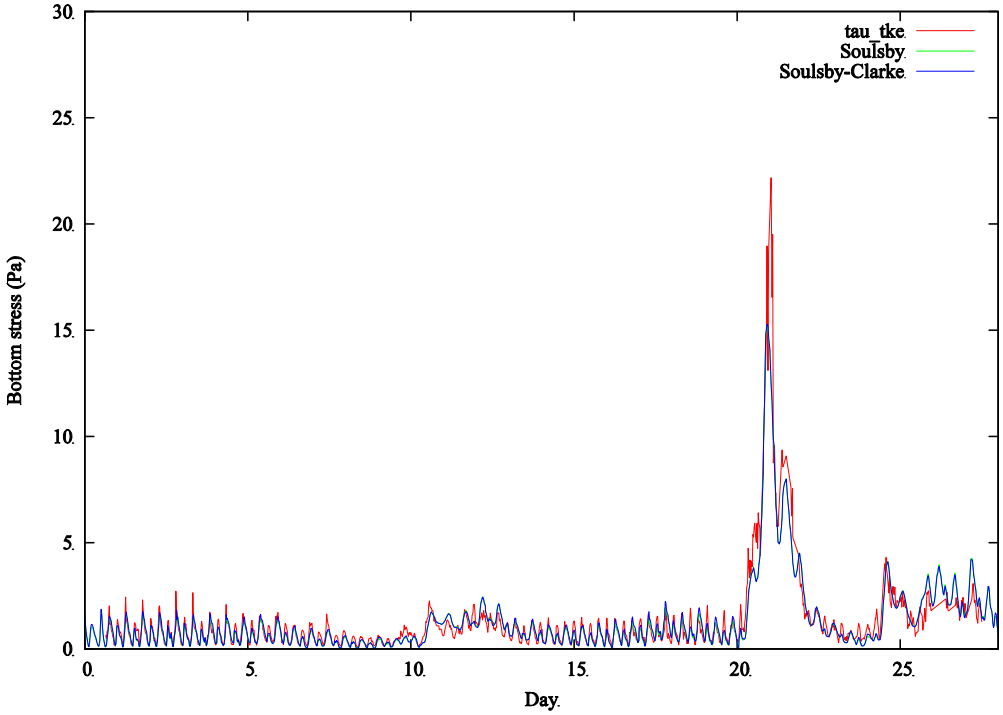

Figure 26: Time series of the maximum bottom shear stress, derived from the turbulent kinetic energy and modelled using the Soulsby and the Soulsby-Clarke method.

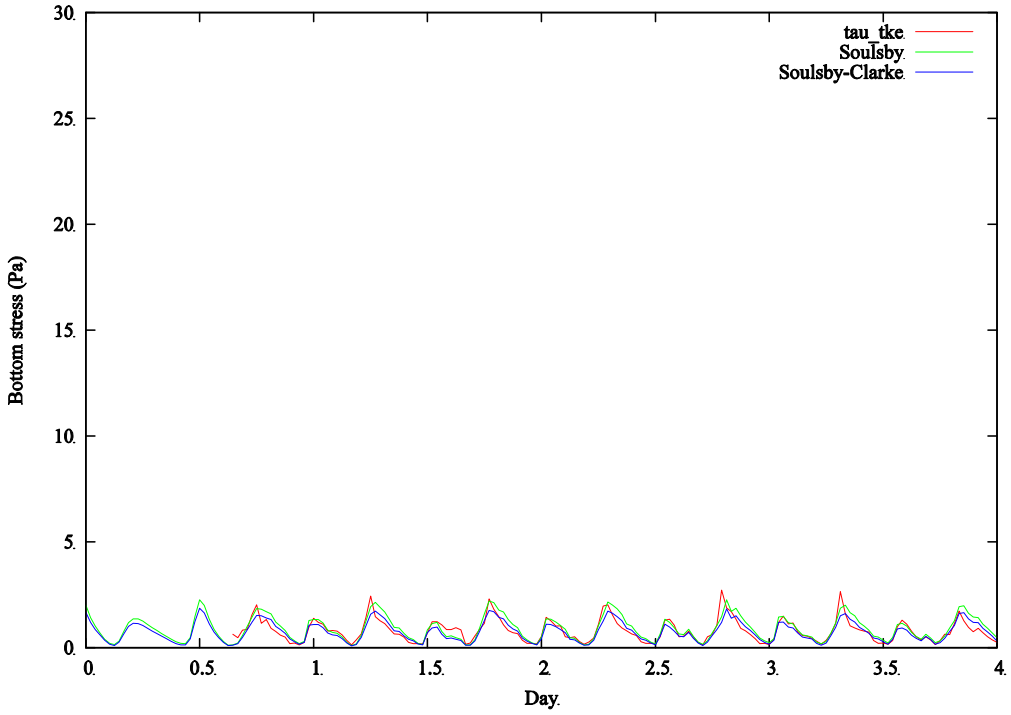

Figure 27: Time series of the maximum bottom shear stress, derived from the turbulent kinetic energy and modelled using the Soulsby and the Soulsby-Clarke method for day 0 to day 4.

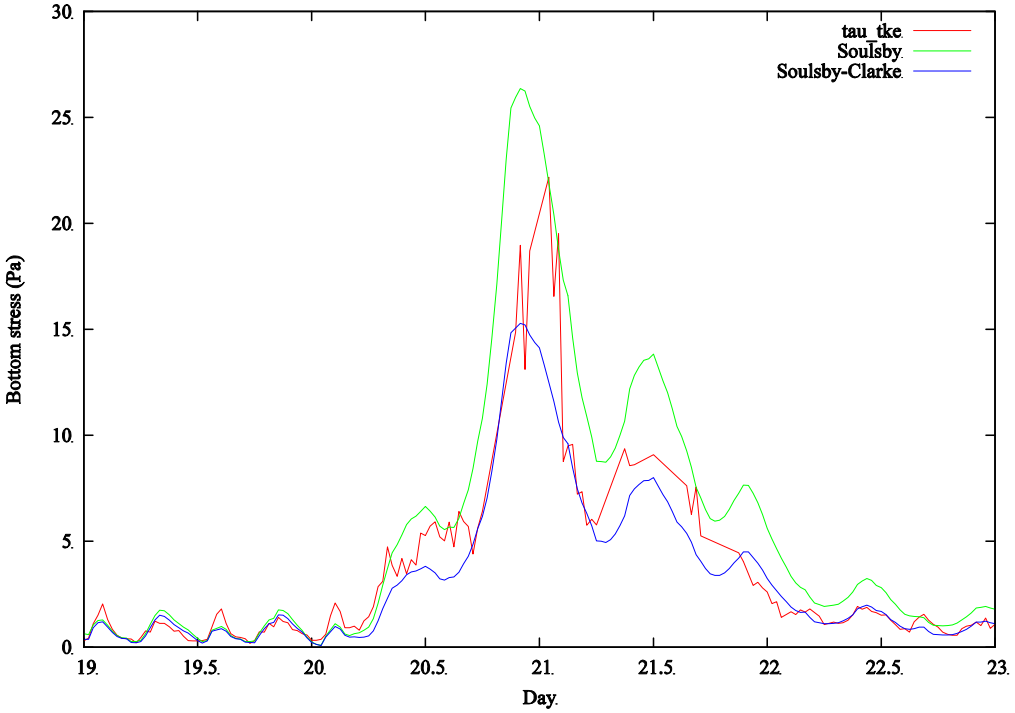

Figure 28: Time series of the maximum bottom shear stress, derived from the turbulent kinetic energy and modelled using the Soulsby and the Soulsby-Clarke method for day 19 to day 23.

5.3. *Bottom shear stress with calculated bottom roughness*

Instead of applying a chosen constant bottom roughness, the bottom roughness can be calculated by the model, using empirical formulations for the form bottom roughness and the roughness, due to bed load, and using empirical formulations for the height and the length of the bottom ripples (see section 3.4.5). In this way, the bottom roughness can vary of the deployment period, which could improve the model results.

In Table 5, the best results for the different numerical models are given. It can be seen that the results are less good than the results with a constant (chosen) bottom roughness. In this case the Soulsby-Clarke model gives the best results, but the RMSE is increased to 0.35 Pa, with a bias of 0.11 Pa. The Malarkey-Davies and certainly the Soulsby model given even worse results. The best results were obtained with the Nielsen model, for the calculation of the bottom roughness due to bedload and the Soulsby-Whitehouse model for the prediction of the ripple geometry. However, the predicted bottom roughness is too high.

Table 5: Statistical parameters for the validation of the mean bottom shear stress calculations, using calculated bottom roughness.

Model	Mean (Pa)	RMSE (Pa)	Bias (Pa)	Corr	Bedload	Ripple	Fac
Soulsby	0.624	0.462	0.199	0.786	Nielsen	Soulsby-W	1.00
Soulsby-Clarke	0.624	0.351	0.106	0.817	Nielsen	Soulsby-W	1.00
Malarkey-Davies	0.624	0.363	0.118	0.816	Nielsen	Soulsby-W	1.00

Tests were executed with a correction factor, with which the calculated bottom roughness was multiplied. This would allow the bottom roughness to vary over the period, due to the changing currents and waves, but would scale them to the correct order of magnitude to predict the bottom shear stress as good as possible. The results are given in Table 6.

Table 6: Statistical parameters for the validation of the mean bottom shear stress calculations, using calculated bottom roughness and using a correction factor.

Model	Mean (Pa)	RMSE (Pa)	Bias (Pa)	Corr	Bedload	Ripple	Fac
Soulsby	0.624	0.252	-0.123	0.836	Soulsby	Soulsby-GM	0.10
Soulsby-Clarke	0.624	0.255	-0.015	0.832	Nielsen	Soulsby-GM	0.30
Malarkey-Davies	0.624	0.259	-0.060	0.818	Nielsen	Soulsby-W	0.30

The results are slightly better than the results obtained with a constant bottom roughness. The best result is obtained by the Soulsby model, using the Soulsby model for the bed roughness, due to bedload and the Soulsby-Grant-Madsen model for calculating the bottom ripple geometry, using a correction factor of 0.10. A RMSE of 0.25 Pa and a bias of -0.12 Pa is obtained. Remark that the correction factor is dependent on the models, used for the calculation of the bottom roughness. Overall the correction factor varies between 0.10 and 0.30, which means that the bed roughness is overpredicted by the models. The results for the bottom shear stress, with and without a correction factor are shown in Figure 29 to Figure 31.

Also the maximum bottom shear stress can be modelled using a calculated bottom roughness. The results without a correction factor are however not good, with a large overprediction of the bottom shear stress (see Table 7). The RMSE is more than 2.7 Pa, with a bias of more than 1.5 Pa. Using a correction factor of 0.10 again, the results are much improved and a RMSE of 0.65 Pa is obtained, with a bias of -0.01 Pa, when the Soulsby-Clarke model is used. This is however still larger than the results obtained with a constant bottom roughness.

Table 7: Statistical parameters for the validation of the maximum bottom shear stress calculations, using calculated bottom roughness, with and without a correction factor.

Model	Mean (Pa)	RMSE (Pa)	Bias (Pa)	Corr	Bedload	Ripple	Fac
Soulsby	1.164	2.856	1.601	0.871	Nielsen	Soulsby-GM	1.00
Soulsby-Clarke	1.164	2.763	1.500	0.873	Nielsen	Soulsby-GM	1.00
Malarkey-Davies	1.164	2.913	1.866	0.885	Nielsen	Soulsby-GM	1.00
Soulsby	1.164	0.659	-0.043	0.925	Soulsby	Soulsby-GM	0.10
Soulsby-Clarke	1.164	0.650	-0.008	0.928	Soulsby	Soulsby-GM	0.10
Malarkey-Davies	1.164	0.728	0.257	0.921	Soulsby	Soulsby-GM	0.10

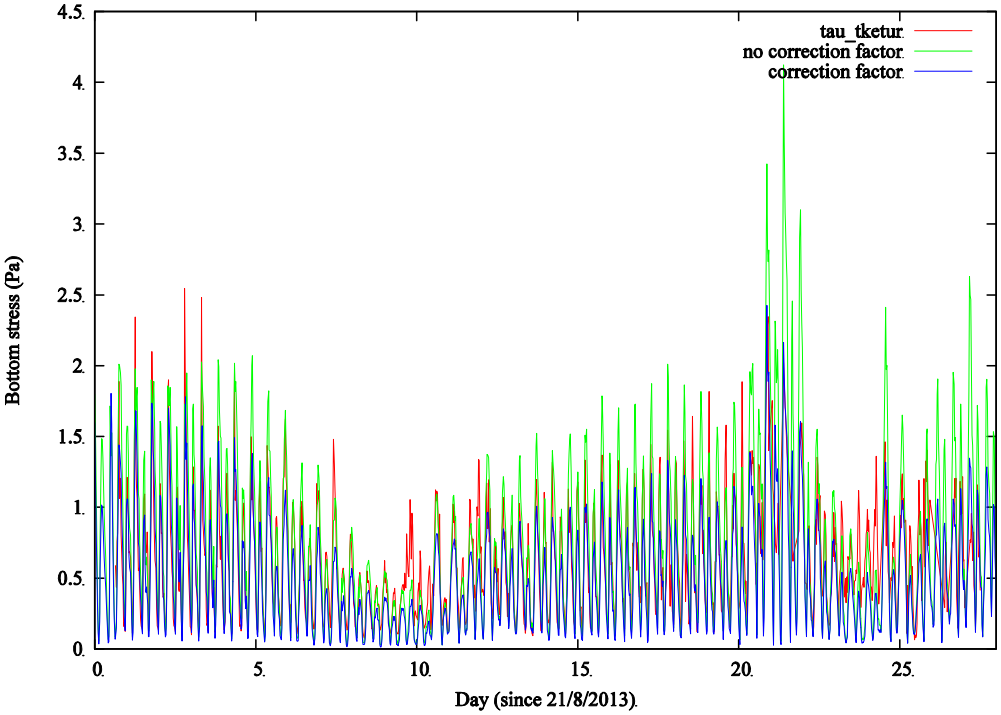

Figure 29: Time series of the mean bottom shear stress, derived from the turbulent kinetic energy and model results. The model uses a predicted bottom roughness, with and without correction factor.

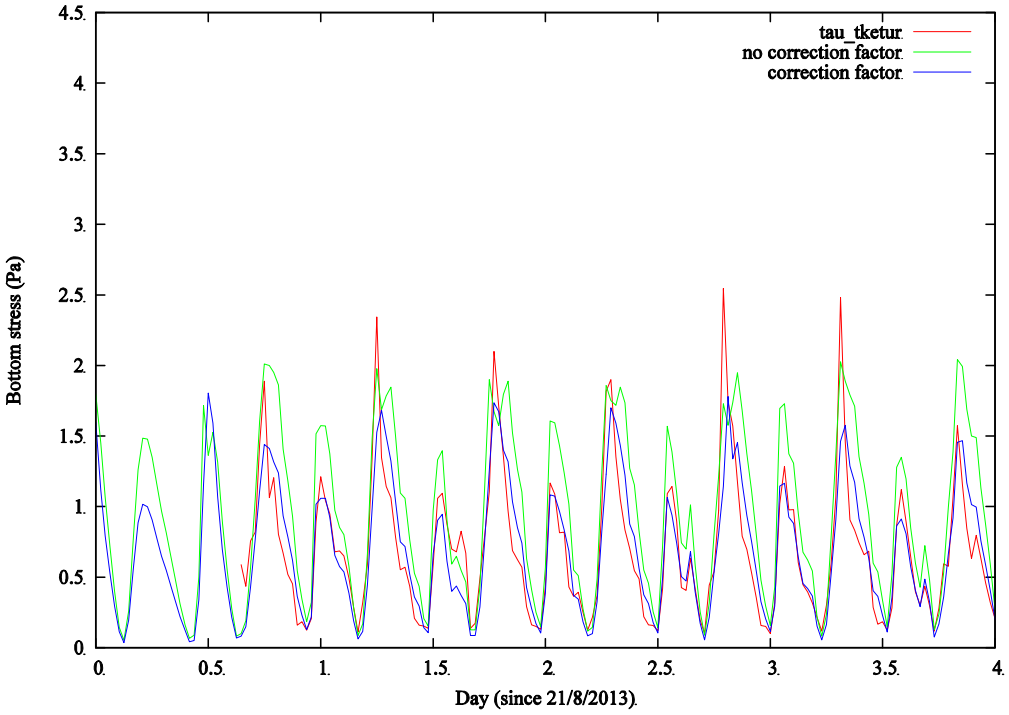

Figure 30: Time series for day 0 to day 4 of the mean bottom shear stress, derived from the turbulent kinetic energy and model results. The model uses a predicted bottom roughness, with and without correction factor.

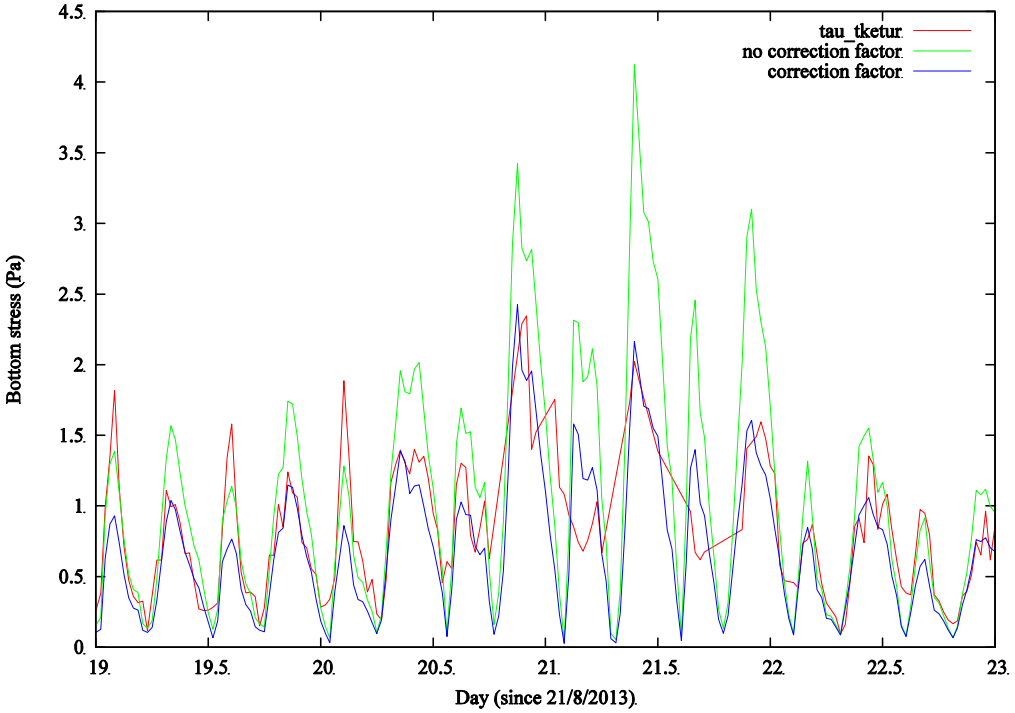

Figure 31: Time series for day 19 to 23 of the mean bottom shear stress, derived from the turbulent kinetic energy and model results. The model uses a predicted bottom roughness, with and without correction factor.

5.4. *Conclusions*

The validation of the currents and the waves showed that the hydrodynamic and wave models provide satisfying results. However, some difficulties in the ebb and flood currents seem to occur, for which no good explanation is available for now.

The validation of the bottom shear stress made it clear that the most reliable method for calculating the bottom shear stress from current measurements is the turbulent kinetic energy method. Furthermore, when this method is used, both the mean bottom shear stress and the maximum bottom shear stress can be derived from the high frequency current measurements.

During the validation of the numerical models for the bottom shear stress, similar results were obtained with the different models. The best results were obtained with a bottom roughness of 0.01 m. Using that value, a RMSE for the mean bottom shear stress in the order of 0.26 Pa was obtained, with a high correlation coefficient. The RMSE for the maximum bottom shear stress was around 0.62 Pa.

When the bottom shear stress was calculated by empirical models, the obtained bottom roughness was too high. Using a correction factor of 0.10, results were much improved. Although the results for the mean bottom shear stress were slightly better than using a constant bottom shear stress, the maximum bottom shear stress was less well modelled. Therefore it is not recommended to use the predicted bottom roughness, but to use a constant bottom roughness of 0.10 m.

6. Conclusions

In the present report, current data from a deployment at the MOW1 station, near the sea harbour of Zeebrugge, were analysed to derive the bottom shear stresses and to validate numerical modesl of bottom shear stresses.

The deployment was executed from August, 21, 2013 to September 27 2013. The instruments included a high frequency (25 Hz) ADV current meter, and a ADP, measuring the current profile over the lowest part of the water column. During the first 20 days, weather was calm and the waves remain limited to less than 1.2 m. After that, waves were higher, with a peak of 3 m wave height at day 21.

The numerical models were discussed first. Three models for the bottom shear stress calculation under the influence of currents and waves were presented, that will be used in the validation exercise.

Further, four methods were described to derive the bottom shear stress from the current measurements: using the logarithmic profile, using the Reynolds stresses, using the inertial dissipation method or using the turbulent kinetic energy. Pre-processing of the data, including despiking the data, was executed first. To improve the quality of the bottom shear stress from the Reynolds stress, the ADV currents were rotated to remove the influence of the waves. These attempts however were not successful. Analysis showed very low correlation between the different estimates of the bottom shear stresses. While the bottom shear stresses from the Reynolds stresses were clearly polluted by the waves, the bottom shear stresses from the logarithmic profiles and from the inertial dissipation method seemed rather high. It was concluded that the bottom shear stress from the turbulent kinetic energy probably was the most accurate estimate of the bottom shear stress. Furthermore, using the turbulent kinetic energy, both an estimate could be made of the mean (averaged over a wave cycle) bottom shear stress and the maximum bottom shear stress.

The validation of the currents and the waves showed that the hydrodynamic and wave models provide satisfying results. However, some difficulties in the ebb and flood currents seem to occur, for which no good explanation is available for now.

The validation of the bottom shear stress made it clear that the most reliable method for calculating the bottom shear stress from current measurements is the turbulent kinetic energy method. Furthermore, when this method is used, both the mean bottom shear stress and the maximum bottom shear stress can be derived from the high frequency current measurements.

During the validation of the numerical models for the bottom shear stress, similar results were obtained with the different models. The best results were obtained with a bottom roughness of 0.01 m, which is still relatively high. Using that value, a RMSE for the mean bottom shear stress in the order of 0.26 Pa was obtained, with a high correlation coefficient. The RMSE for the maximum bottom shear stress was around 0.62 Pa.

When the bottom shear stress was calculated by empirical models, the obtained bottom roughness was too high. Using a correction factor of 0.10, results were

much improved. Although the results for the mean bottom shear stress were slightly better than using a constant bottom shear stress, the maximum bottom shear stress was less well modelled. Therefore it is not recommended to use the predicted bottom roughness, but to use a constant bottom roughness of 0.10 m.

Overall, one can conclude that using a constant bottom roughness of 0.1 m, satisfying results can be obtained when modelling the bottom shear stress. However, the fact that the measured bottom shear stress, using different techniques doesn't correlate very well with each other, makes the results of this study still uncertain. It is clear that more research has to be done to evaluate the measurements and to obtain in the future high quality measurements of the bottom shear stress. Only in this way, a solid validation of the model results can be achieved.

In the future, an analysis will be made on the dependency of the bottom roughness length to be used on the water depth, the maximum current or the significant wave height, based on different deployment. Furthermore, it could be useful to obtain new, high quality, measurements of the bottom shear stress. Using two ADV sensors near each other could improve the estimate of the Reynolds stresses, which could provide a second good estimate of the bottom shear stress, apart from the bottom shear stress, derived from the turbulent kinetic energy.

7. References

Bijker, E.W., 1966. The increase of bed shear in a current due to wave motion. In: Proceeding 10th Conference on Coastal Engineering, Tokyo, 746-765.

Drake, D.E. and D.A. Cacchione, 1986. Field observations of bed shear stress and sediment resuspension on continental shelves, Alaska and California. Continental Shelf Research, 6, 415-429.

Drake, D.E., D.A. Cacchione and W.D. Grant, 1992. Shear stress and bed roughness estimates for combined wave and current flows over a rippled bed. Journal of Geophysical Research, 97, 2319-2326.

Dujardin, A., D. Van den Eynde, J. Vanlede, J. Ozer, R. Delgado and F. Mostaert, 2010. BOREAS - Belgian Ocean Energy Assessment: A comparison of numerical tidal models of the Belgian part of the North Sea. Version 2_0. WL Rapporten, 814_03. Flanders Hydraulics Research, Soresma & MUMM: Antwerp, Belgium. BELSPO contract SD/NS/13A, 62 pp.

Dyer, K.R. and R.L. Soulsby, 1988. Sand transport on the continental shelf. Annual Review of Fluid Mechanics, 20, 295-324.

Dyer, K.R., M.C. Christie and A.J. Manning, 2004. The effects of suspended sediment on turbulence within an estuarine turbidity maximum. Estuarine, Coastal and Shelf Science, 59, 237-248.

Elgar, S. B. Raubenheimer and R.T. Guza, 2005. Quality control of acoustic Doppler velocimeter data in the surfzone. Measurement Science and Technology, 16, 1889-1893.

Francken, F. and D. Van den Eynde, 2010. Calculation of current and wave induced turbulence from high frequency ADV measurements. Technical Report 2010/12/1/Turbulence/EN. Royal Belgian Institute of Natural Sciences, Operational Directorate Natural Environment, Brussels, 14 pp.

Fugate, D.C. and R.J. Chant, 2005. Near-bottom shear stresses in a small, highly stratified estuary. Journal of Geophysical Research, 110, C03022. doi:03010.01029/02004JC002563.

Goring, D.G. and V.I. Nikora, 2002. Despiking Acoustic Doppler Velocimeter Data. Journal of Hydraulics Engineering, 128(1), 117-126.

Grant, W.D. and O.S. Madsen, 1982. Movable bed roughness in unsteady oscillatory flow. Journal of Geophysical Research, 87, C1, 469-481.

Gross, T.F., A.E. Isley and C.R. Sherwood, 1992. Effective roughness changes during storms on the North California Shelf. Continental Shelf Research, 14, 1239-1256.

Günther, H., S. Hasselmann and P.A.E.M. Janssen, 1992. Wamodel Cycle 4. DKRZ Technical Report No. 4, Hamburg, October 1992, 102 pp.

Huntley, D.A., 1988. A modified intertial dissipation method for estimating seabed stresses at low Reynolds numbers, with application to wave/current boundary layer measurements. Journal of Physical Oceanography, 18, 339-346.

Huthnance, J.M., J.D. Humphery, P.J. Knight, P. G. Chatwin, L. Thomsen and M. White, 2002. Near-bed turbulence measurements, stress estimates and sediment mobility at the continental shelf edge. Progress in Oceanography, 52, 171-194.

Inoue, T., R.N. Glud, H. Stahl and A. Hume, 2011. Comparison of three different

methods for assessing in situ friction velocity: A case study from Lock Etive, Scotland. Limnology and Oceanography: Methods, 9, 275-287.

Kim, S.-C., C.T. Friedrichs, J.P.-Y. Maa and L.D. Wright, 2000. Estimating bottom stress in tidal boundary layer from acoustic Doppler velocimeter data. Journal of Hydraulic Engineering, 126, 399-406.

Lecouturier, M., 2000. Turbulence and macro-turbulence in the bottom boundary layer downstream of large-scale bedforms: implications for sediment transport. PhD. Thesis. University of Southampton, School of Ocean and Earth Science, 113 pp.

Lohrman, A., B. Hackett and L.D. Roed, 1990. High resolution measurements of turbulence, velocity, and stress using a pulse to pulse coherent sonar. Journal of Atmospheric and Oceanic Technology, 7, 19-37.

Lohrman, A., R. Cabrera, G. Gelfenbaum and J. Haines, 1995. Direct measurments of Reynolds stresses with an acoustic Doppler velocimeter. In: Proceedings of the IEEE Fifth Working Conference on Current Measurements, 7-9 February 1995, Saint Petersburg, Florida, US, 205-210.

Luyten, P. (editor), 2014. Coherens – A coupled hydrodynamic-ecological model for regional and shelf seas: user documentation. Version 2.6. RBINS Report, Operational Directorate Natural Environment, Royal Belgian Institute for Natural Sciences, Brussels, Belgium, 1554 pp.

Malarkey, J. and A.G. Davies, 2012. A simple procedure for calculating the mean and maximum bed stress under wave and current conditions for rough turbulent flow based on Soulsby and Clarke's(2005) method. Computers and Geosciences, 43, 101-107.

Mathys, P., J. De Rouck, L. Fernandez, J. Monbaliu, D. Van den Eynde, R. Delgado and A. Dujardin, 2011. Belgian Ocean Energy Assessment (BOREAS). Final Report. Belgian Science Policy Office, Brussels, 171 pp.

Nystrom, E.A., C.R. Rehmann and K.A. Oberg, 2007. Evaluation of mean velocity and turbulence measurements with ADCPs. Journal of Hydraulic Engineering, 133, 1310-1318.

Sherwood, C., J. Lacy and G. Voulgaris, 2006. Shear velocity estimates on the innter shelf off Grays Harbor, Washington, USA. Continental Shelf Research, 26, 1995-2018.

Soulsby, 1995. Bed shear-stresses due to combined waves and currents. In: Advances in Coastal Morphodynamics. M.J.F. Stive, H.J. de Vriend, J. Fredsøe, L. Hamm, R.L. Soulsby, C. Teisson and J.C. Winterwerp (eds.), 4-20 to 4-23. Delft Hydraulics, The Netherlands.

Soulsby, R., 1997. Dynamics of marine sands. A manual for practical applications. Telford, London, 249 pp.

Soulsby, R.L. and S. Clarke, 2005. Bed shear-stresses under combined waves and currents on smooth and rough beds. Report TR 137. HR Wallingford, Wallingford, United Kingdom, 42 pp. (http://www.estproc.net/EstProc_library.htm).

Soulsby, R.L. and J.D. Humphery, 1990. Field observations of wave-current interaction at the sea bed. Water Wave Kinematics, 178, 413-428.

Soulsby, R.L. and R.J.S. Whitehouse, 2005. Prediction of ripple properties in shelf

seas. Mark 2 Predictor for Time Evolution. Final Technical Report. Prepared for US Office of Naval Research, Contract No. N00014-04-C-0408. Report TR154, HR Wallingford, 41 pp + App.

Stacey, M.T., S.G. Monismith and J.R. Burau, 1999. Measurements of Reynolds stress profiles in unstratified tidal flow. Journal of Geophysical Research, 104, 10993-10949.

Stapleton, K.R. and D.A. Huntley, 1995. Seabed stress determinations using the intertial dissipation method and the turbulent kinetic energy method. Earth Surface Processes and Landforms, 20, 807-815.

Thompson, C., C. Amos, T. Jones and J. Chaplin, 2003. The manifestation of fluid-transmitted bed shear stress in a smooth annular flume – a comparison of methods. Journal of Coastal Research, 19, 1094-1103.

Trowbridge, J., 1998. Trowbridge, J. and S. Elgar, 2001. Turbulence measurements in the surf zone. Journal of Physical Oceanography, 31, 2403-2417.

Van den Eynde, D., 2013. Comparison of the results of the operational HYPAS and WAM models. Report OPTOS/1/DVDE/201303/EN/TR1, Royal Belgian Institute for Natural Sciences, Operational Directorate Natural Environment, Brussels, Belgium, 39 pp.

Van den Eynde, D., 2015. Measuring, using ADV and ADP sensors, and modelling bottom shear stresses in the Belgian coastal waters. Report ZAGRI-MOZ4/1/DVDE/201502/EN/TR02. Royal Belgian Institute of Natural Sciences, Operational Directorate Natural Environment, Brussels, 49 pp.

Van den Eynde, D. en J. Ozer, 1993. Sediment-Trend-Analyse: berekening van sedimenttransport met behulp van een mathematisch model. Studie uitgevoerd in opdracht van HAECON NV, betreffende de 'Sediment-Trend-Analyse' (STA) Activiteit 1. Beheerseenheid Mathematisch Model Noordzee, Brussel, 111 pp.

Van Lancker, V., S. Deleu, V. Bellec, S. Le Bot, E. Verfaillie, M. Fettweis, D. Van den Eynde, V. Pison, S. Wartel, J. Monbaliu, J. Portilla, J. Lanckneus, G. Moerkerke and S. Degraer, S., 2004. Management, research and budgetting of aggregates in shelf seas related to end-users (Marebasse). Scientific Report Year 2. Belgian Science Policy Office, 144 pp.

Verney, R., 2008. Hydrodynamics and wave parameters calculated from pressure and velocity measurements. Technical Report, Ifremer, Centre of Brest, France, 19 pp.

Verney, R., J. Deloffre, J.-C. Brun-Cottan and R. Lafite, 2007. The effect of wave-induced turbulence on intertidal mudflats : Impact of boat traffic and wind. Continental Shelf Research, 27, 594-612.

Wang, Y., W.F. Bohlen and J. O'Donnell, 2000. Storm enhanced bottom shear stress and associated entrainment in a moderate energetic estuary. Journal of Oceaongraphy, 56, 311-317.

The WAMDI Group, 1988. The WAM Model – A Third Generation Ocean Wave Prediction Model. Journal of Physical Oceanography, 18, 1775-1810.

Walter, R. K., M. E. Squibb, C.B. Woodson, J.R. Koseff and S. G. Monismith, 2014. Stratified turbulence in the nearshore coastal ocean: dynamics and evolution in the presence of internal bores. Journal of Geophysical Research: Oceans, 119, doi: 10.1002/2014JC010396.

Wilcock, P.R., 1996. Estimating local bed shear stress from velocity observations. Water Resources Research, 32, 3361-3366.

Wilkinson, R.H., 1984. A Method for Evaluating Statistical Errors Associated with Logarithmic Velocity Profiles. Geo-Marine Letters, 3, 49-52.

Williams, J.J., P. Bell and P.D. Thorne, 2003. Field measurements of flow fields and sediment transport above mobile bed forms. Journal of Geophysical Research, 108, 3109.

8. Appendix: Statistical parameters

For the validation, the statistical parameters bias, root mean square error (RMSE), the systematical and unsystematical RMSE and the correlation coefficient can be be calculated.

Hereafter, the measurements series will be presented as x and the model results (that is subject to the test) as y.

The mean values of the time series are represented by $\bar{x}$ (reference) and $\bar{y}$ (subject to test):

$$\overline{x} = \frac{1}{N}\sum_{i=1}^{N} x_i$$

$$\overline{y} = \frac{1}{N}\sum_{i=1}^{N} y_i$$

where N is the length of the time series.

The bias is the difference between the mean of the modelled and the measured time series:

$$bias = \overline{y} - \overline{x}$$

The closer the bias is to zero, the better both time series correspond. A positive bias value means that the modelled time series are an overestimation of the observed time series. A negative bias value means that the modelled time series are an underestimation of the observed time series.

The root mean square error (RMSE) is a measure for the absolute error and is defined as:

$$RMSE = \sqrt{\frac{\sum_{i=1}^{N}\left(y_i - x_i\right)^2}{N}}$$

Corresponding time series will result in RMSE values close to zero.

Furthermore, a systematical RMSE ($RMSE_s$) and an unsystematical RMSE ($RMSE_u$) can be defined, that evaluate respectively, the (absolute) error, which is generated by the deviation from the linear regression of the modelled time series from the measurements, and the error that is generated by the deviation from the individual model results from the linear regression itself. While the systematical RMSE could be reduced by applying a correction, using the linear regression, the unsystemical RMSE is the error which is inherent from the variation from the results themselves. These parameters can be calculated as:

$$RMSE_s = \sqrt{\frac{\sum_{i=1}^{N}\left(\hat{y}_i - x_i\right)^2}{N}}$$

$$RMSE_u = \sqrt{\frac{\sum_{i=1}^{N}\left(y_i - \hat{y}_i\right)^2}{N}}$$

with $\hat{y}_i$ is defined from the linear regression

$$\hat{y}_i = mx_i + b$$

with slope m and intercept b calculated from:

$$m = \frac{N\sum x_i y_i - \sum x_i \sum y_i}{N\sum x_i^{\,2} - \left(\sum x_i\right)^2}$$

$$b = \overline{y} - m\overline{x}$$

The correlation between both signals is given by Pearson's correlation coefficient, defined as:

$$r = \frac{\sum_{i=1}^{N}\left(x_i - \overline{x}\right)\left(y_i - \overline{y}\right)}{\sqrt{\sum_{i=1}^{N}\left(x_i - \overline{x}\right)^2}\sqrt{\sum_{i=1}^{N}\left(y_i - \overline{y}\right)^2}}$$

The scatter index is a measure for the relative error and is defined by:

$$S.I. = \frac{RMSE}{\overline{x}}$$

❍ COLOPHON

This report was issued by Operational Directorate Natural Environment in August 2016.

The reference code is INDI67/1/DVDE/201608/EN/TR1.

Status ☐ draft
☒ final version
☐ revised version of document
☐ confidential

Available in ☒ English
☐ Dutch
☐ French

If you have any questions or wish to receive additional copies of this document, please send an e-mail to *Dries.VandenEynde@mumm.ac.be*, quoting the reference, or write to:

Royal Belgian Institute of Natural Sciences
Operational Directorate Natural Environment
100 Gulledelle
B–1200 Brussels
Belgium
Phone: +32 2 773 2111
Fax: +32 2 770 6972
http://www.mumm.ac.be/

Royal Belgian Institute of Natural Sciences
Operational Directorate Natural Environment
Suspended Matter and Seabed Monitoring and Modelling Group

The typefaces used in this document are Gudrun Zapf-von Hesse's *Carmina Medium* at 10/14 for body text, and Frederic Goudy's *Goudy Sans Medium* for headings and captions.